Combustion Chemistry of Alkyl-Substituted Oxetane Radicals: Quantum Chemistry and Speciation

by

Anna C. Doner

(Under the Direction of Brandon Rotavera)

Abstract

Because of climate change and the energy crisis, significant research effort has been focused on the adoption of cleaner and more efficient combustion technologies, such as the homogeneous charge compression engine (HCCI). HCCI engines operate at lower temperatures and equivalence ratios than conventional spark ignition (SI) and diesel engines to curb the production of NO_X and soot. Because HCCI engines rely on autoignition triggered by compression alone, detailed chemical kinetics models are needed to accurately predict global observables important to engine design, such as ignition delay time. In low-temperature combustion chemistry, autoignition is driven by chain-branching pathways initiated by O_2-addition to alkylhydroperoxy (QOOH) radicals, which form following H-abstraction from, O_2-addition to, and isomerization of a fuel molecule. QOOH radicals also have chain-propagating pathways, which compete with chain-branching pathways initiated by second O_2-addition to QOOH. Because the steady-state concentration of QOOH is difficult to measure experimentally, direct products of QOOH are used as proxies to infer QOOH reaction rates from steady-state experiments. Cyclic ethers are direct chain-propagating products of QOOH radicals. Steady-state concentrations of cyclic ether isomers in combustion experiments are frequently used to validate chemical kinetics mechanisms. As such, high

level theoretical rate coefficients are available for a variety of QOOH $\longrightarrow$ cyclic ether + OH reactions. However, the steady-state concentration of cyclic ethers also depends on the rate of consumption, which is usually chosen on an arbitrary basis.

This dissertation focuses on the consumption reactions for alkyl-substituted four-membered cyclic ethers, or alkyloxetanes, including unimolecular decomposition following H-abstraction and bimolecular reaction with O_2. In addition, several preliminary chemometrics-based binary classification models were constructed to aid in the identification of relevant combustion intermediates with unknown VUV absorption spectra. The key outcomes of the present work are the following. Ring-opening pathways frequently lead to species which are also important intermediates in reaction mechanisms of other species. Stereochemistry has a significant impact on the dominant pathways for decomposition of cyclic ether peroxy radicals. Cyclic ether peroxy radicals can decompose via conventional QOOH-mediated pathways. Finally, a class of ring-opening pathways linking cyclic ether peroxy radicals to ketohydroperoxides (KHP) and related decomposition products was discovered.

INDEX WORDS: low-temperature combustion, cyclic ethers, alkylhydroperoxy (QOOH) radicals, ketohydroperoxides (KHP), dicarbonyls, bicyclic ethers, automated potential energy surface exploration, *ab inito* stationary point energies, master equation theoretical rate coefficients, theoretical branching fractions, multiplexed photoionization mass spectrometry (MPIMS), VUV absorption spectroscopy, chemometrics

Combustion Chemistry of Alkyl-Substituted Oxetane Radicals: Quantum Chemistry and Speciation

by

Anna C. Doner

B.S., University of Arkansas, 2018

A Dissertation Submitted to the Graduate Faculty of the University of Georgia in Partial Fulfillment of the Requirements for the Degree.

Doctor of Philosophy

Athens, Georgia

2023

Combustion Chemistry of Alkyl-Substituted Oxetane Radicals: Quantum Chemistry and Speciation

by

Anna C. Doner

Major Professor:	Brandon Rotavera, PhD
Committee:	Gary Douberly, PhD
	Steven Wheeler, PhD

Electronic Version Approved:

Ron Walcott
Dean of the Graduate School
The University of Georgia
May 2023

Dedication

This dissertation is dedicated to my dearest husband and collaborator, Matthew Davis, and my parents, Catherin and Scott Doner, whose steadfast support has made my education, culminated in this body of work, possible.

Acknowledgments

First, I would like to acknowledge Professor Brandon Rotavera for his support, which is many-fold. His support includes but is not limited to funding my graduate research assistantship since August 2021, consistently providing constructive and edifying feedback, and encouraging me to pursue the many opportunities I have been afforded during my time in his group. Additionally, I would like to acknowledge the University of Georgia Graduate School for funding my Georgia Research Education Award Traineeship (GREAT) stipend from August, 2018, to July 2021, and my travel to several conferences to present my research to peers. I would also like to acknowledge my professors and collaborators from the Center for Computational Quantum Chemistry (CCQC) for the excellent training and coursework which this dissertation required. Lastly, I would like to acknowledge the Office of Science for my Department of Energy Office of Science Graduate Student Research (SCGSR) award, which gave me the opportunity to complete a portion of my dissertation research as part of a productive collaboration with Dr. Judit Zádor at Sandia National Laboratories in Livermore, CA, in the Fall 2021-Spring 2022 academic year.

Contents

List of Figures

List of Tables

Chapter 1

Introduction

Although the United States relies on combustion of hydrocarbons and biomass for 99.2% of transportation energy,[1] fossil fuel availability and expense remains volatile. Significant research effort has been focused on optimizing renewable energy technologies, including the use of biofuels in advanced internal combustion engines. Conventional engines, such as spark ignition (SI) and diesel engines, produce NO_X, a gaseous pollutant which is harmful to human health. Diesel engines also produce soot due to local areas within the engine with high fuel-to-air ratios.

Advanced engines such as the Homogeneous Charge Compression Ignition (HCCI) engine, operate at low temperatures and low fuel-to-air ratios to curb the production of NO_X and soot. This is achieved by relying on compression to trigger autoignition of the fuel, which is well-mixed with air. This technology requires thorough understanding the kinetics of autoignition, so that ignition occurs on an appropriate and predictable timescale for an engine. Global observables, such as ignition delay time, are predicted by using chemical kinetics models. Every chemical kinetics model uses a chemical kinetics mechanism, which is a collection of chemical species, reactions, and rate coefficients. The overall quality of these chemical kinetics mechanisms is critical to model accuracy.

1.1 The Low-Temperature Combustion Mechanism for Alkanes

During low-temperature combustion, the backbone of alkane fuels remains intact. An abbreviated example of the mechanism for low-temperature combustion of *n*-pentane is given by Figure 1.1 Following H-abstraction from an alkane fuel (RH), alkyl radicals (R) undergo molecular oxygen addition, yielding an alkylperoxy radical (ROO). Alkylperoxy radicals either undergo HO_2-elimination or internal H-abstraction, resulting in a hydroperoxyalkyl radical (QOOH). HO_2 can abstract H from other species in the reacting mixture, producing H_2O_2. Under higher temperature conditions (>850 K), H_2O_2 contributes to ignition by decomposing into two highly reactive OH radicals. However, HO_2 is considered to be chain-inhibiting because its H-abstraction rates are three to four orders of magnitude slower than those of OH.

QOOH radicals produced from isomerization of ROO radicals can either undergo chain-propagation reactions including HO_2-elimination, β-scission, and cyclic ether formation, or second O_2-addition, yielding OOQOOH. Therefore, the balance between chain-branching and chain-propagating or chain-inhibiting pathways relies heavily on the specific structure and kinetics of the involved QOOH isomers. When the peroxy group of OOQOOH abstracts H from the carbon on which the hydroperoxy group is positioned, the unstable α-HOOQ'OOH formed loses OH to form a ketohydroperoxide (KHP) as shown in Figure 1.1. KHP are highly reactive species considered the source of ignition in low-temperature combustion. The most often prescribed decomposition pathway for KHP decomposition is OH loss by O-O bond scission, producing dicarbonyls.[2] However, there is an ongoing effort to better characterize the decomposition of KHP.[3,4] Alternative KHP decomposition pathways include the Korcek mechanism, which yields organic acids and carbonyls.[5]

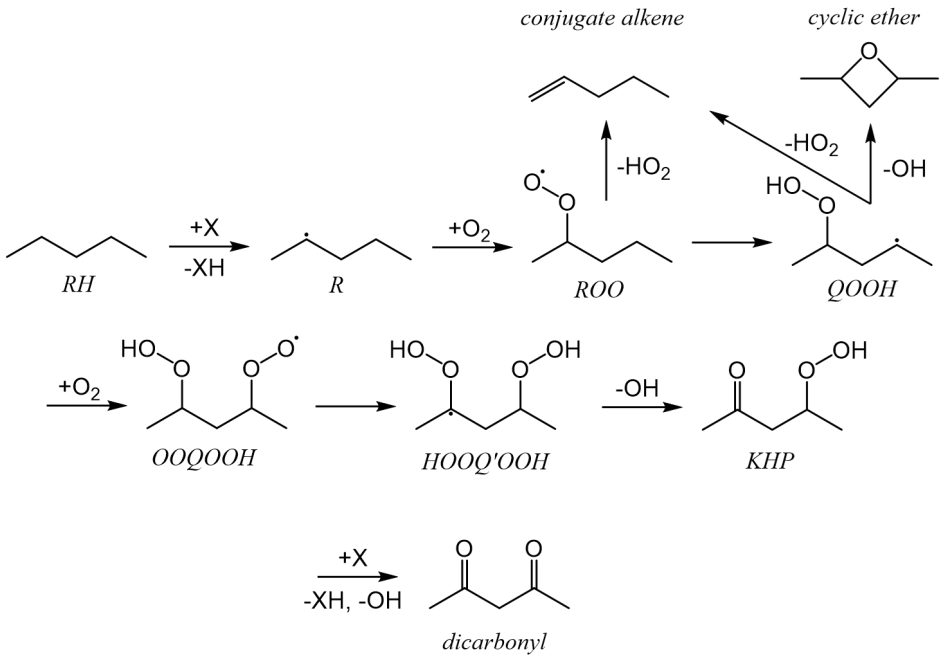

Figure 1.1: The mechanism for low-temperature combustion of *n*-pentane is summarized. X is a generic radical which abstracts H from RH and ketohydroperoxide (KHP). The generic names for chemical species are given in italics.

1.2 Sources of Error in Chemical Kinetics Mechanisms

Inaccurate rate coefficients contribute to error in chemical kinetics model predictions. Due to the vast number of reactions in the chemical kinetics mechanism of a single fuel species, rate parameters are often estimated using structure-activity relations.[6] Such estimation methods often work well for alkane fuels which have been studied extensively.[7] However, accurate rate rules and group additivity procedures are limited for fuel species with various oxygen-containing functional groups (e.g. ethers, alcohols, carbonyls, carboxylic acids).[8] For theoretical rate coefficients, the level of theory used for geometries, stationary point energies, and frequencies, impacts the uncertainty of computed rate coefficients. CBS-QB3,[9] a composite method commonly used to construct

potential energy surfaces, has been shown to have poor accuracy for the computation of enthalpy of formation for open and closed-shell $C_xH_yO_z$ species compared to similar methods.[10] Estimations by analogy to similar systems are frequently applied for collision parameters and rates for barrierless reactions (e.g. R + O_2 $\longrightarrow$ ROO). The accuracy of Lennard-Jones collision parameters can be improved by instead using full-dimensional intermolecular potentials,[11] which is far more computationally expensive than the estimation procedure provided by Jasper.[12] Barrierless reaction rates can be improved by the use of variable reaction coordinate transition state theory (VRC-TST) for barrierless reaction rates,[13] which is far more computationally intensive than simple transition state theory.

Although there are numerous opportunities for the improvement of theoretical rate coefficient accuracy, many reactions are missing altogether. Missing reactions in chemical kinetics mechanisms causes what is called mechanism truncation error. Ideally, each reaction in a chemical kinetics mechanism is a single elementary step. However, in the absence of rate parameters, several elementary steps are often combined into one. Similarly, some isomers produced from similar pathways are lumped into one representative species (e.g. cyclic ethers). As an example, the mechanism for low-temperature combuston of *n*-butane from Cord et al.[14] lumps together both of the the three-membered cyclic ethers formed from *n*-butane QOOH radicals, 2-ethyloxirane and 2,3-dimethyloxirane. Stereoisomers are more often than not lumped together, especially when their rates of formation are similar.[15] However, stereoisomers can have distinct consumption pathways with different rates.[16] This phenomenon has been investigated by Danilack et al.[17] by constructing a chemical kinetics mechanism for diethyl ether which distinguishes diastereomers and comparing modeling results. These changes resulted in an increase in the predicted peak KHP concentration by almost 15%.[17]

1.3 Speciation Diagnostics

Due to the short lifetimes and low steady-state concentrations of QOOH and KHP, most experimental work relies on the quantification of their direct products to better understand and model their kinetics. Cyclic ethers are especially useful for studying QOOH because there are few, if any, pathways producing cyclic ethers from species apart from QOOH. This is in contrast to other QOOH decomposition products like conjugate alkenes, which can be produced from a number of pathways not involving QOOH, such as H-abstraction. Dicarbonyls are frequently used as proxy species for KHP. Species profiles for such products are useful for the assessment of chemical kinetics mechanism accuracy.

1.3.1 Multiplexed Photoionization Mass Spectrometry (MPIMS)

In the present work, two methods for obtaining species profiles are discussed. The first is Multiplexed Photoionization Mass Spectrometry (MPIMS), which uses time-resolved mass spectrometry in conjunction with VUV photoionization spectroscopy to identify and quantify intermediates. Experimental signals are fit to reference photoionization spectra for quantification. In the absence of reference measurements, possible species corresponding to unknown photoionization spectra may be narrowed down by comparing the onset photoionization energy to theoretically computed adiabatic ionization energies.[18,19,20,21] There are some limitations of MPIMS which can be attributed to the photoionization process. Large changes in the geometry of intermediates pre- and post-photo-ionization have low Franck-Condon overlap, resulting to low or non-existent photoionization signal. The intense VUV radiation can also fragment intermediates before detection.

1.3.2 Vacuum-Ultraviolet (VUV) Absorption Spectroscopy

In the Rotavera Laboratory, isomer-resolved speciation data are collected from jet-stirred reactor (JSR) experiments. Samples are collected at steady state conditions and analyzed via gas chromatography and mass spectrometry (GC-MS). Mass spectrometry sometimes fails to resolve constitutional isomers due to unpredictable fragmentation patterns.[22] In order to achieve superior isomer resolution, gas chromatography and vacuum ultraviolet (VUV) absorption spectroscopy is used as a parallel diagnostic. VUV absorption cross-sections are similar or larger in magnitude than VUV photoionization cross-sections, allowing for a low detection limit of approximately 1 ppm. Furthermore, VUV absorption spectra are far more unique than VUV photoionization spectra,[23] allowing for easy distinction between wide ranges of constitutional isomers and stereoisomers. Chapter 7 briefly summarizes the results of a campaign of quantitative Vacuum Ultraviolet (VUV) absorption reference measurements for relevant combustion intermediates. Literature comparisons are included. At present, there is no common procedure for identifying the species corresponding to unknown VUV absorption spectra. Toward that end, Chapter 8 analyzes the results from binary classification models for VUV absorption spectra for five different molecular structure motifs.[24]

1.4 Cyclic Ether Combustion Kinetics

The formation of cyclic ethers from QOOH radicals has been studied extensively via experiment and theory. In fact, the formation of 2,2-dimethyloxirane from the QOOH species 2-hydroperoxy-2-methylpropan-1-yl was recently observed by Hansen et al.[25] using pump-probe spectroscopy. Theoretical rate coefficients for formation of cyclic ethers from QOOH have been computed and added to chemical kinetics mechanism for a wide range of alkanes (e.g. *n*-butane, *n*-pentane).[26,15] However, studies on the kinetics of consumption reactions of cyclic ethers are limited to those for cyclic ethers which are also po-

tential biofuels (e.g. tetrahydrofuran, tetrahydropyran).[27,18] The alkyl-substituted oxiranes and oxetanes investigated in the present work are not potential biofuels, but they are direct products of QOOH decomposition in low-temperature combustion of *n*-butane and *n*-pentane which have been detected in abundance in jet-stirred reactor (JSR) experiments.[14,15]

1.4.1 Reaction Mechanisms of Oxolanes in the Literature

Oxolanes are the closest analogs to oxetanes for which detailed chemical kinetics mechanisms have been developed. These mechanisms include tetrahydrofuran (THF),[28,29] 2-methyltetrahydrofuran (2-MTHF),[30,31] and 2,5-dimethyltetrahydrofuran (2,5-DMTHF).[30] Each of the mechanisms includes unimolecular decomposition pathways following H-abstraction. Unimolecular decomposition of alkyl-substituted oxolanyl radicals proceeds via ring opening followed by β-scission, yielding small organic species (e.g. formaldehyde, acetaldehyde, ethylene, propylene) and radicals (e.g. allyl, vinoxy, β-acetonyl).

The mechanisms for THF and 2-MTHF also include peroxy radical decomposition pathways following O_2-addition. Alkyl-substituted oxolanyl peroxy radicals form QOOH species via internal H-abstraction. The QOOH species derived from oxolanes have conventional QOOH-mediated pathways such as HO_2-elimination and bicyclic ether formation as well as ring opening pathways. The majority of ring opening pathways in the oxolane mechanisms are concerted with loss of OH, due to the formation of unstable α-QOOH radicals.[32] An example reaction forming butanedial is shown in Figure 1.2. butanedial was detected in jet-stirred reactor (JSR) experiments for the first time by Koritzke et al.[27] Although butanedial is a dicarbonyl, which are decomposition products of KHP, the KHP which would produce butanedial, 4-hydroperoxybutanal, is likely insignificant because the pathway forming it includes several unfavorable steps, including H-abstraction from the primary carbon of butane, internal H-abstraction from a primary carbon forming QOOH, and second O_2-addition to a primary radical forming OOQOOH.

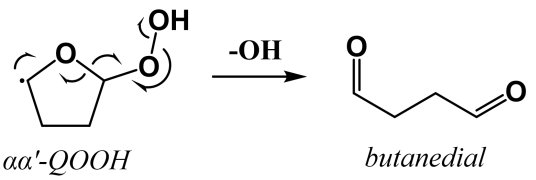

Figure 1.2: The concerted ring opening and OH loss step for the $\alpha\alpha'$-QOOH from THF is shown.[29] The product, butanedial, was detected in THF combustion experiments for the first time by Koritzke et al.[27]

One notable ring opening pathway in the potential energy surfaces constructed by Fenard et al.[29] which does not result in simultaneous OH-loss is the ring opening of the $\alpha\beta'$-QOOH from THF which yields 1-hydroperoxy-1-oxy-3-butene. 1-hydroperoxy-1-oxy-3-butene has a low barrier (1.3 kcal/mol) for β-scission forming allyl and performic acid (Figure 1.3). Although performic acid is a KHP, the pathway to performic acid was not included in the mechanism for THF. Performic acid was not detected experimentally by Fenard et al,[29] potentially due to short lifetime and low-steady state concentration typical to KHP species in temperature range studied because of facile abstraction of the H or unimolecular decomposition yielding carbon dioxide, H, and OH. However, low-flux species which contribute to chain-branching can have large impacts on global observables such as ignition delay time. Four similar pathways were discovered for 2,4-dimethyloxetane and 2-ethyloxetane in the present work (Chapter 6), suggesting that small KHP formation from cyclic ether oxidation may contribute substantially to the reactivity of alkane fuels in low-temperature combustion.

Stereochemistry was not accounted for in the aforementioned mechanism except for the OOQOOH radicals resulting from second O_2-addition in the THF mechanism explored by Antonov et al.[28] Antonov et al. demonstrated that *cis* and *trans* isomers of OOQOOH radicals have differing decomposition pathways, which can impact the overall reactivity of THF as a fuel.[28] The results of the present work demonstrate similar effects of the relative orientation of alkyl-substituents and

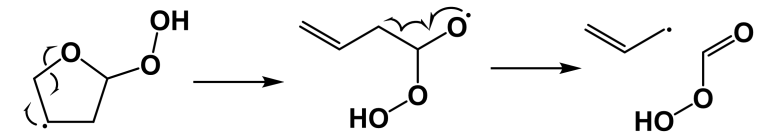

Figure 1.3: The pathway from the $\alpha\beta'$-QOOH from THF oxidation to performic acid and allyl found by Fenard et al.[29] Ring opening of $\alpha\beta'$-QOOH has a 28.7 kcal/mol barrier, and β-scission of 1-hydroperoxy-1-oxy-3-butene has a barrier of only 1.3 kcal/mol at the CBS-QB3 level of theory.

peroxy groups in the oxidation of alkyl-substituted oxiranes (Chapter 4) and oxetanes (Chapter 6).

1.4.2 Alkyl-Substituted Oxiranes

In Chapter 4, the potential energy surfaces constructed for the unimolecular decomposition of peroxy radicals resulting from H-abstraction from and subsequent O_2-addition to *cis*-2,3-dimethyloxirane, *trans*-2,3-dimethyloxirane, and 2-ethyloxirane are provided. Pathways discovered for these peroxy radicals are supported by the detection of their unique QOOH decomposition products in MPIMS experiments probing Cl-initiated oxidation of *cis*-2,3-dimethyloxirane, *trans*-2,3-dimethyloxirane, and 2-ethyloxirane. One of the key outcomes of this work is that O_2-addition to alkyl-substituted oxiranyl radicals is, in fact, competitive with unimolecular decomposition via ring opening. QOOH radicals derived from alkyl-substituted oxiranes underwent a combination of ring opening and conventional QOOH-mediated pathways.

1.4.3 Alkyl-Substituted Oxetanes

In Chapter 5, potential energy surfaces, theoretical rate coefficients, and theoretical branching fractions are provided for the decomposition of each of the radicals resulting from H-abstraction from *syn*-2,4-dimethyloxetane, *anti*-2,4-dimethyloxetane, and 2-ethyloxetane. Taking a stepwise approach re-

sulted in the discovery of some new favorable pathways for decomposition of alkyl-substituted oxetanyl radicals. In Chapter 6, the same investigation for each of the peroxy radicals resulting from O_2-addition to the aforementioned H-abstraction radicals, is discussed. The pathways forming each of the radicals arising from 2,4-dimethyloxetane are shown with nomenclature in Figure 1.4. The pathways forming each of the radicals arising from 2-ethyloxetane are shown with nomenclature in Figure 1.5. Key findings for the peroxy radicals include the influence of stereochemistry on the ROO $\longrightarrow$ QOOH isomerization, the competition between conventional ROO and QOOH-mediated reactions and ring opening reactions, and alternate pathways to KHP and dicarbonyls.

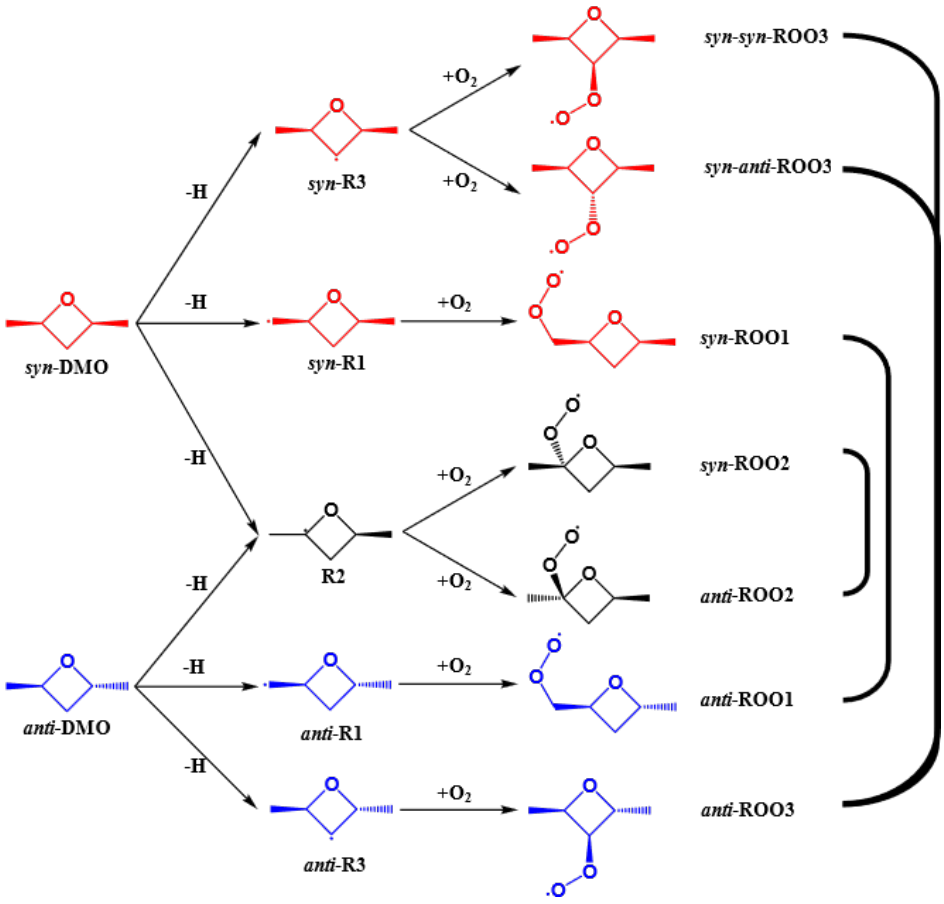

Figure 1.4: The radicals produced from H-abstraction from and O_2-addition to *syn* and *anti*-2,4-dimethyloxetane are shown with abbreviations. Diastereomers are connected by black lines on the right.

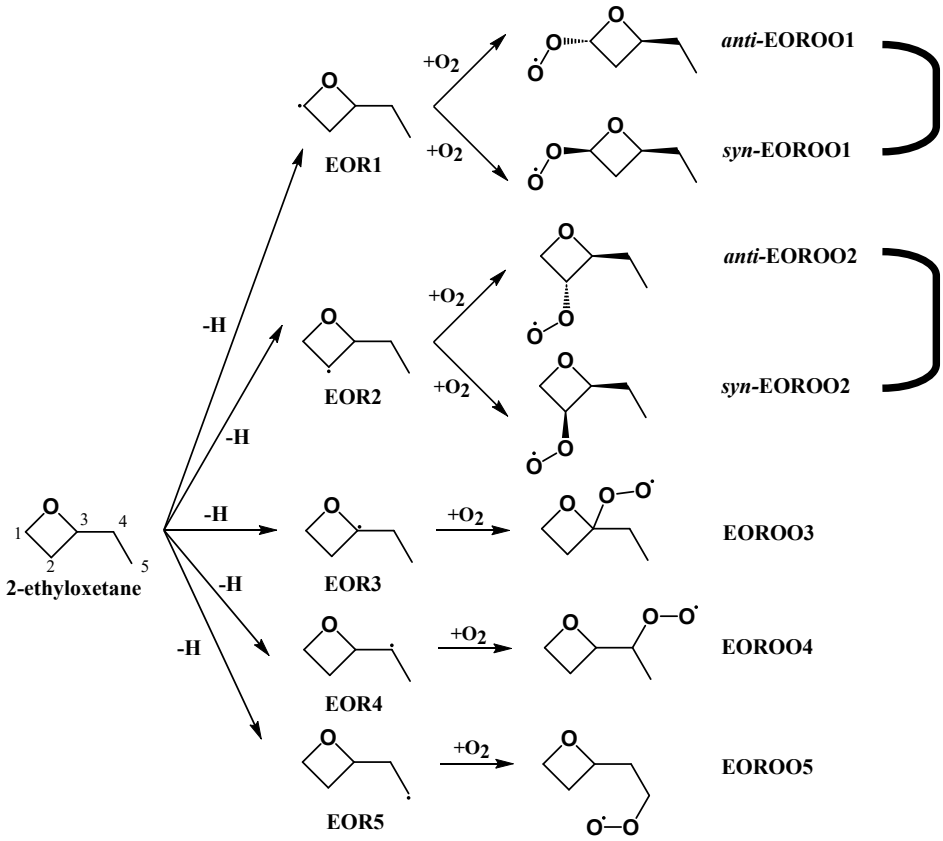

Figure 1.5: The radicals produced from H-abstraction from and O_2-addition to 2-ethyloxetane are shown with abbreviations. Diastereomers are connected by black lines on the right

Chapter 2

Computational Methods

Computational methods were employed for the construction of potential energy surfaces and computation of theoretical rate coefficients for 10 alkyl-substituted oxetanyl radicals, and the 14 peroxy radicals they form upon O_2-addition. In addition, machine learning was applied for classification of Vacuum Ultraviolet (VUV) absorption spectra. The following sub-sections detail those methods.

2.1 Potential Energy Surfaces

Two different methods were used to construct the potential energy surfaces in this work. In the first, a composite method was employed, and transition states were found "by-hand". Information about the methods used is also described in the publications of this work on 2,3-dimethyloxirane and 2-ethyloxirane peroxy radical chemistry by Doner et al. and Christianson et al.[20,21] In the second, the automated chemical kinetics workflow, KinBot,[33,34,35] was applied, which offers a streamlined and unbiased approach. The details of the methods applied are also described in two publications on 2,4-dimethyloxetane radical chemistry by Doner et al.[16,36] The following sub-sections provide more detail on both potential energy surface construction methods.

2.1.1 Exploratory Methods

Exploratory potential energy surface computations were performed at the ccCA-PS3 level of theory.[37] ccCA-PS3 is a composite method with geometries optimized at the B3LYP/cc-pVTZ level of theory with the following energy corrections (Equation 2.1) where E_e is the electronic energy, ΔCC is the coupled cluster correction, ΔCV is the core valence correction, ΔSR is the relativity correction, and ΔZPE is the zero-point energy correction.

$$E[\text{ccCA-PS3}] = E_e[\text{MP2/CBS}] + \Delta CC + \Delta CV + \Delta SR + \Delta ZPE \tag{2.1}$$

The electronic energy was obtained by independently extrapolating the aug-cc-pVXZ (X=D,T,Q) HF energy and MP2 correlation energy. The HF/CBS energy was estimated via a two-point fit of the HF/aug-cc-pVXZ (X=T,Q) energies to the following equation.

$$E[\text{HF}](n) = E[\text{HF/CBS}] - Be^{-1.63n} \tag{2.2}$$

The MP2/CBS correlation energy is estimated using an average of a three-point fit through the MP2/aug-cc-pVXZ (X=D,T,Q) correlation energies given by the following equation.

$$E_{corr}[\text{MP2}](x) = E_{corr}[\text{MP2/CBS}] + Be^{-(x-1)} + Ce^{-(x-1)^2} \tag{2.3}$$

The coupled cluster correction is defined by Equation 2.4. The core valence correction is defined by Equation 2.5 where AE is the all-electron computation and FC is the frozen-core computation.The relativity correction is defined in Equation 2.6 where the Douglas Kroll Hamiltonian is approximated to second order (DKH2).The harmonic zero-point energy was scaled by a factor of 0.989 to obtain ΔZPE as recommended by Deyonker et al.[38]

$$\begin{aligned}\Delta CC = {} & E_e[\text{CCSD(T)/aug-cc-pVTZ}] \\ & - E_e[\text{MP2/aug-cc-pVTZ}]\end{aligned} \tag{2.4}$$

$$\begin{aligned}\Delta CV = E_e[AE - \text{MP2/aug-cc-pVTZ}] \\ -E_e[FC - \text{MP2/aug-cc-pVTZ}]\end{aligned} \tag{2.5}$$

$$\Delta SR = E_e[\text{MP2/cc-pVTZ-DK}] - E_e[\text{MP2/cc-pVTZ}] \tag{2.6}$$

The accuracy of ccCA-PS3 is comparable to the more commonly used composite method, CBS-QB3, with a mean absolute deviation of 0.96 kcalmol^{-1} on the G3/99 test set.[37] Transition states were optimized for the following reaction types: internal H-abstraction, HO_2-elimination, cyclic ether formation, ring-opening and inversion. Internal H-abstraction reactions forming QOOH through a four-membered transition state were not considered because they typically have high energy barriers.[39] Both concerted and sequential HO_2-elimination reactions were considered. Inversion reactions were considered when the radical was centered on a non-planar tertiary radical. An example is given in Figure 2.1. Intrinsic reaction coordinate (IRC) calculations were performed at the same level of theory.

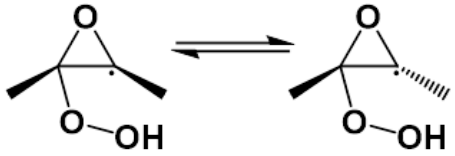

Figure 2.1: Tertiary radicals resulting from H abstraction from alkyl-substituted oxiranes can undergo inversion through an umbrella-like motion. The analogous tertiary radicals resulting from H abstracton from alkyl-substituted oxetanes are planar and therefore do not undergo inversion.

2.1.2 Automated Methods: KinBot

The reactive potential energy surfaces for each of the 10 of cyclic ether radicals resulting from H-abstraction from DMO and EO in Table 2.1 and the 15 cyclic ether peroxy radicals resulting from H-abstraction from and O_2-addition to DMO

and EO in Table 2.2 were explored automatically with the open-source kinetics workflow code, KinBot.[34,35,33]

Table 2.1: 10 energetically unique alkyl-substituted oxetane radicals can be formed following H-abstraction from 2,4-dimethyloxetane and 2-ethyloxetane. Here, their structures and names are provided for reference.

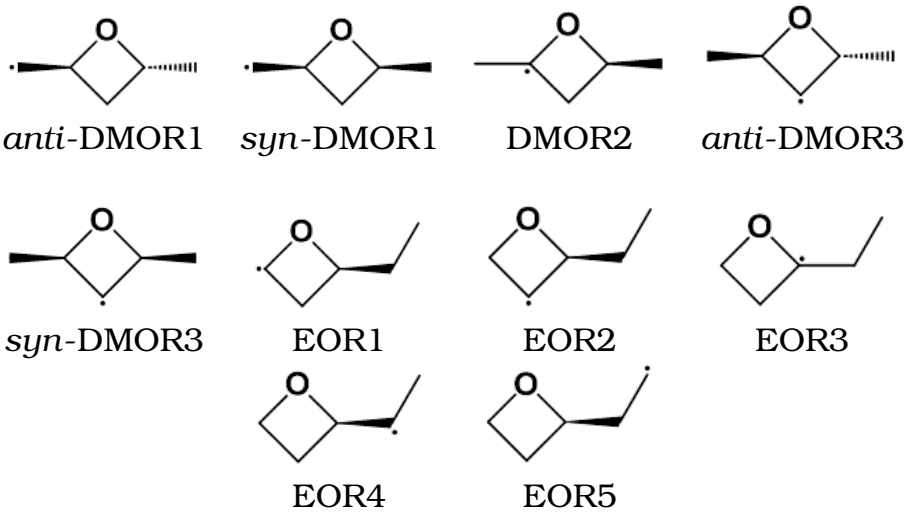

First, the starting radical structure was optimized at L1 = B3LYP/6-31+G. Then, a conformational search was conducted at L1. The lowest energy conformer structure was then re-optimized at L2= ωB97X-D/6-311++G(d,p). The electronic energy, frequencies, zero-point energy correction, and hindered rotor scans were computed at L2.The final electronic energy was computed at L3=CCSD(T)-F12/cc-pVXZ-F12a where X is D for ROO radicals and T for R radicals. Therefore, the values reported can be represented by Equation 2.7, where E_{NN} is the nuclear repulsion energy, E_e is the electronic energy, and ZPE is the zero-point energy correction.

$$E = E_e(\text{L3//L2}) + ZPE(\text{L2//L2}) \tag{2.7}$$

The following sections contain details about the conformational search, hindered rotor scan, and reaction search procedures.

Table 2.2: 14 energetically unique alkyl-substited oxetane peroxy radicals can be formed following H-abstraction from and O_2-addition to 2,4-dimethyloxetane and 2-ethyloxetane. Here their structures and names are provided for reference.

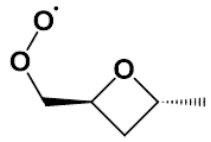
anti-DMOROO1

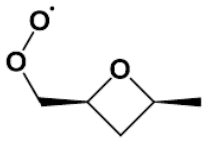
syn-DMOROO1


anti-DMOROO2

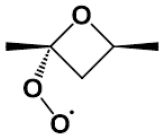
syn-DMOROO2

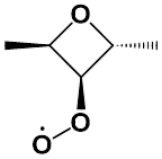
anti-DMOROO3

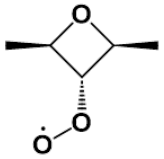
syn-anti-DMOROO3

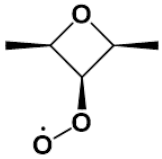
syn-syn-DMOROO3

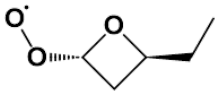
anti-EOROO1

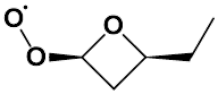
syn-EOROO1

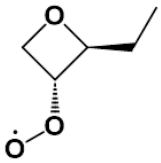
anti-EOROO2

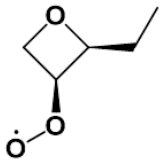
syn-EOROO2

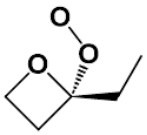
EOROO3

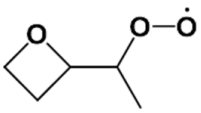
EOROO4

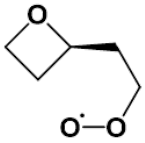
EOROO5

Conformational Search

The conformational search was performed on a 60° (6 points) grid. Ring conformers were generated by systematically distorting the backbone of the ring. When determining the number of ring conformers to generate, the following rules were used. For 3-membered rings, no ring conformers were generated. For 4-membered, 5-, and 6-membered rings, the number of trial ring conformers was calculated as $3^{n_{\text{ring}}-3}$,

where n_{ring} is the size of the ring. For fused rings, the size of the smallest complete ring was taken. The conformers of each sub-ring were sampled as usual. The conformers of the acyclic side chains of each ring conformer are then sampled on the 60° grid, yielding $n_{\mathrm{dih}}^3 \times \Pi_i^N 3^{n\mathrm{ring},i-3}$ total trial conformers, where N is the number of subrings. However, if the predicted number of conformers was greater than 300, 300 points on the grid were randomly selected.

Hindered Rotor Scans

For each rotor, the energy was calculated for 24 dihedral angles separated by 15^o. All degrees of freedom except the scanned dihedral were relaxed. Failed points were approximated using interpolation based on a Fourier fit. The motion along the rotors at the minimum was projected out from the Hessian to arrive at the reduced set of harmonic frequencies. In the rare case that KinBot found a lower energy conformer during the hindered rotor scans, the new, lower energy structure replaced the old one.

Reaction Search

Reaction classes have templates that are used to construct initial saddle point guesses for the current well. The initial saddle point guess is constructed by a series of constrained optimization steps at the L0 = AM1 level of theory. The initial guess is refined to a true first-order-saddle-point (FOSP) at the L1 = B3LYP/6-31+G level theory and confirmed by intrinsic reaction coordinate (IRC) calculations at the same level. For this system, a stereochemistry check feature was added to KinBot. This is done by checking that the stereochemistry of the reactant from the IRC calculation matches the stereochemistry of the current well geometry if there is more than one chiral center, which results in energetically distinct diastereomers. Inversion between diastereomers was not consider because the tertiary oxetane radicals are approximately planar, and inversion not about a tertiary radical would have a large barrier.

Pruning Potential Energy Surfaces

There were two conditions for a product well to be included and followed on the potential energy surfaces. The first is that the L1 barrier height leading to the product well is less than a user-determined energy threshold. For the radicals resulting from H-abstraction from DMO or EO, this threshold was 30 kcal/mol above the initial radical. For peroxy radicals resulting from H-abstraction from and O_2-addition to DMO and EO, this threshold was equal to the R + O_2 $\longrightarrow$ ROO well depth computed at the L3 level of theory. The second condition for inclusion of a product well was that the predicted branching fraction from the reactant well was greater than 5% at the high pressure limit at 400 K or 1000 K. The branching fractions required for this condition were computed by solving the master equation constructed with the L2 level stationary points directly connected to the current reactant well.

2.2 Theoretical Rate Coefficients

For each stationary point, the input parameters were taken for the lowest energy conformer found by KinBot. The master equations were assembled by KinBot and solved using the MESS code[40]. The direct solving method was used except for the DMOR1 system, for which the low-eigenvalue method was used because of numerical instability, especially below 400 K. Collision parameters and rates for the barrierless oxygen addition were estimated as describe in the following sections.

2.2.1 Collision Parameters

Estimates for the Lennard-Jones parameters were calculated according to the formula for alcohols and hydroperoxides given by Jasper[12] for the R and ROO radicals, respectively. The average downward energy transfer α was calculated between 300 K and 1000 K and fit to the form $\alpha_0 \times (T/300\text{ K})^n$. The energy relaxation factor α and power n depend on the equilibrium distance (σ), the well depth (ϵ), and the effective number of heavy atoms (N_{eff}) which is defined in Equation 2.8 below where p, s, t, and q, denote primary, secondary,

tertiary, and quaternary carbons, $ring$ denotes carbons in a ring of the structure, and N denotes the number of bonds between the types of carbons denoted.

$$N_{eff} = 1 + (N_{pp} + N_{ps} + N_{ss}) + \frac{2}{3}(N_{pt} + N_{st}) + \frac{1}{3}(N_{pq} + N_{sq}) + \frac{1}{3}(N_{CO} + N_{OO}) + \frac{1}{2}N_{ss,ring} - N_{rings} \tag{2.8}$$

Table 2.3 contains the values of σ, ϵ, α, n, and the root-mean-squared (RMS) of the resulting fit for each of the R and ROO radicals.

The same energy transfer parameters were assumed for all wells on each PES. This may incur some additional uncertainty. However, for the QOOH species on the ROO surfaces, the estimates would be exactly the same as the ROO radical because the connectivity of the heavy atoms, which is used to evaluate N_{eff} is unchanged. Furthermore, since only N, the number of heavy atoms, enters the estimation of σ and ϵ, their estimates within this framework are also unchanged for ring-opened or otherwise rearranged structures. For Ar we used $\sigma = 3.462$ Å and $\epsilon = 88.75$ cm^{-1}.[11]

2.2.2 Phase-Space Theory

The R + O_2 entrance channel on the for the formation of each of the peroxy radicals is barrierless. While in principle it is possible to calculate the microcanonical rate coefficients for this step in a variable-reaction-coordinate transition state theory (VRC-TST) framework, a simpler approach was used. The sum of states for the transition state was approximated using phase-space theory.[41] The R...O_2 potential was modeled as ar^n, with $n = 6$. The pre-exponential factor a was adjusted to match the desired capture rate coefficients, which are given by Table 2.4. Half of the recommended value was taken for molecules which have two sides for oxygen to attack, resulting in diastereomer pair peroxy radicals.

Table 2.3: The collision parameters used to solve the master equation (σ, ϵ, α_0, and n), are given by starting radical.

Species	σ	ϵ (K)	N_{eff}	α_0 (cm^{-1})	n	α-fit RMS (cm^{-1})
anti-DMOR1, *syn*-DMOR1, DMOR2, *anti*-DMOR3, *syn*-DMOR3	4.36	252	$3\frac{1}{3}$	323	0.53	6.6
EOR1, EOR2, EOR3, EOR4, EOR5	4.36	252	$3\frac{1}{2}$	340	0.51	6.9
anti-DMOROO1, *syn*-DMOROO1, *anti*-DMOROO2, *syn*-DMOROO2	4.62	248	4	269	0.54	6.0
anti-DMOROO3, *syn-anti*-DMOROO3, *syn-syn*-DMOROO3	4.62	248	$2\frac{2}{3}$	211	0.66	6.0
anti-EOROO1, *syn*-EOROO1, *anti*-EOROO2, *syn*-EOROO2	4.62	248	$3\frac{2}{3}$	260	0.55	5.4
EOROO3, EOROO4	4.62	248	$3\frac{1}{6}$	239	0.59	5.0
EOROO5	4.62	248	$4\frac{1}{6}$	280	0.52	5.7

Table 2.4: The potential for barrierless O_2-addition to each of the alkyl-substituted oxetane radicals were modeled by fitting an exponential to an analogous rate coefficient selected from the literature. In the first two columns, each O_2-addition step is represented by alkyl-substituted oxetane radical, R, and the peroxy radical(s) resulting from addition of O_2, ROO. The referenced rate coefficients and their description are given by the third and fourth columns.

R	ROO	Assigned Rate Coefficient, k (cm^3s^{-1})	Reference
anti-DMOR1 *syn*-DMOR1	*anti*-DMOROO1 *syn*-DMOROO1	7.5×10^{-12}	1-butyl + O_2 [42]
DMOR2	*anti*-DMOROO2 *syn*-DMOROO2	1×10^{-11}	*tert*-butyl + O_2 [42]
anti-DMOR3	*anti*-DMOROO3	1.5×10^{-11}	cyclopentyl + O_2 [43]
syn-DMOR3	*syn*-*anti*-DMOROO3 *syn*-*syn*-DMOROO3	7.5×10^{-12}	cyclopentyl + O_2 [43]
EOR1	*anti*-EOROO1 *syn*-EOROO2	7.5×10^{-12}	cyclopentyl + O_2 [43]
EOR2	*anti*-EOROO2 *syn*-EOROO2	7.5×10^{-12}	cyclopentyl + O_2 [43]
EOR3	EOROO3	2×10^{-11}	*tert*-butyl + O_2 [42]
EOR4	EOROO4	1.7×10^{-11}	2-butyl + O_2 [42]
EOR5	EOROO5	7.5×10^{-12}	1-butyl + O_2 [42]

2.2.3 Theoretical Branching Fractions

To obtain theoretical branching fractions, the the kinetic differential equations produced from the master equation calculation were solved with the desired parameters for temperature, pressure, initial molecular oxygen concentration, and elapsed time. The conditions were selected based on the conditions at which cyclic ethers were detected in the highest concentrations in *n*-pentane combustion experiments.[15] The conditions of interest are 650 K and 825 K at atmospheric pressure and excess (10^{18} molecules cm^{-3}) molecular oxygen, resulting in pseudo-first order conditions. The time elapsed was chosen to be 20 ms.

2.3 Classification of Vacuum Ultraviolet Absorbance Spectra

Machine learning (ML) classification models were constructed as a tool to narrow down the pool of possible species corresponding to unknown VUV absorption spectra which may be encountered during combustion kinetics experiments. The computational methods for this work are also described in the publication by Doner et al.[24] Table 2.5 summarizes five of the binary molecular classifications employed for which the best accuracy was achieved, corresponding definitions, and representative species which possess that molecular attribute. Each species is either "positive" or "negative" for each classification, meaning that the species either possesses or does not possess that molecular attribute, respectively.

The machine learning, chemometrics, and statistical methods used to construct, improve, and assess VUV absorption spectra classification models are discussed in Sections 2.3.1-2.3.4. The open-source Python package SciKitLearn[44] was employed for all decompositions, regressions, and transformations. Principal Component Analysis (PCA) was used for unsupervised, exploratory analysis of the VUV absorption spectra dataset (Section 2.3.1). Several pre-processing procedures were applied and compared for classification model accuracy (Section 2.3.2). Two types of supervised classification (Sec-

Table 2.5: The five selected classification criteria are explained. Examples of chemical species which possess the molecular feature described are included.

Classification	Definition	Examples
alkane	saturated hydrocarbons, including linear, branched and cyclic species	*n*-butane, *iso*-butane, cyclopentane
non-conjugated alkene	species containing C=C bonds that are *not* part of a conjugated π system of 3 or more adjacent atoms	*cis*-2-butene, 1,4-cyclohexadiene, 3-methyl-3-buten-1-ol
oxygen-containing	species containing one or more oxygen atoms as a part of any functional group	2-butanol, cyclopentanone, 1,4-dioxane
conjugation with oxygen	species which contain 3 or more adjacent atoms part of a conjugated π-system, with one or more of those atoms being an oxygen atom	diacetyl, 2-cyclopentene-1-one, ethyl vinyl ether
homocyclic	cyclic species, excluding species with an ether functional group	cyclopentane, cyclohexanol, benzene

tion 2.3.3) were applied, Partial Least-Squares Discriminant Analysis (PLS-DA) and decision trees.

Due to the relatively manageable dataset, leave-one-out cross-validation was applied for all models to obtain all accuracy, precision, and recall values reported herein. The definitions of each of these metrics is given by Table 2.6. F1-scores were similar to the computed accuracy values and are included in the Appendices. For each VUV absorption spectrum, the molecular classification was predicted using the

remaining 101 spectra as the training set. The accuracy, precision, and recall reported herein are the average of the results from each individual spectrum trained on all remaining spectra. Because each spectrum is classified individually, random sample selection for the test set is not required. Learning curves were constructed to determine the benefit of increasing the training set size, in which training sets of size n were randomly selected 100 times. The remaining spectra were used as a test set, and the average accuracy and F1-score with standard deviation at each training set size are reported in the Appendices. In Section 2.3.4, the classification models were applied to specific bins of the VUV absorption spectrum. The accuracy obtained in each region sheds light on the most important part of the VUV absorption spectrum for classification.

Table 2.6: The definitions for the classification metrics, accuracy, precision, and recall are given.

metric	**definition**
accuracy	the portion of samples for which the class was predicted correctly
precision	the portion of samples predicted to be in a class that are actually in that class
recall	the portion of samples in a class that are predicted to be in that class

2.3.1 Principal Components Analysis (PCA)

Principal Component Analysis (PCA) is an unsupervised method of dimensionality reduction that maximizes variance. In PCA, the dataset is represented by a number of principal components, which are ranked by the percent variance within the dataset. PCA often reveals natural clustering of samples in principal component space. The loadings of each principal component are the coefficients of the linear combination of the original variables from which the principal components (PCs) are constructed and provide information on contributions of

the initial dataset variables to that particular principal component. In the case of spectroscopy, loadings often resemble peaks that account for the most variance in the dataset. In the present work, the cross-sections were normalized with MaxAbsScaler in SciKitLearn[44] to a maximum value within the range of photon energies utilized in the experiments.

2.3.2 Pre-Processing

Several function transformations were applied to the cross-sections prior to PLS-DA using the FunctionTransformer function in SciKitLearn. All functions were used directly or built from SciPy or NumPy functions. Function transformations that improved classification accuracy the most were the following: square root, natural log, Gaussian, inverse Morse, inverse Cauchy, inverse Gaussian. When more than one function transformation was used, each function transformation was applied to the initial data, and then concatenated. The stacking method combines the PLS regression data from the desired binary classification and a secondary binary classification before a final PLS-DA (Figure 1).

2.3.3 Supervised Classification Methods

Species were classified by the presence or absence of the structural motifs in Table 2.5. Species possessing a structural motif were termed positive and assigned a value of 1, while species not possessing the motif were termed negative and assigned a value of 0. These 1s and 0s make up the binary y_{class} vector which is used as the dependent variable in the classification models.

Partial Least Squares Discriminant Analysis (PLS-DA)

The first step of PLS-DA is to perform a PLS regression on the training data, returning a non-binary matrix of predicted $\hat{y}$ values. In the discriminant analysis (DA) step, the values in the returned non-binary matrix are assigned as 1 or 0 by simple rounding, giving the binary classification of each species in $\hat{y}_{class}$.

Decision Tree Classifiers

Decision trees use training data to create a multi-layered tree of simple rules for sample classification. Each node contains a condition that determines to which subsequent node the sample proceeds. The last node a sample reaches gives the class label for the sample. Both RandomForestClassifier and ExtraTreesClassifier from SciKitLearn[44] create a number of decision trees using the training set that vote to select a class prediction. The key difference between the two decision tree classifiers applied in the present work is that, while the RandomForestClassifier selects an optimal split point at each node, the ExtraTreesClassifier selects a split point at random. Both RandomForestClassifier and ExtraTreesClassifier were applied directly to pre-processed data with default settings.

2.3.4 Binning

The dataset was divided into five spectral regions (9.65-8.22 eV, 8.22-7.16 eV, 7.16-6.35 eV, 6.35-5.7 eV, 5.7-5.17eV), each containing an equal number of photon energies. PLS-DA and the two decision tree classifiers with each pre-processing method, Function Transformations and Stacking, were applied to each sub-region of the spectra to obtain the accuracy, precision, and recall values reported. Binning analysis provides insight on which regions of the spectra are crucial to the accuracy of each classification model.

Chapter 3

Experimental Methods

The following sections summarize the experimental methods in the present work. The first section discusses the detection and quantification of intermediates and products from Cl-initiated oxidation of 2-ethyloxirane and the stereoisomers of 2,3-dimethyl-oxirane via multiplexed photoionization mass spectrometry (MPIMS) at the Advanced Light Source in Berkeley, CA. The methods used are also described in two publications on the same work by Doner et al. and Christianson et al.[20,21] The second section of experimental work discussed is method development for a vacuum ultraviolet (VUV) absorption spectroscopy diagnostic used for identification and quantification diagnostic for jet-stirred reactor experiments at the University of Georgia.[27,45] Over 100 reference measurements were taken, many for the first time.[46,47,48,24] In addition to providing reference measurements for species quantification in experiments, these measurements provide valuable benchmarks for computational chemists who desire to simulate absorption cross-sections in this region of wavelengths.

3.1 Multiplexed Photoionization Mass Spectrometry (MPIMS) Experiments

MPIMS provides a 3-dimensional dataset where signal intensity depends on time, photon energy, and mass-to-charge (m/z) ratio. Two-dimensional slices of this dataset give the mass spectrum within a selected range of photon energies and

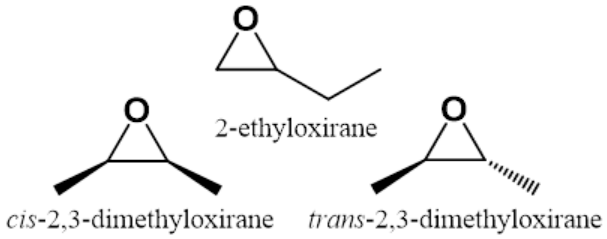

Figure 3.1: The chemical structures of the alkyl-substituted oxiranes studied via multiplexed photoionization mass spectrometry (MPIMS), 2-ethyloxirane, *cis*-2,3-dimethyloxirane, and *trans*-2,3-dimethyloxirane, are provided.

the photoionization spectrum at a selected m/z ratio. When reference data is available, these spectra are used to identify intermediate cations. When reference data is not available, the photoionization onset energy can be compared to theoretically computed adiabatic ionization energies.

3.1.1 MPIMS Reactor

The sample species in the present experimental work, here referred to generally as RH, are 2-ethyloxirane, *cis*-2,3-dimethyloxirane, and *trans*-2,3-dimethyloxirane (Figure 3.1). A dilute sample of each species is allowed to mix and react with dilute O_2 in a slow-flow quartz reactor. Experiments were conducted at 10 Torr and two different temperatures, 650 K and 800 K. The aforementioned temperatures were selected because they correspond to the two local maxima in cyclic ether concentration in previous *n*-butane combustion experiments.[49] Cl_2 gas is photolyzed by a 351-nm wavelength excimer laser. Instantaneously produced $Cl^{\bullet}$ initiates the $R^{\bullet} + O_2$ reaction by abstracting H from the sample species. The relative concentrations of reactants were selected to produce pseudo-first-order conditions. $[O_2]_0$ was four orders of magnitude larger than $[Cl^{\bullet}]_0$, which is approximately equal to $[R^{\bullet}]$ post-photolysis. To limit reactions between Cl_2 and $R^{\bullet}$, $[Cl_2]_0$ was two orders of magnitude smaller than $[RH]_0$.

3.1.2 Instrumentation

Intermediate species produce from R + O_2 travel through a 600 µm orifice on the side of the quartz reactor to the 10^{-8} Torr detector region where they are collimated into a near-effusive molecular beam. The molecular beam of intermediates are photoionized by orthogonal, tunable VUV synchrotron radiation, producing parent and fragment cations which are detected by an orthogonal time-of-flight (TOF) mass spectrometer.

3.2 Vacuum Ultraviolet (VUV) Absorption Spectroscopy

VUV absorption spectroscopy offers unparalleled isomer resolution, distinguishing constitutional and stereoisomers.[46,21,48] While the UV-vis wavelengths of light only excite electrons in conjugated -systems, the VUV wavelengths also excite electrons from -orbitals. Therefore, any species with bonds will absorb in this region of light. One limitation of experimental setup is that the VUV absorption diagnostic data not time-resolved. Samples are collected from experiments and subsequently measured after being separated by a gas chromatography (GC) column, which avoids excessive de-convolution procedures. In the case of co-elution, species can be deconvoluted and quantified by performing a linear fit of two or more reference measurements. The following sections describe the instrument used, sample preparation, reference measurement procedure, and associated uncertainty.[46]

Sample Preparation

Binary gas-phase mixtures of reference chemicals and He were prepared manometrically in 500 mL cylinders and supplied to the flow cell. High-purity liquid chemicals were degassed using the freeze-pump-thaw method then introduced in the gas phase into the cylinder at a prescribed initial pressure, typically 1 Torr, diluted with ultra-high purity He to

nominal concentrations between 50 and 200 ppm, and statically mixed for at least 2 h.

Instrumentation

Differential absorption spectroscopy measurements were conducted in the gas phase using a temperature- and pressure-controlled flow cell with a pathlength of 10 cm. For all experiments, the conditions in the flow cell were 800 Torr and 50 °C. A deuterium (D_2) lamp is the source of white light, which is directed through the flow cell using high-reflectivity mirrors located at the inlet and exit. The mirror positioned at the exit of the flow cell directs unabsorbed white light onto a diffraction grating, which provides high-resolution separation (<4 meV) of the light onto a CCD detector that produces output voltages corresponding to wavelength. The environment inside of the flow cell and around the optical path is controlled to remove ambient N_2, O_2, and H_2O via inert purging.

Procedure for Reference Measurements

Prior to each absorption measurement, a reference scan (to measure background absorbance) and a dark scan (with the D_2 lamp blocked) were performed sequentially using He flow for 1 min. to enable background-subtraction and proper determination of I_0. The mixture is introduced to the flow cell and allowed to reach steady state concentration. The sample is then flowed for an additional 5 minutes. Time-averaged absorption signals were then measured. Between measurements of different sample species, the flow cell was purged with ultra-high-purity N_2 until no residual signal remained, and the manifold from which the gas-phase mixtures were supplied was placed under vacuum for at least 15 min.

Statistical Analysis

To quantify absorption cross-sections as a function of photon energy, $\sigma(E)$ (cm^2), the Beer-Lambert law (Equation 3.1) was applied where A is the absorbance, I_0 is the incident intensity of the white light, $I(E)$ is the residual intensity after passing through the flow cell, L is pathlength (cm), and N

(molecules cm^{-3}) is the gas-phase number density of absorbing species determined at the temperature of the flow cell (50 °C) using partial pressure calculations. Units for absorption cross-sections are reported in megabarns (Mb); 1 Mb = 10^{-18} cm^2.

$$\sigma(E) = \frac{A(E)\ln(10)}{NL} = \log\frac{I_0}{I(E)}\frac{\ln(10)}{NL} \tag{3.1}$$

The absorption measurements were repeated 3-5 times within the steady state region. Two main sources of experimental uncertainty were quantified: (1) gas-phase concentration within the absorption region and (2) experimental repeatability. Details and methods for calculating both types of uncertainty are outlined by Doner et al.[46] The largest source of uncertainty in the gas-phase concentrations is the chemical purity and the maximum uncertainty in the measured cross-sections is 5%. The standard-error-to-average ratio, $r_{\epsilon,\bar{x}(E)}$, given by Equation 3.2 is used as a measure of repeatability where $\bar{x}$ is the mean, $\epsilon(E)$ is the standard error, $s(E)$ is the standard deviation, and n is the number of measurements averaged.

$$r_{\epsilon,\bar{x}(E)} = \frac{\epsilon(E)}{\bar{x}(E)} = \frac{1}{\bar{x}(E)}\frac{s(E)}{\sqrt{n}} = \frac{1}{\bar{x}(E)}\frac{1}{\sqrt{n}}\sqrt{\frac{\sum(x(E)-\bar{x}(E))^2}{n-1}} \tag{3.2}$$

For spectral regions above a threshold of 2% of maximum absorbance, a standard-error-to-average ratio of <5% was typical.

Chapter 4

Alkyl-Substituted Oxiranyl Radicals + O_2

2-ethyloxirane and 2,3-dimethyloxirane are alkyl-substituted, three-membered cyclic ethers, which have been detected experimentally in low-temperature combustion of *n*-butane.[50,51,49,52] The barrier heights for formation of 2-ethyloxirane + OH from 2-hydroperoxy-1-butyl and 1-hydroperoxy-2-butyl are 11.0 kcalmol^{-1} and 11.3 kcalmol^{-1}, respectively.[26] The barrier heights for formation of *syn*- and *anti*-2,3-dimethyloxirane are 9.9 kcalmol^{-1} and 10.3 kcalmol^{-1}, respecitvely.[26] These barrier heights were previously under-predicted, likely due to the use of CBS-QB3,[53] resulting in over-predicted steady-state concentrations of alkyl-substituted oxiranes in JSR experiment.

Doner et al.[20] and Christianson et al.[21] investigated consumption reactions of 2,3-dimethyloxirane and 2-ethyloxirane, including reaction with O_2. Potential energy surfaces, including ring opening pathways in addition to conventional ROO- and QOOH-mediated pathways, were constructed at the ccCA-PS3[37] level of theory. The stereoisomers of 2,3-dimethyloxirane, *cis* and *trans*, were treated separately. Barriers to inversion of tertiary radicals, yielding the opposite stereoisomer were also calculated. T1 diagnostics were generally less than 0.04 with the exceptions several transition states corresponding to several HO_2 elimination transition states, both concerted and sequential, one ROO $\longrightarrow$ QOOH transition state forming the *cis*-$\alpha\beta'$-QOOH from *cis*-2,3-dimethyloxirane, and two cyclic ether formation transition states. Interme-

diates of Cl-initiated oxidation each isomer were identified andquantified via multiplexed photoionization mass spectrometry (MPIMS).

4.1 Alkylperoxy (ROO) Radical Pathways

Unimolecular reactions of alkylperoxy radicals include dissociation to R + O_2, concerted HO_2-elimination, or internal H-abstraction forming hydroperoxyalkyl (QOOH) radicals. The barrier heights for these pathways investigated by Doner et al.[20] and Christianson et al.[21] are summarized by Figure 4.1.

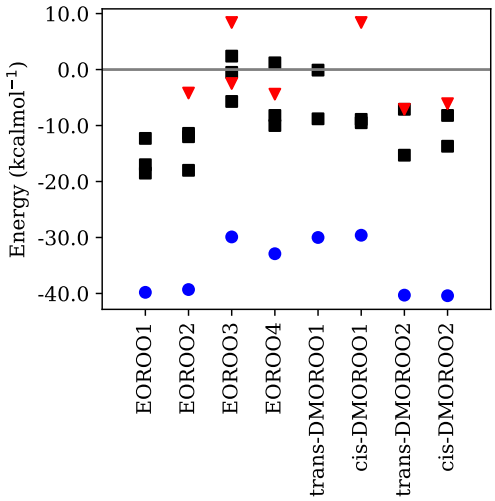

Figure 4.1: The barrier heights relative to R + O_2 (gray line) for each of the pathways for each of the alkylperoxy radicals produced from O_2-addition to 2-ethyloxiranyl (left) and 2,3-dimethyloxiranyl (right) radicals are given. In black is internal H-abstraction yielding QOOH. In red is concerted HO_2-elimination. In blue is the welldepth of the peroxy radical.

Dissociation to R + O_2 and HO_2-elimination are chain-inhibiting pathways in low-temperature combustion because they compete with the formation of QOOH and second O_2-addition, which lead to chain branching. Because of the barrierless entrance channel, for which basic transition state theory is not appropriate, the dissociation to R + O_2 was not studied theoretically. However, there are a multitude of submerged pathways for each of the ROO radicals studied, and

the detection of several QOOH decomposition products via MPIMS suggest that dissociation to R + O_2 is not a major pathway under the selected conditions.

HO_2-elimination pathways were found for every ROO and β-QOOH, except for those with products containing a double bond within the oxirane ring. Examples of missing HO_2-elimination pathways are given by Figure 4.2. In general, barrier heights for concerted HO_2-elimination from ROO were higher than some or all internal H-abstraction pathways producing QOOH, which were nearly all submerged below R + O_2. A comparison of the barrier heights for all of the alkylperoxy radicals produced from O_2-addition to 2-ethyoxiranyl and 2,3-dimethyloxiranyl radicals is given by Figure 4.1.

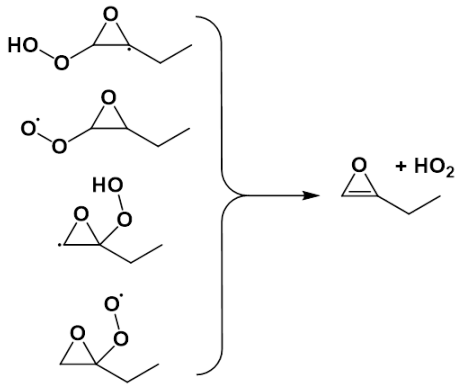

Figure 4.2: The transition states for each of the pathways shown leading to 2-ethyloxirene and HO_2 were not found, likely due to the high ring strain in the 2-ethyloxirene.

The lowest internal H-abstraction pathways form δ-QOOH radicals through favorable 6-membered transition states, as observed in various other works concerning low-temperature combustion of alkanes.[54] The stereochemistry of 2,3-dimethyloxirane ROO radicals prohibited certain internal H-abstraction reactions. For example, β,α'-QOOH can be formed from only the *trans* isomer of β-ROO, while $\beta\beta'$-QOOH can only be formed from the *cis* isomer of β-ROO (Figure 4.3). However, ROO radicals with tertiary radical centers can undergo inversion, for which the barrier heights are typically 6-7 kcal/mol. In this way, inversion reactions mitigate stereochemical effects on the mechanism of 2,3-dimethyloxirane.

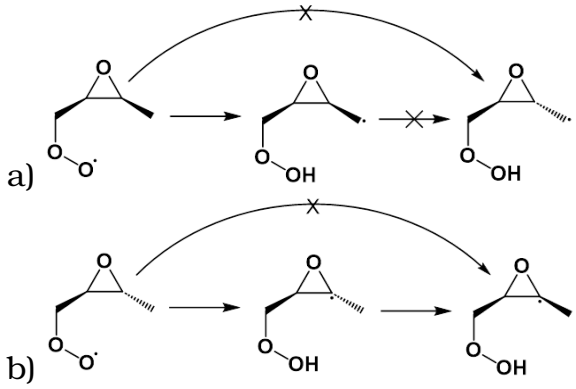

Figure 4.3: Due to steric restrictions, $\beta\beta'$-QOOH can only be formed from the *cis* isomer of β-ROO (a), while β,α'-QOOH can be formed from only the *trans* isomer of β-ROO (b). However QOOH species with the radical center positioned on one of the carbons forming the oxirane ring,, can undergo facile inversion. For example,*trans*-$\beta\alpha'$-QOOH in the middle of the (b) scheme can invert to *cis*-$\beta\alpha'$-QOOH over a 6.9 kcal/mol barrier.

4.2 Alkylhydroperoxy (QOOH) Radical Pathways

Alkylhydroperoxy (QOOH) radicals either undergo conventional QOOH-mediated pathways, including HO_2-elimination and cyclic ether formation, or ring opening reactions. The barrier heights for QOOH-mediated pathways are summarized by Figure 4.4.

Cyclic ether formation pathways were found for all QOOH species except those for which the product contains two oxirane rings which share two carbons (Figure 4.5). The barrier heights for sequential HO_2-elimination, which are mostly between 15 kcal/mol and 30 kcal/mol, are similar to the barrier heights for cyclic ether formation.

Ring opening via C-O bond scission can yield either ketohydroperoxyalkyl radicals or dicarbonyls and OH. Dicarbonyls are formed when the ketohydroperoxyalkyl radical that ring opening would produce is an α-QOOH, in which the radical

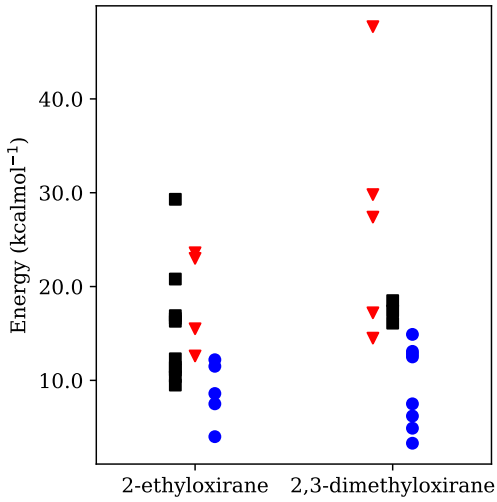

Figure 4.4: The barrier heights for alkylhydroperoxy radicals formed from O_2-addition to 2-ethyloxiranyl (left) and 2,3-dimethyloxiranyl (right) radicals are given where black squares represent cyclic ether formation barriers, red triangles represent sequential HO_2-elimination barriers, and blue circles represent ring opening barriers.

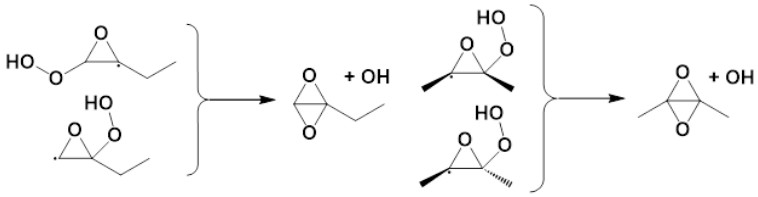

Figure 4.5: The transitions states were not found for three pathways forming bicyclic ethers in which two oxirane rings share two carbons. This is likely due to the high ring strain of the products.

center and hydroperoxy group are on positioned the same carbon. α-QOOH radicals are known to be unstable.[32] One ring opening pathway via C-C bond scission was found for α,α'-QOOH which simultaneously loses OH, giving vinyl acetate (Figure 4.6).

Because of the difficulty of quantifying highly reactive ketohydroperoxides,[55] dicarbonyls are commonly used as proxy species attributed to ketohydroperoxide decomposition. There-

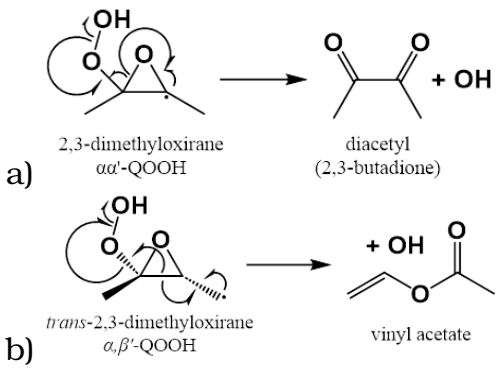

Figure 4.6: Ring opening and OH-loss occur in the same step for the $\alpha\alpha'$-QOOH and $\alpha\beta'$-QOOH radicals from 2,3-dimethyloxirane because of the instability of the α-QOOH radicals which would be formed from ring opening alone. In (a), diacetyl can be formed from the *cis*- or *trans*-$\alpha\alpha'$-QOOH from 2,3-dimethyloxirane α-peroxy radicals. In (b), vinyl acetate can be formed from *trans*-$\alpha\beta'$-QOOH from 2,3-dimethyloxirane.

fore, it is critical to be aware of alternative pathways producing dicarbonyls, so that ketohydroperoxide production is not overestimated. Ring opening of the $\alpha\alpha'$-QOOH from 2,3-dimethyloxirane yields diacetyl and OH. Although $\alpha\alpha'$-QOOH can only be formed from the *cis* isomer of α-ROO, *trans*-$\alpha\alpha'$-QOOH can be formed via inversion and undergo ring opening.

Due to the ring size of oxirane, the ketohydroperoxyalkyl radicals produced via ring opening of alkyl-substituted oxirane QOOH radicals are always resonance-stabilized alkylvinoxy radicals.[56,57] This detail, in addition to high ring strain, helps to rationalize the low barrier heights and exothermic products (30-60 kcal/mol) of ring opening pathways.

4.3 Detected Intermediates

The detection of several intermediates via MPIMS[20,21] bolster the computational results discussed in the previous sections.

4.3.1 2-Ethyloxirane + O_2

For the 2-ethyloxirane oxidation experiments, intermediates detected at m/z 70, 86 and 103 indicate peroxy radical chemistry. The m/z 70 corresponds to peroxy radical decomposition products coincident with HO_2. These products include vinyl oxirane and 2-butenal. Four HO_2-elimination pathways to vinyl oxirane were found, including concerted and sequential pathways (Figure 4.7).

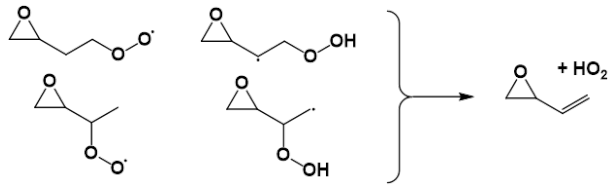

Figure 4.7: Vinyl oxirane (m/z) can be formed from two different peroxy radicals via concerted HO_2-elimination and two different alkylhydroperoxy radicals via sequential HO_2-elimination.

In the photoionization spectrum obtained at m/z 70, the onset photon energy is approximately 9.5 eV, which matches that of vinyl oxirane. However, based on reference measurements, vinyl oxirane does not account for all of the signal at m/z 70.[21] The remaining signal may arise from 2-butenal, which has an adiabatic ionization energy of 9.8 eV.[47] 2-butenal could be formed from HO_2-elimination from the ketohydroperoxyalkyl radical in Figure 4.8.

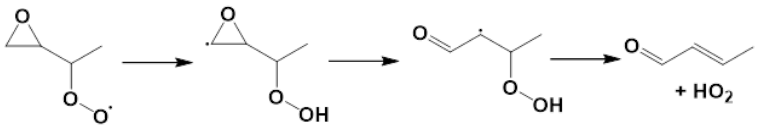

Figure 4.8: 2-butenal appears at the same m/z as vinyl oxirane. The proposed formation pathway, which involves formation of QOOH, ring opening, and then HO_2 elimination, is shown.

The m/z 86 corresponds to peroxy radical pathways resulting in loss of OH, such as cyclic ether formation. The photoionization spectrum obtained at m/z 86 is a linear combination of the photoionization spectra from tetrahydrofuran-

3-one and 2,2'-bioxirane. There are two pathways from 2-ethyloxirane QOOH radicals forming 2,2'-bioxirane with barrier heights of 10 kcal/mol and 12 kcal/mol (Figure 4.9).

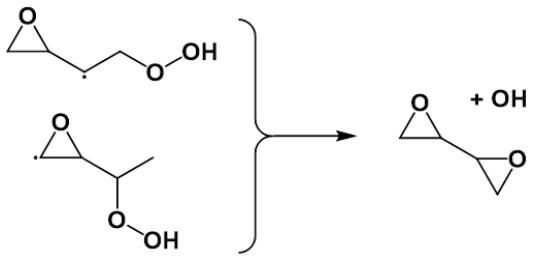

Figure 4.9: Two 2-ethyloxirane QOOH radicals decompose to form 2,2'-bioxirane which was detected at m/z 86. The barrier height for the top QOOH species is 12 kcal/mol while the barrier height for the bottom QOOH species is 10 kcal/mol.

The pathway to tetrahydrofuran-3-one was not part of the potential energy surfaces in the previous sections. However, cyclic ether formation is a plausible pathway for the keto-hydroperoxylalkyl radical resulting from ring opening of a 2-ethyloxirane QOOH radical (Figure 4.10).

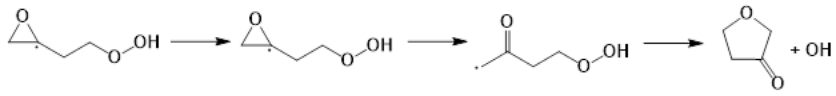

Figure 4.10: Tetrahydrofuran-3-one was detected at the same m/z as 2,2'-bioxirane. Given here is the proposed pathway for its formation from 2-ethyloxetane QOOH radical decomposition via ring opening and cyclic ether formation.

4.3.2 2,3-Dimethyloxirane + O_2

In the *cis*- and *trans*-2,3-dimethyloxirane experiments, only acyclic species were detected. Three acyclic species detected can be attributed to QOOH-mediated pathways. The first was methyl vinyl ketone (m/z 70) which was not part of the potential energy surfaces in the previous sections, but could be formed via HO_2-elimination from a QOOH species that has undergone ring opening (Figure 4.11). Two m/z 86 species from the potential energy surfaces discussed in the previous sections, diacetyl and vinyl acetate. Both are formed

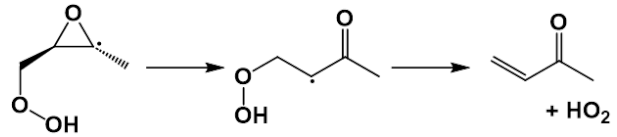

Figure 4.11: Methyl vinyl ketone (m/z 70) was detected in oxidation of both *cis*- and *trans*-2,3-dimethyloxirane. The proposed pathway for its formation is ring opening of $\beta\alpha'$-QOOH and HO_2-elimination.

via ring opening of QOOH and simultaneous OH loss from the hydroperoxy group (Figure 4.6). Although many of the same species were identified in both of the *cis*- and *trans*-2,3-dimethyloxirane experiments, there were significant differences in the relative yields. For example, ketene was only detected for the *cis* isomer, and all of the relative yields for the *cis* isomer were larger than that of the *trans* isomer. This is due to the combination of steric restrictions mitigated by inversion of the tertiary radicals.

Chapter 5

Unimolecular Decomposition of Alkyl-Substituted Oxetanyl Radicals

The steady-state concentration of cyclic ethers in low-temperature combustion depends not only on their rate of formation from QOOH, but also on their rate of consumption. High-level theoretical rate coefficients for the formation of 2,4-dimethyloxetane and 2-ethyloxetane have been calculated, refined, and incorporated into the latest chemical kinetics mechanism for low-temperature combustion of *n*-pentane.[15,26] In the same mechanism, however, the consumption of 2,4-dimethyloxetane and 2-ethyloxetane are represented by several plausible elementary steps combined into one with estimated rate coefficients. Breaking these reactions into elementary steps opens up many more pathways, several of which are significant. In the prescribed consumption reactions for 2,4-dimethyloxetane and 2-ethyloxetane, H-abstraction is only considered from oxygen-adjacent carbons. In the present work, every possible radical resulting from H-abstraction was considered. Secondly, only C-O bond scission is considered by the current mechanism. In the present work, ring opening by C-C bond scission was also considered. Finally, only one β-scission pathway was considered per ring-opened radical, whereas KinBot finds all reactions of the ring-opened radicals that

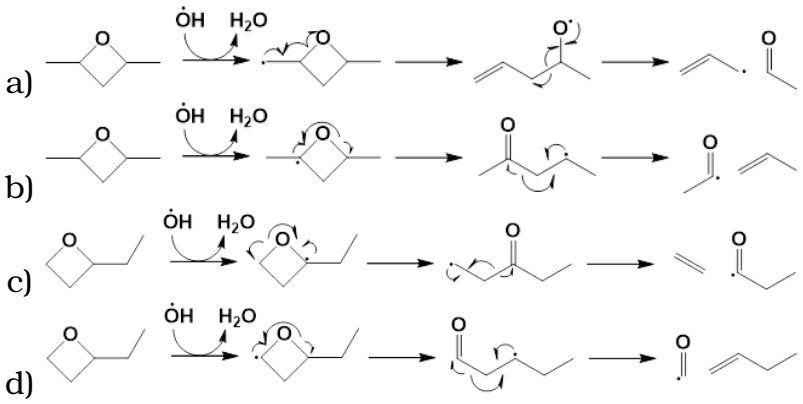

Figure 5.1: The consumption pathways for 2,4-dimethyloxetane and 2-ethyloxetane from Bugler et al.[15] are broken into elementary steps. There are plausible alternative steps for each elementary step shown, including H-abstraction from different carbons, ring opening via C-C bond scission, and other β-scission steps.

meet the inclusion criteria described in the Computational Methods chapter. The first section discusses the potential energy surfaces of the most dominant pathways and general trends. In the Appendix, the full potential energy surfaces are given. The second section compares the highest several theoretical rate coefficients computed for each initial radical. The final section provides theoretical branching fractions under conditions relevant to combustion experiments. These branching fractions can act as a target for experimentalists to replicate.

5.1 Unimolecular Decomposition Mechanisms

The potential energy surfaces for the DMOR and EOR radicals mainly consists of four types of reactions, ring opening, H-shifts, 1,2-functional group shifts, and β-scission. Ring opening can occur via C-O bond scission or C-C bond scission. C-O bond scission almost always has a lower barrier than C-C bond scission. However, ring opening via C-C bond

scission is still significant in several cases. Some examples of included C-C bond scission ring opening pathways are given in Figure 5.2, The barrier heights for ring opening of EOR4 and DMOR1 are approximately half of that of EOR1. This could be attributed to the radical position in the initial radical. Both EOR4 and DMOR1 have radical centers one carbon removed from the oxetane ring.

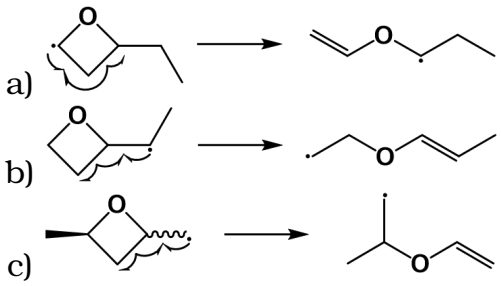

Figure 5.2: In (a) and (b) the included ring opening pathways that occur via C-C bond scission for 2-ethyloxetanyl radicals are shown. In (c), the same is shown for 2,4-dimethyloxetanyl. The barrier heights for (a), (b), and (c) are 33 kcal/mol, 15 kcal/mol, and 16 kcal/mol, respectively.

Ring opening was only significantly exothermic when it yielded a ketoalkyl radical as shown in Figure 5.3. The C-O bond scission ring opening steps for EOR3, EOR1, and DMOR2 are 20 kcal/mol, 17 kcal/mol, and 18 kcal/mol exothermic, respectively. Ring opening EOR1 produces 1-pentanal-3-yl, the mechanism for which has been studied by Singh et al.[58] Ring opening of the tertiary radical of 2-ethyloxetane, EOR3, decomposes to 3-pentanone-1-yl which has been studied by Dames et al.[59] The major products, propanal-1-yl + ethylene agree with this work. Two additional pathways are included in the present work; however, they produce the same end products. Ring opening pathways forming unsaturated alkoxy and ether radicals were usually within 5 kcal/mol of the closed ring reactant.

Analogous ring opening pathways for DMOR diastereomers had the same barrier heights within 0.5 kcal/mol. Potential energy surfaces for these reactions are provided in the Appendix. All of the acyclic ring opening products have at most 1 chiral center, making them energetically identical enan-

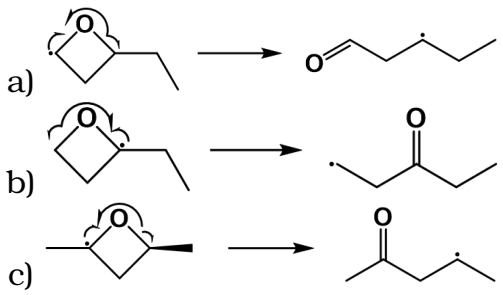

Figure 5.3: The exothermic ring opening steps included for 2-ethyloxetanyl radicals and 2,4-dimethyloxetanyl radicals, in which the radical center is always adjacent to oxygen, are shown. The barrier heights for C-O bond scission ring opening of (a) EOR1, (b) EOR3, and (c) DMOR3 are 27 kcal/mol, 27 kcal/mol, and 26 kcal/mol, respectively, and they are 17 kcal/mol, 20 kcal/mol, and 18 kcal/mol exothermic, respectively.

tiomers. Therefore, in the following sections, only the *syn*-diastereomer rate coefficients and branching fractions are shown. The *anti* diastereomer plots are included in the Appendix.

There are several pathways for acyclic radicals which result in a 1,2-functional group shift. Many of these involve an intermediate well, which contains a three-membered ring. These instances shown in Figure 5.4 are described here. In the potential energy surface for the secondary DMOR3 radical, 2-penten-4-oxy has a ring closure pathway forming 1-(3-methyloxiran-2-yl)ethan-1-yl. There is no pathway meeting the inclusion criteria from 1-(3-methyloxiran-2-yl)ethan-1-yl apart from the reverse reaction. However, this reaction could be interpreted as a cis-trans isomerization analogous to inversion reaction for alkyl-substituted oxirane radicals.[20] In the present work, *cis* and *trans* alkenes were not treated separately, so further investigation of its effect on the kinetics is needed. Another ring closure pathway on the secondary DMO radical surface forms 1-methylyl-2-methyl-3-hydroxycyclopropane, which can undergo exothermic ring opening reaction, producing the branched species, 2-methylbut-

3-en-1-ol-1-yl. The intermediate well corresponding to 1-methylyl-2-methyl-3-hydroxycyclopropane has a well depth of approximately 6 kcal/mol on each side. Similarly, in the merged potential energy surface for EOR1, EOR2, and EOR5, 2-penten-4-ol-5-yl closes to form 1-hydroxy-2-(1-ethyl)cyclopropane, which opens to form 2-penten-5-ol-5-yl, and 1-penten-1-ol-4-yl closes to form 1-methyl-2-(methanol-1-yl)cyclopropane, which opens to form 1-buten-1-ol-4-methyl-5-yl. The detection of branched species from these channels in combustion experiments may falsely suggest the presence of *iso*-pentane.

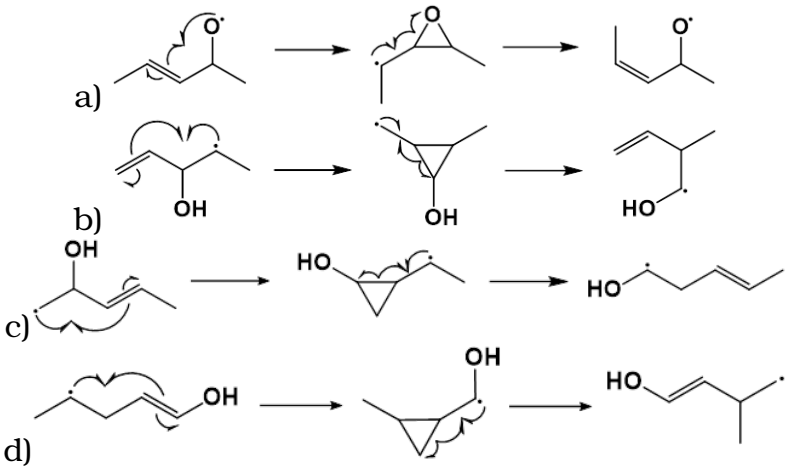

Figure 5.4: Several β-alkene and β-alkenoxy radicals undergo ring closure forming a substituted 3-membered ring with a shallow (<10 kcal/mol) well. Upon ring opening, these species can yield opposite conformers or branched species. The pathways in (a) and (b) are part of the DMOR3 and EOR4 potential energy surfaces. The pathways in (c) and (d) are part of the EOR1, EOR2, and EOR5 potential energy surfaces.

The potential energy surfaces of 2-ethyloxetanyl and 2,4-dimethyloxetanyl radicals have several networks of H-shift reactions for acyclic radicals which have low energy barriers compared to β-scission reactions. These H-shift reactions occur via loose five-, six-, or seven-membered transition states. Some examples are shown by Figure 5.5. These reactions are responsible in part for the large size of the potential energy surfaces in the present work.

The pathway forming pentanal-1-yl and ethylene in the *n*-pentane mechanism from Bugler et al.[15] was found and

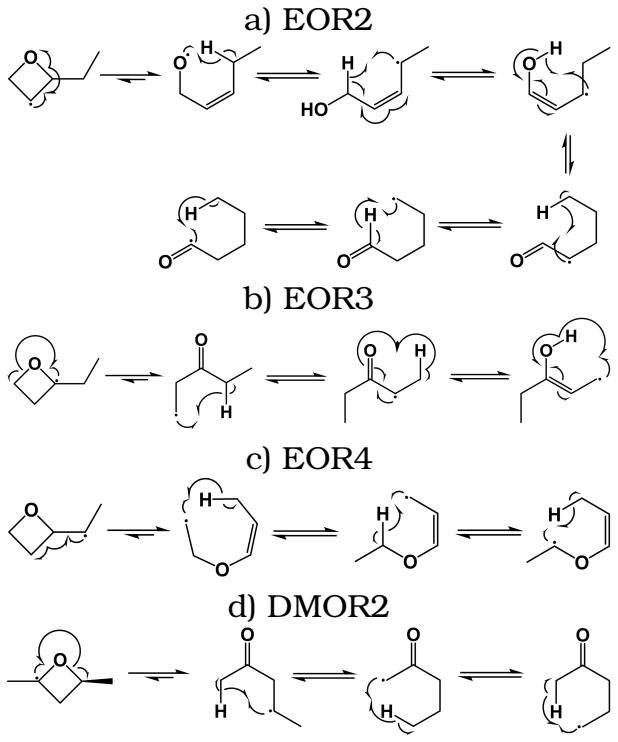

Figure 5.5: Networks of H-shift reactions on the potential energy surfaces for (a) EOR2, (b) EOR3, (c) EOR4, and (d) DMOR2 are shown.

included in the present work. The tertiary EOR3 radical undergoes exothermic ring opening via C-O bond scission over a 27 kcal/mol barrier followed by β-scission over a 24 kcal/mol barrier, giving ethylene and pentanal-1-yl. The pathway forming formyl radical and 1-butene from 2-ethyloxetane included in the *n*-pentane mechanism from Bugler et al.[15] was found but excluded due to a low branching fraction (<5%) from the 1-pentanon-3-yl well. Compared to the included 1,2-acyl migration pathway from the same well with a barrier of 10 kcal/mol, the formation of formyl radical and butene has a 26 kcal/mol barrier at the L2= ωB97XD/6-311++G(d,p) level of theory.

5.2 Theoretical Rate Coefficients

Theoretical rate coefficients were calculated between 300 K and 1000 K at the pressures, 0.01 atm, 0.1 atm, 1 atm, 10 atm, and 100 atm. The following Figures 5.6-5.9 show the largest several rate coefficients at 1 atm across the entire temperature range. Some rate coefficients disappear at higher temperatures where the reaction rate is faster than the rate of collisional stabilization. It should be noted that this could introduce non-Boltzmann effects, which may require different techniques to capture accurately.[60]

Figure 5.6 gives the highest several rate coefficients for each *syn* DMOR radical at 1 atm. The rate coefficients for *anti*-DMOR1 and *anti*-DMO3 are near identical and included in the Appendix. For the primary DMOR1 radical, the highest rate coefficient by approximate two orders of magnitude ($\sim 10^8$ s^{-1} at 700 K) across the entire temperature range is formation of allyl and acetaldehyde by skipping the 1-penten-4-oxy well. There is also a well skipping pathway giving vinoxy radical and propene which is $\sim 10^6$ s^{-1} at 700 K. For the tertiary DMOR2 radical, the rate coefficient for 2-pentan-4-yl is the largest below 600 K, where the rate coefficient for well skipping producing acetyl and propene is higher. For the secondary DMOR3 radical, the highest rate coefficient is the one corresponding to C-O bond scission ring opening and H-shift from the distal primary carbon to the oxy group, which yields pent-3-en-2-ol-5-yl. The second highest is the one cor-

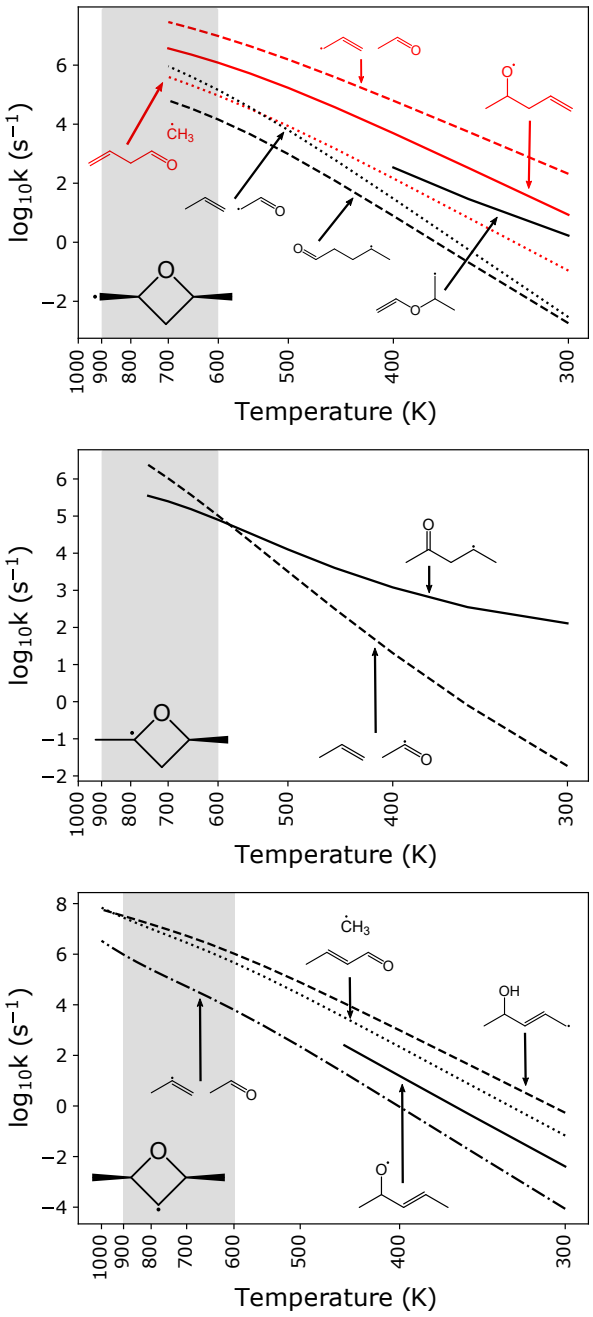

Figure 5.6: The highest several rate coefficients for the *syn* diastereomers of each DMOR radical, (a) *syn*-DMOR1, (b) DMOR2, and (c) *syn*-DMOR3 are given between 300 K and 1000 K at 1 atm. Well skipping reactions are denoted by dotted or dashed lines.The shaded region between 600 K and 900 K denotes the temperature range in which 2,4-dimethyloxetane has been detected in jet-stirred reactor experiments.[15]

responding to C-O bond scission ring opening and β-scission giving methyl and 2-butenal.

Figure 5.7 gives the highest several rate coefficients for EOR1, EOR2, and EOR5, which have many pathways in common. The largest rate coefficient for EOR1 across the entire temperature range is exothermic ring opening via C-O bond scission, which yields 1-pentanal-3-yl. The rate coefficient for C-O bond scission ring opening followed by 1,2-acyl migration is the second largest below 650 K. The rate coefficients for both of the aforementioned pathways from EOR1 demonstrate strong non-linear temperature dependence. Above 650 K, the rate coefficient for ring opening of EOR1 via C-C bond scission followed by β-scission, giving acrolein and ethyl is the second largest. The rate coefficients for ring opening of EOR1 via C-C bond scission without well skipping and H-transfer from the primary carbon are below 10^5 s^{-1} for entire temperature range. For EOR2, the highest rate coefficient corresponds to ring opening via C-O bond scission followed by H-shift, giving pent-3-en-1-ol-2-yl. Above 500 K, the second-highest rate coefficient is for a well-skipping pathway yielding acrolein and methyl. For EOR5, the rate coefficient for H-shift from the oxygen-adjacent secondary carbon is 1-2 orders of magnitude larger than the rate coefficient for H-shift from the proximal secondary carbon. This can be rationalized by the larger size of the transition state. Well-skipping rate coefficients are competitive with stepwise rate coefficients in the higher temperature region (>800 K).

Figure 5.8 gives the highest three rate coefficients for EOR3. Below 600 K, the largest rate coefficient is ring opening via C-O bond scission, which yields 3-pentanone-1-yl. Above 600 K, the well skipping rate coefficients giving butanal-1-yl and ethylene is higher than the stepwise rate coefficient. This strongly resembles the rate coefficients for ring opening and β-scission of DMOR2 in Figure 5.6b.

Figure 5.9 shows that the largest rate coefficient for EOR4 corresponding to ring opening via C-O bond scission and β-scission giving 1-buten-3-yl and formaldehyde. The stepwise rate coefficient for ring opening of EOR4 via C-O bond scission is approximately two orders of magnitude slower than the

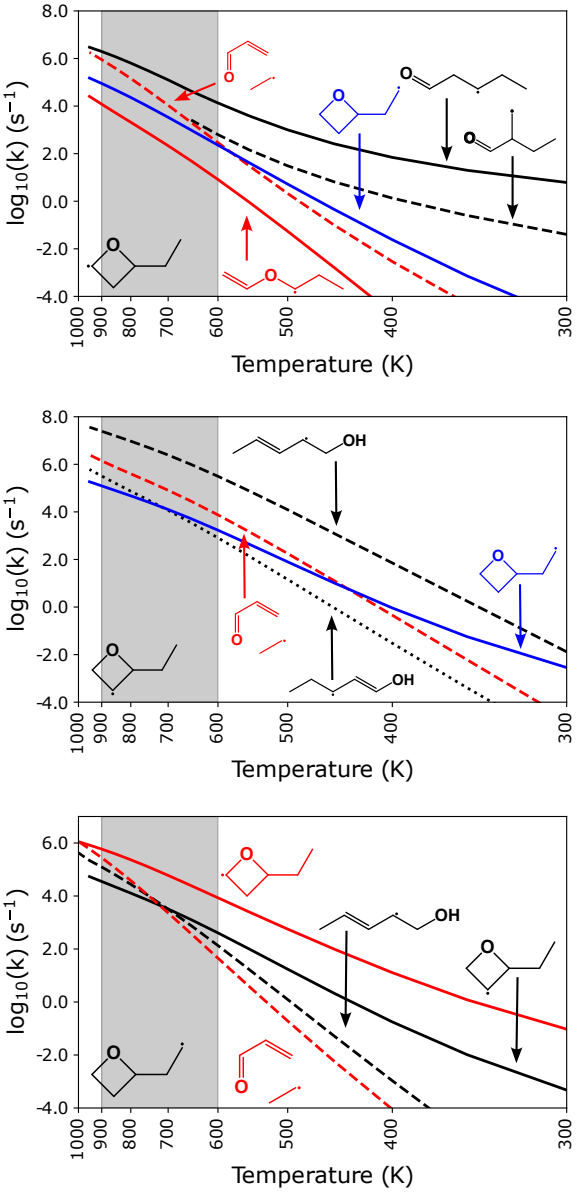

Figure 5.7: The highest several rate coefficients are given for EOR1, EOR2, and EOR5. Well skipping reactions are denoted by dotted or dashed lines. The shaded region between 600 K and 900 K denotes the temperature range in which 2-ethyloxetane has been detected in jet-stirred reactor experiments.[15]

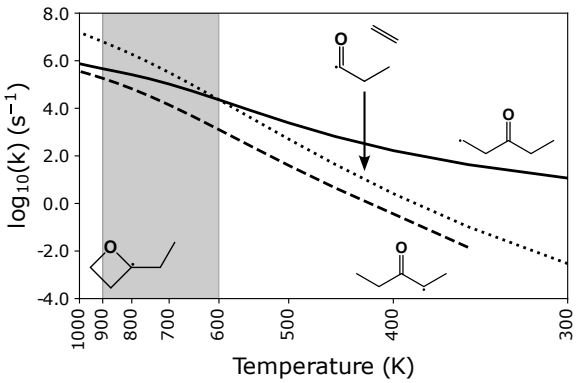

Figure 5.8: The highest three rate coefficients are given for EOR3. Well skipping reactions are denoted by dotted or dashed lines.The shaded region between 600 K and 900 K denotes the temperature range in which 2-ethyloxetane has been detected in jet-stirred reactor experiments.[15]

well-skipping rate coefficient. The stepwise rate coefficients for ring opening via C-C bond scission is competitive with C-O bond scission. However, the rate coefficient for well-skipping and β-scission, yielding 2-methylvinoxy radical and ethylene is lower than the stepwise rate coefficient for ring opening C-C bond scission.

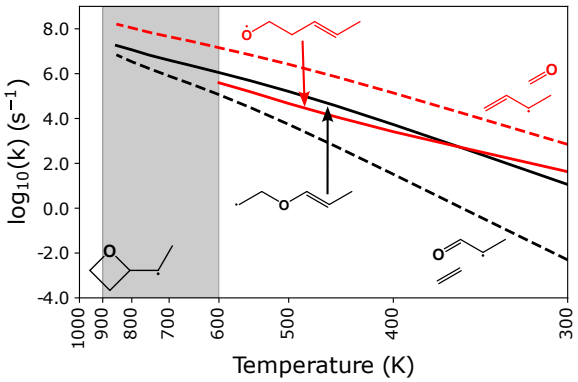

Figure 5.9: The highest four rate coefficients are given for EOR4. Well-skipping reactions are denoted by dotted or dahsed lines.The shaded region between 600 K and 900 K denotes the temperature range in which 2-ethyloxetane has been detected in jet-stirred reactor experiments.[15]

For both 2-ethyloxetanyl and 2,4-dimethyloxetanyl radicals, the rate coefficients are highest for species with the radical center located at the 3-position on the oxetane ring. The maximum rate coefficients for both EOR2 and DMOR3 are $\sim 10^8$ s^{-1}, while the remaining radicals have maximum rate coefficients of approximately 10^6 s^{-1} or 10^7 s^{-1}.

The total rate coefficient for unimolecular decomposition of each carbon-centered radical derived from H-abstraction from 2-ethyloxetane and 2,4-dimethyloxetane at atmospheric pressure and three temperatures (500 K, 650 K, 800 K) are given by Figure 5.10. The radicals DMOR1 and EOR4 have radical centers positioned on alkyl substituents directly adjacent to the oxetane ring. This radical position corresponds to low barrier heights for ring-opening and the largest total rate coefficients. DMOR3 and EOR2 have radicals centers in the 3-position of the oxetane ring. These radicals have intermediate total rate coefficients. DMOR2, EOR1, and EOR3, have radical centers directly adjacent to the ether group. This corresponds to relatively high energy barriers for ring-opening and low total rate coefficients. Finally EOR5 has the lowest total rate coefficient because it has no direct ring-opening pathways. Instead, EOR5 undergoes an internal H-abstraction forming either EOR1 or EOR2.

5.3 Theoretical Branching Fractions

Theoretical branching fractions were calculated for each alkyl-substituted oxetanyl radical. The conditions selected are typical for jet-stirred reactor experiments from the Rotavera Laboratory.[45,27] The time selected was 20 ms and the pressure selected was 1 atm. Figures 5.11-5.13 show the branching fractions for the *syn* diastereomer of each DMOR radical. For *syn*-DMOR1, the major product (>80%) is allyl and acetaldehyde. Propene and vinoxy radical are minor products with a maximum branching fraction of $\sim$10% at 700 K.

Propene and acetyl are the major products for DMOR2, making up 100% of the yield above 450 K. Below 450 K, the remainder of the yield is 2-pentanone-4-yl, which is produced from ring opening via C-O bond scission.

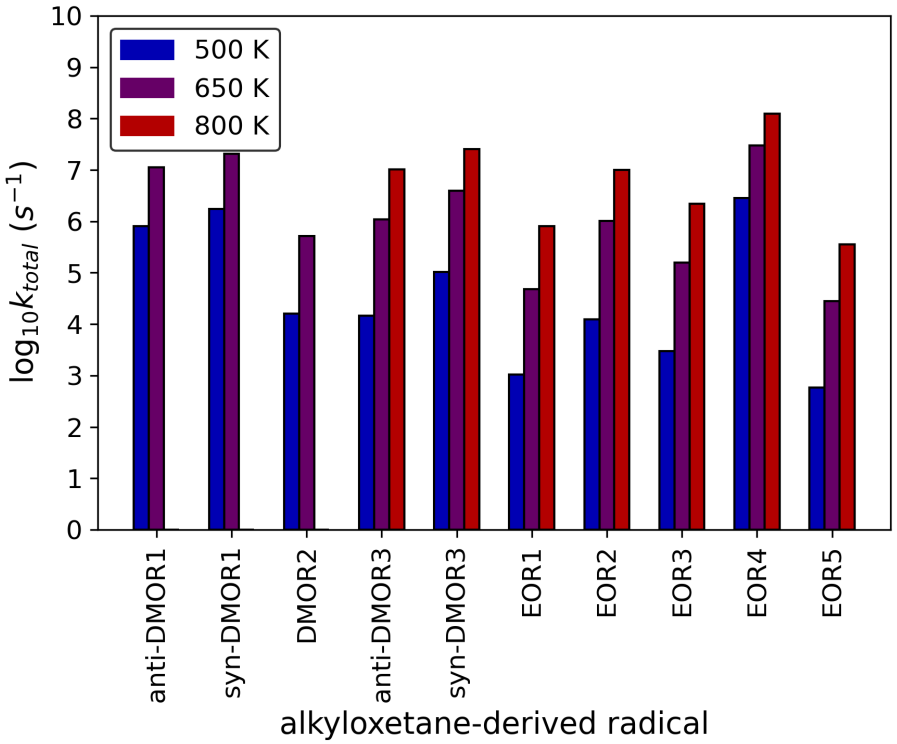

Figure 5.10: The total rate coefficient at 1 atm for unimolecular decomposition of each radical is given at 500 K (blue), 650 K (purple), and 800 K (blue). Rate coefficients at 800 K are missing for DMOR1 and DMOR2 due to disappearing values in the master equation solution.

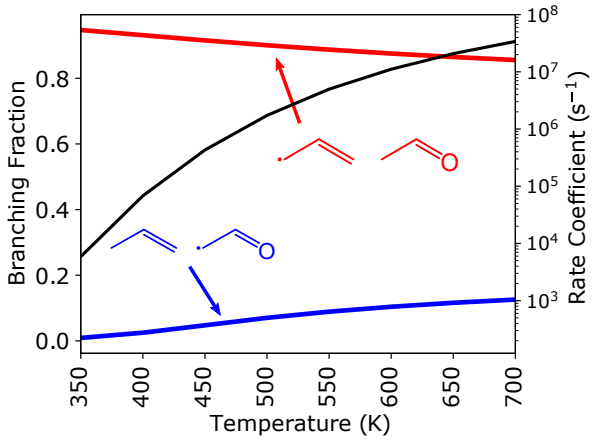

Figure 5.11: The branching fractions at 1 atm and 20 ms for *syn*-DMOR1 are shown between 300 K and 850 K.

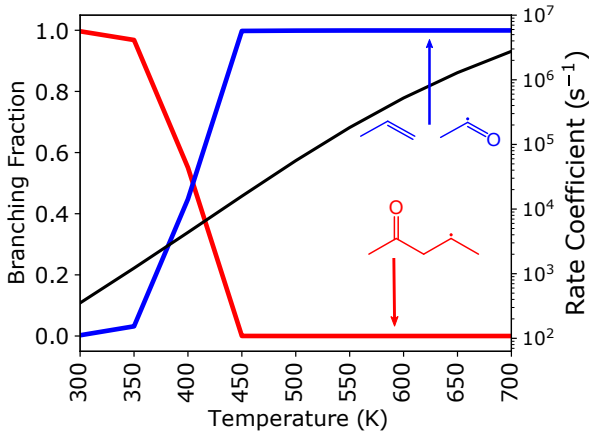

Figure 5.12: The branching fractions under at 1 atm and 20 ms for DMOR2 are shown between 300 K and 850 K.

Below 600 K, where the total rate coefficient is approximately 10^6 s^{-1}, the majority of the yield is 1-penten-4-ol-3-yl, which is produced from H-shift from the primary carbon of 2-penten-4-oxy to the oxy group. Above 600 K, the majority of the yield for *syn*-DMOR3 is methyl and 2-butenal. Interestingly, the jet-stirred reactor experiment speciation data from Bugler et al.[15] show that their model underpredicts the steady state concentration of 2-butenal at 10 atm between 850 K and 1000 K.

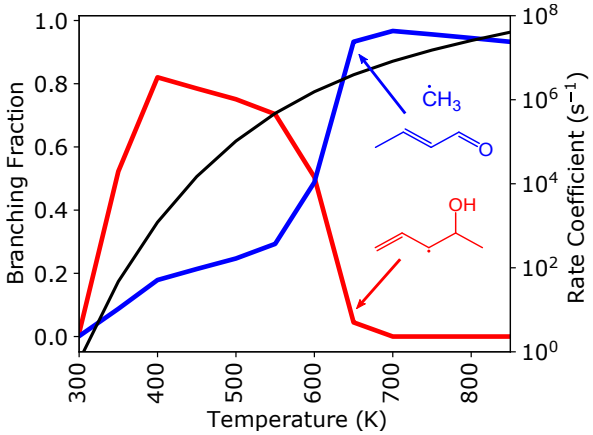

Figure 5.13: The branching fractions under at 1 atm and 20 ms for *syn*-DMOR3 are shown between 300 K and 850 K.

Figures 5.14-5.18 show the theoretical branching fractions for EOR1, EOR2, EOR3, EOR4, and EOR5. Above 700 K, acrolein and ethyl are 100% of the yield for EOR1 (Figure 5.14). Below 700 K, the major product is 1-pentanal-3-yl. Acrolein and ethyl are the main products for EOR2 above 700 K (Figure 5.15). There is also a small but significant branching fraction for 1-butyl and carbon monoxide which has a maximum of 16% at 750 K. Below 700 K, the major product is pent-3-en-1-ol-2-yl.The majority of the branching fracton for EOR3 above 500 K is butanal-1-yl and ethylene (Figure 5.16). Below 450 K, the majority of the branching fraction for EOR3 is the ring opening product, 3-pentanon-1-yl. Between 400 K and 700 K, there is a substantial branching fraction for the resonance stabilized radical 3-pentanone-2-yl, with a maximum of 50% at 500 K. The majority of the yield for EOR4 across the entire temperature range is 1-buten-3-yl and formaldehyde (Figure 5.17). 2-methylvinoxy radical and ethylene are minor products of EOR4 decomposition with a maximum branching fraction of 10% at 850 K. Below 700 K, the main product of EOR5 decomposition is 1-pentanon-3-yl, and above 700 K, the main product is acrolein and methyl (Figure 5.18). Between 400 K and 750 K, pent-3-en-1-ol-yl is

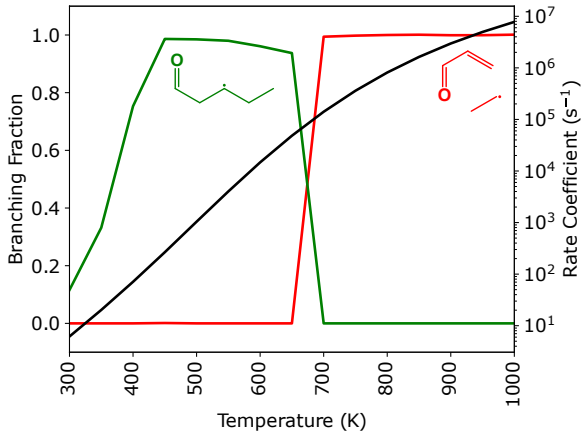

Figure 5.14: The branching fractions for the secondary 2-ethyloxetanyl radical EOR1, are given at 20 ms and 1 atm from 300 K to 1000 K by 50 K increments. In black is the total rate coefficient for EOR1 $\longrightarrow$ products on a logarithmic scale.

a minor product with a maximum branching fraction of 7% at 650 K.

There are several pathways from 2-ethyloxetanyl radicals to acrolein and ethyl. The jet-stirred reactor experiment speciation data from Bugler et al.[15] shows that the model from the same work underpredicts the steady state concentration of acrolein at 1 atm between 600 K and 700 K by approximately half. The absence of acrolein-yielding pathways from 2-ethyloxetanyl radicals may contribute to this discrepancy. However, in the same experiments, the concentration of acrolein is overpredicted by a factor of 5 above 700 K, so there are likely other sources of error in the model.

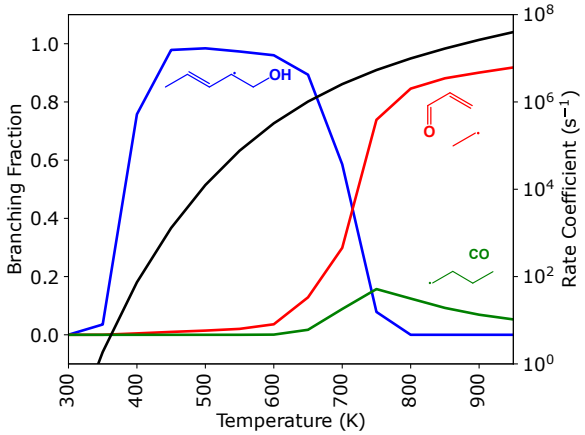

Figure 5.15: The branching fractions for the secondary 2-ethyloxetanyl radical, EOR2, are given at 20 ms and 1 atm from 300 K to 1000 K by 50 K increments. In black is the total rate coefficient for EOR2 $\longrightarrow$ products on a logarithmic scale.

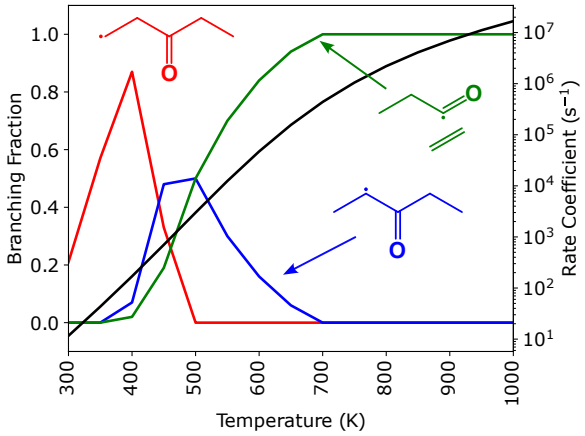

Figure 5.16: The branching fractions for the tertiary 2-ethyloxetanyl radical, EOR3, are given at 20 ms and 1 atm from 300 K to 1000 K by 50 K increments. In black is the total rate coefficient for EOR3 $\longrightarrow$ products on a logarithmic scale.

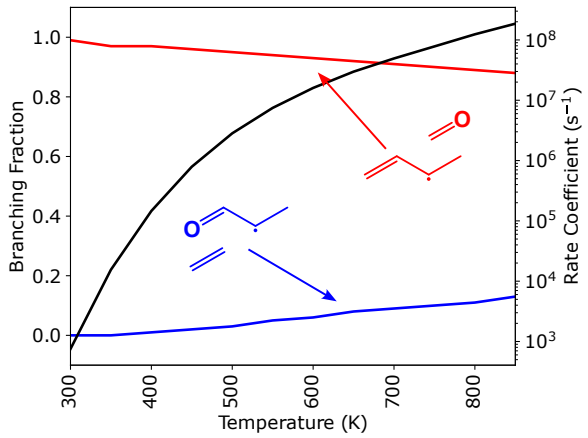

Figure 5.17: The branching fractions for the secondary radical, EOR4, are given at 20 ms, and 1 atm from 300 K to 850 K by 50 K increments. In black is the total rate coefficient for EOR4 $\longrightarrow$ products on a logarithmic scale.

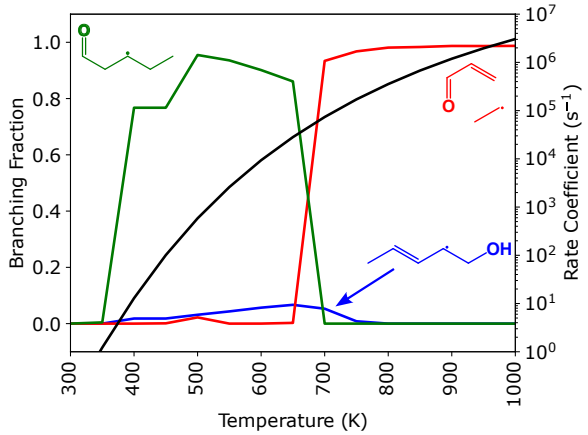

Figure 5.18: The branching fractions for the primary radical, EOR5, are given at 20 ms and 1 atm from 300 K to 850 K by 50 K increments. In black is the total rate coefficient for EOR5 $\longrightarrow$ products on a logarithmic scale.

Chapter 6

Alkyl-Substituted Oxetane Peroxy Radical Decomposition

Based on the findings from Doner et al.[20] and Christianson et al.,[21] alkyl-substituted cyclic ether radicals do react with O_2 and follow ROO- and QOOH-mediated pathways. This chapter details the investigation of the decomposition of peroxy radicals resulting from H-abstraction from and O_2-addition to 2,4-dimethyloxetane and 2-ethyloxetane. The results for 2,4-dimethyloxetane peroxy radicals in this chapter are detailed by Doner et al.[16] The first section summarizes each of the 14 potential energy surfaces constructed. The second section compares the theoretical rate coefficients calculated from 300 K to 1000 K and 0.01 atm to 100 atm for each reaction discovered. Finally, the third section provides theoretical branching fractions under conditions relevant to low-temperature combustion experiments, namely jet-stirred reactor (JSR) experiments. These branching fractions demonstrate the dramatic effect of the stereochemistry of the initial peroxy radical and can serve as targets for experimentalists to replicate.

6.1 Potential Energy Surfaces

In the following subsections, the potential energy surfaces constructed at the CCSD(T)-F12/cc-pVDZ-F12 level of theory for EO and DMO peroxy radicals are summarized by compar-

ing barrier heights for each ROO and QOOH species. Notable pathways following ring opening of QOOH are also provided and discussed. Due to a change in computational resources available, ORCA[61] instead of Molpro[62] was used to calculate stationary point energies for *anti*- and *syn*-EOROO1, *anti*- and *syn*-EOROO2, and EOROO5. Note that relative energies were never calculated from the difference of values calculated with different software.

6.1.1 ROO-Mediated Reactions

Figure 6.1 give the well depths and barrier heights for each peroxy radical formed from H-abstraction from and subsequent O_2-addition to 2-ethyloxetane (EO) and 2,4-dimethyloxetane (DMO). Pathways available to ROO radicals include concerted HO_2-elimination and internal H-abstraction forming QOOH radicals. Barriers to concerted HO_2-elimination pathways are lowest for ROO radicals in which the peroxy radical is positioned on a tertiary carbon. The pathways for HO_2-elimination from each of the EOROO2 radicals were excluded due to large barrier heights, so the barrier heights provided in Figure 6.1 are at the L2=ωB97X-D/6-311++G(d,p) level of theory. In Figure 6.1, the deepest submerged pathways for HO_2-elimination are for *syn*- and *anti*-DMOROO2 and EOROO3. However, formation of a QOOH is the lowest energy pathway for each ROO radical. The lowest barriers for QOOH formation correspond to loose six- or seven-membered transition states. Figure 6.2 gives the QOOH from the lowest energy pathway for each DMO and EO peroxy radical.

6.1.2 QOOH-Mediated Reactions

Figure 6.3 summarizes the pathways available to each QOOH species formed from DMO and EO peroxy radicals. QOOH species in which the hydroperoxy group is positioned on the alkyl chain typically have shallower wells than those with the hydroperoxy group positioned on the oxtane ring. As an example, isomerization to ROO has an average barrier height of 12.3 kcal/mol for the QOOH radicals formed from , while for the QOOH radicals formed from EOROO2, this value is 14.5

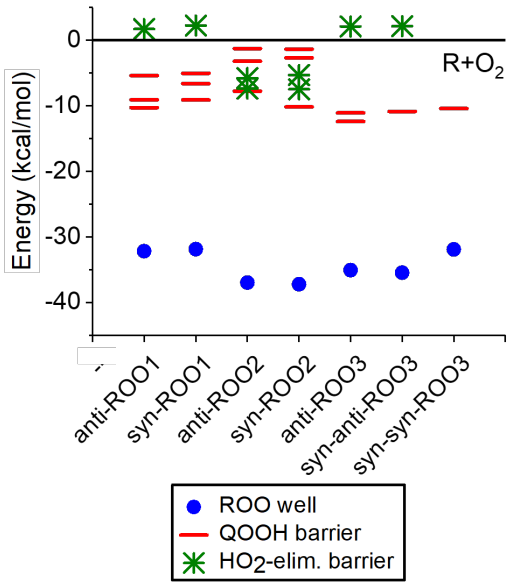

a)

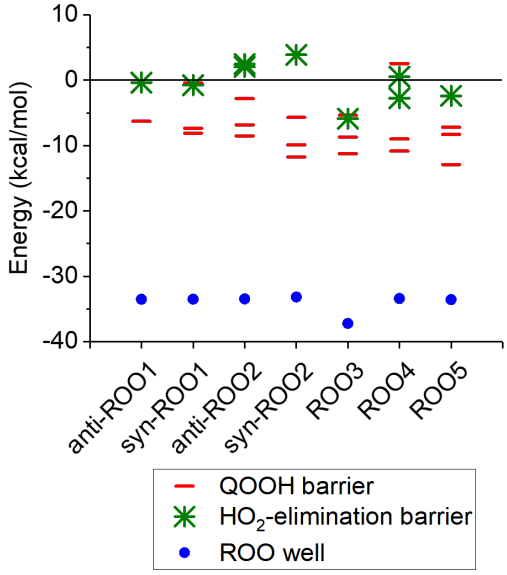

b)

Figure 6.1: The well depths for each 2,4-dimethyloxetane (a) and 2-ethyloxetane (b) peroxy radical (blue) and barrier heights for HO_2-elimination (green) and QOOH formation (red) are shown relative to R + O_2. The barrier heights for HO_2-elimination are shown at the L2=ωB97X-D/6-311++G(d,p) level of theory.

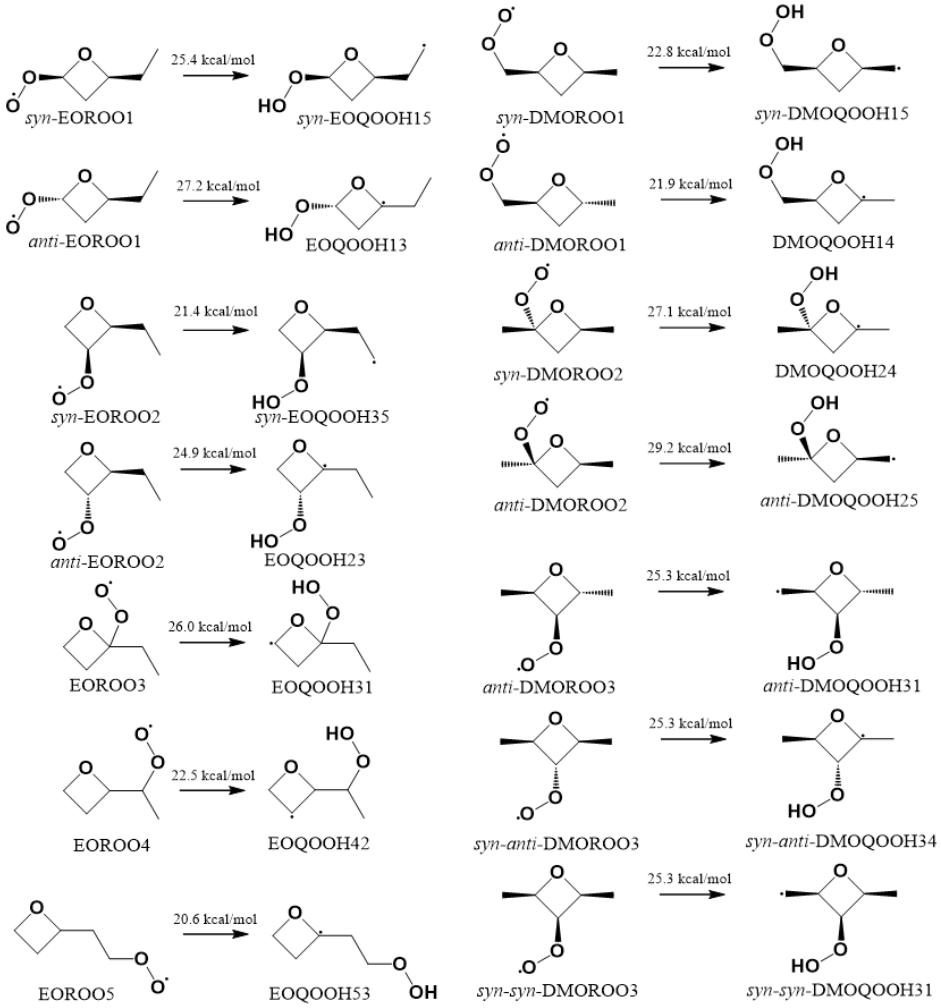

Figure 6.2: The ROO $\longrightarrow$ QOOH isomerization pathways with the lowest barrier heights are given for each peroxy radical derived from DMO and EO.

kcal/mol. Additionally, each of the QOOH radicals formed from has no lower barrier than isomerization to ROO. In constrast, QOOH radicals from EOROO2 have several pathways with smaller barriers than the reverse reaction yielding EOROO2, including HO_2-elimination, bicylic ether formation, and ring-opening.

All HO_2-elimination pathways were found for each β-QOOH. The pathway to 2-ethylideneoxetane is only included for EOQOOH43 and not EOQOOH34. This can be rationalized by the increased flexibility of the hydroperoxy group in EOQOOH43, which is positioned on the secondary carbon compared to EOQOOH34, in which the hydroperoxy group is positioned on the tertiary carbon.

Bicyclic ether formation pathways were found for each QOOH species at the L1 level. Three bicyclic ether formation pathways were not included either because the barrier height was not submerged below R + O_2 or the pathways did not account for at least 5% of the branching fraction from the QOOH well at 400 K or 1000 K at the high pressure limit. The bicyclic ethers excluded are given by Figure 6.4. The pathway forming the bicyclic ether 3-methyl-2,5-dioxabicyclo[2.1.1]hexane is only included for EOQOOH41 and not EOQOOH14. This can be attributed to a lower barrier for the competing ring-opening reaction of EOQOOH14 (11.5 kcal/mol) than for EOQOOH41 (26.2 kcal/mol). Similarly, 1-methyl-2,5-dioxabicyclo[2.1.1]-hexane is formed from DMOQOOH14 but not DMOQOOH25. The lowest barriers for competing ring-opening pathways for DMOQOOH14 and DMOQOOH25 are 26.3 kcal/mol and 13.6 kcal/mol, respectively. Each of the ring-opening pathways for QOOH species formed from isomerization of EOROO5 are not submerged below EOR + O_2. Therefore, they were not followed further than the QOOH species directly resulting from ring-opening.

Each of the QOOHs for which bicyclic ether formation was excluded can undergo ring-opening and OH-loss, producing dicarbonyls. DMOQOOH24 produces acetylacetone over a 18.9 kcal/mol barrier, and EOQOOH13 and EOQOOH31 produce 1,3-pentanedione over 19.2 kcal/mol and 19.5 kcal/mol barriers, respectively. In the mechanism for *n*-pentane from

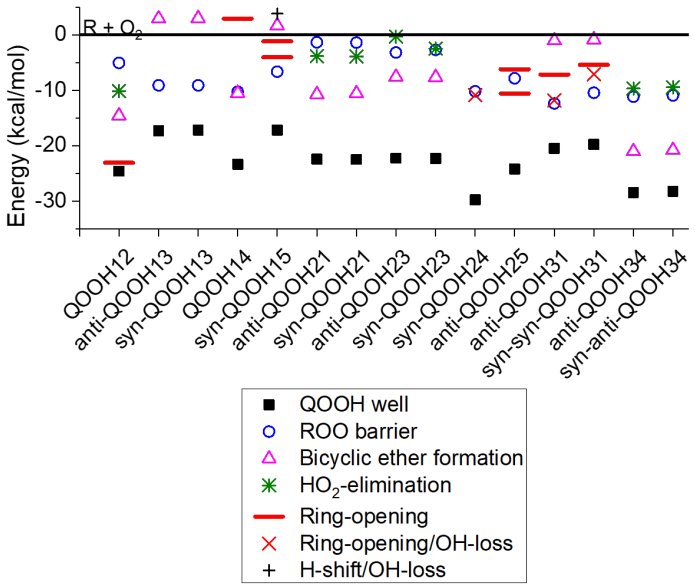

a)

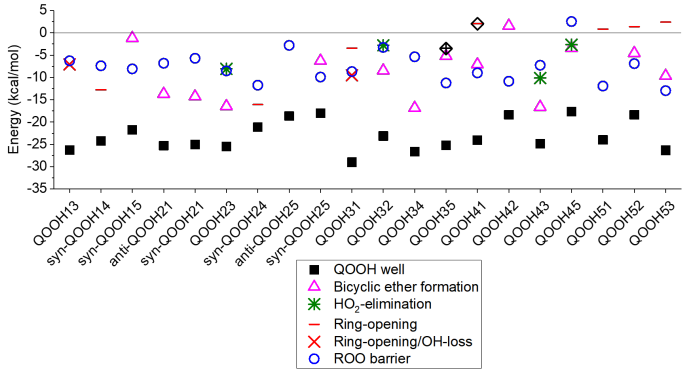

b)

Figure 6.3: The well depths for each DMO (a) and EO (b) QOOH radical (blue) and barrier heights for HO_2-elimination (green), ring opening (red), isomerization to ROO (blue), and bicyclic ether formation (magenta) are shown relative to ROO.

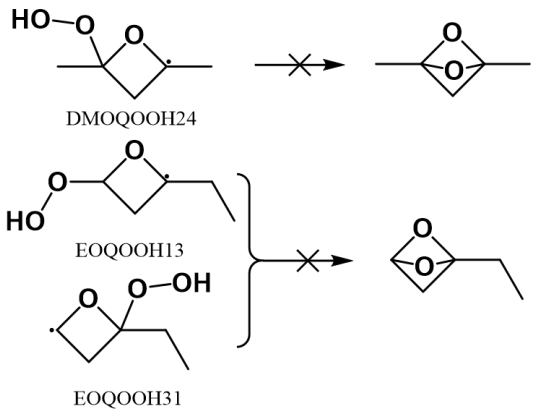

Figure 6.4: The bicyclic ethers for which pathways were excluded are shown.

Bugler et al.[15], both diones are products of KHP decomposition. Acetylacetone and 1,3-pentanedione concentrations in JSR experiments were underpredicted ratio by the model at stoichiometric equivalence and 1 atm at 600 K according to Bugler et al.[15] The results of the present work suggest that some of this concentration can be attributed to cyclic ether reactions instead of KHP decomposition alone. These discrepancies are important to correct because predicted flux to KHP can significantly impact modeled ignition delay times.[63]

QOOH diastereomers typically have similar relative barrier heights as exemplified by *syn*- and *anti*-QOOH13 from DMOROO1 and *syn*- and *anti*-QOOH21 from EOROO2 (Figure 6.3). Several QOOH radicals are unique to one diastereomer of their ROO precursor. While DMOOOOH14 is only formed from the *anti*-DMOROO1 radical, DMOQOOH15 is only formed from the *syn*-DMOROO1 radical. Similarly, while DMOQOOH24 is only formed from the *syn*-DMOROO2 radical, DMOQOOH25 is only formed from the *anti*-DMOROO2 radical. EOQOOH13 is only formed from *anti*-EOROO1, while EOQOOH14 and EOQOOH15 are only formed from *syn*-EOROO1. EOQOOH23 is only formed from *anti*-EOROO2, while EOQOOH24 is only formed from *syn*-EOROO2. For many ROO radicals, the lowest lying pathway to QOOH is also unique to one diastereomer. This enhances the effect of

stereochemistry on the kinetics of alkyl-substituted oxetane peroxy radicals.

6.1.3 Notable Pathways Following Ring-Opening

As demonstrated in the previous section, acyclic QOOH radicals are produced from several ring-opening reactions of QOOH. These species follow either β-scission reactions, H-shifts, and rearrangement pathways. Figure 6.5 shows the rearrangement of the QOOH radical resulting from ring-opening of DMOQOOH14. Similar reactions of 3-oxoalkyl radicals were studied by Scheer et al.[64] The product in Figure 6.5 could also be produced via H-abstraction from KHP species in *iso*-pentane combustion. Thus, this pathway may falsely suggest the presence of *iso*-pentane if their decomposition products were detected experimentally.

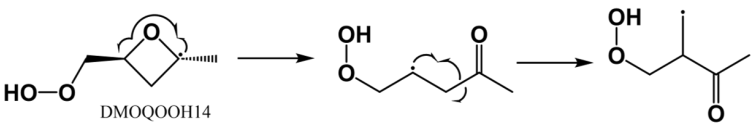

Figure 6.5: A rearrangement reaction of DMOQOOH14 occurs via a three-membered transition state producing a branched, acyclic QOOH radicals.

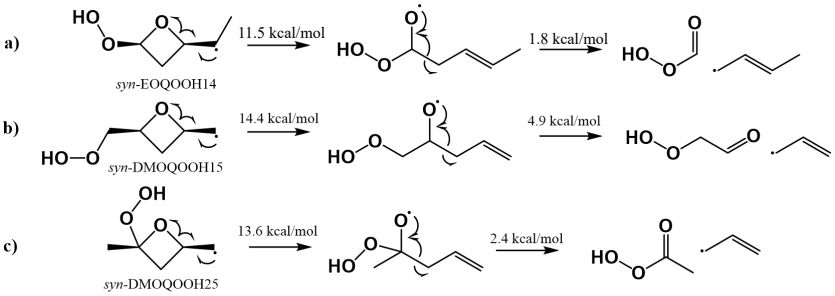

Figure 6.6: Reactions producing small ketohydroperoxides (a) performic acid, (b) 2-hydroperoxyacetaldehyde, and (c) peracetic acid, from *syn*-QOOH14, *syn*-DMOQOOH15, and *syn*-DMOQOOH25, respectively, are shown with barrier heights.

Hydroperoxyalkoxy radicals, which are produced from ring-opening of QOOH in which the radical carbon is separated by one carbon from the ether group, primarily undergo β-scission. In some cases, this yields a hydrocarbon radical

and a small ketohydroperoxide. The KHP species formed from hydroperoxyalkoxy radicals include performic acid, peracetic acid, and 2-hydroperoxyacetaldehyde. Because the L3 energy for the transition state forming performic acid and 2-buten-1-yl was submerged below the reactant by 8 kcal/mol, the relative energy calculated at the L2 energy was substituted. Future work is needed to better characterize this transition state with a higher level theory for the geometry optimization. Each of the reactions yielding small, closed-shell KHP species is shown in Figure 6.6.

6.2 Theoretical Rate Coefficients

The highest several rate coefficients for each DMO and EO peroxy radical at 1 atm is plotted vs. temperature from 300 K to 1000 K in Figure 6.7 and Figure 6.8, respectively.

The DMOROO2 radicals are the only species with rate coefficients for HO_2-elimination which are higher than the rate coefficients for formation of any QOOH above 500 K. This can be attributed to the relatively lower barriers to HO_2-elimination discussed in the previous section. However, the rate coefficient for HO_2-elimination from EOROO3, another tertiary peroxy radical with, is lower than the rate coefficient for formation of EOQOOH35 across the entire temperature range.

Well skipping rate coefficients overtake stepwise rate coefficients for QOOH formation as temperature increases. As pressure increases, the temperature above which well skipping reactions are faster than stepwise reactions increases.[36] In several cases, the rate coefficient values for QOOH formation vanish at high temperatures. It is notable that the rate coefficient for formation of EOQOOH42 vanishes above 400 K despite there being no well-skipping rate coefficient near its magnitude at higher temperatures. This may be caused by the shallow QOOH well.

6.3 Theoretical Branching Fractions

Theoretical branching fractions were computed from the master equation solutions at 1 atm and two temperatures, 650 K

and 825 K. The temperatures selected correspond to observed peaks in the steady-state concentration of cyclic ethers in JSR experiments on low-temperature combustion of *n*-pentane. Figure 6.9 and Figure 6.10 summarize the branching fractions for each peroxy radical under each set of conditions by categorizing products by pathway type. The peroxy radicals almost exclusively undergo combinations of HO_2-elimination, bicyclic ether formation, and ring-opening, depending heavily on the stereochemistry of the initial ROO radical where applicable.

The majority of the yield from *anti*-DMOROO1 is bicyclic ethers at both temperatures. The *syn* diastereomer of DMOROO1 yields over 85% ring-opening products at both temperatures. At 650 K, *syn*-DMOROO1 ring-opening pathways primarily produce OH radicals, but at 825 K there is an increase in the branching fraction for other ring-opening radical products, such as allyl. The DMOROO2 radicals are the only DMO peroxy radicals which have a substantial branching fraction corresponding to HO_2-elimination from either ROO or QOOH radicals. This is easily rationalized by the low barrier heights for HO_2-elimination shown in Figure 6.1a. Similarly, EOROO3, which also has the peroxy group positioned on the tertiary carbon, has a significant branching fraction for HO_2-elimination. The DMOROO3 radicals undergo a combination of bicyclic ether formation and ring-opening reactions. The *syn*-*syn*-DMOROO3 radical branching fractions are dominated by ring-opening products, while the *syn*-*anti*-DMOROO3 radical yields entirely bicyclic ethers, and *anti*-DMOROO3 has significant branching fractions for bicyclic ether formation and ring-opening. This pattern is dictated by which QOOH pathways are available to each diastereomer. The *syn*-*syn*-DMOROO3 radical has one QOOH-mediated pathway forming DMOQOOH31. DMOQOOH13 primarily undergoes simultaneous ring-opening and OH-loss, yielding 2-(vinyloxy)propanal. The *syn*-*anti*-DMOROO3 radical also has only one QOOH-mediated pathway which forms DMOQOOH34. DMOQOOH34 exclusively forms the bicyclic ether, 1,3-dimethyl-2,5-dioxabicyclo [2.1.0]pentane. In contrast, *anti*-DMOROO3 has QOOH-mediated pathways form-

ing both DMOQOOH31 and DMOQOOH34, resulting in a mixture of product types.

The *anti* diastereomer of EOROO1 yields mostly ring-opening products, specificially, 1,3-pentanedione and OH which is produced from QOOH13 in one step. The remaining yield is composed of HO_2-elimination products. The majority of the branching fractions calculated for *syn*-EOROO1 was also comprised of ring opening products. $40-60\%$ of the branching fraction for *syn*-EOROO1 under the selected conditions was the small KHP performic acid. *anti*-EOROO2 produces exclusively bicyclic ethers. 3-ethyl-2,5-dioxabicyclo-[2.1.0]pentane, formed from EOQOOH21 decomposition, is the major product making up over 80% of the yield at both temperatures shown. 1-ethyl-2,5-dioxabicyclo[2.1.0]pentane, formed via decomposition of EOQOOH23, constitutes the remainder of the yield for *anti*-EOROO2. EOROO3 is the only peroxy radical which has a significant branching fraction for HO_2-elimination. There is a minor product from β-scission of EOQOOH35, yielding oxetan-2-one, ethylene, and OH contributing 8-11% of the yield between 650 K and 825 K. EOROO4 mostly produces bicyclic ethers, including 3-methyl-2,5-dioxabicyclo[2.2.0]hexane, 3-methyl-2,5-dioxabicyclo[2.1.1] hexane, 2-methyl-1,4-dioxa-spiro[2.3]hexane, and 2-(oxiran-2-yl)oxetane. At both 650 K and 825 K, EOROO5 mostly decomposes to form bicyclic ethers, including 2,6-dioxabicyclo[3.2.0] heptane and 1,5-di-oxaspiro[3.3]heptane. However, there is a minor β-scission pathway forming 2-methyleneoxetane, formaldehyde and OH from EOQOOH53 which makes up 9-12% of the yield. The exclusion of non-submerged ring-opening pathways from the EOROO5 potential energy surface appears to have been inconsequential as the total ring-opened QOOH yield at 825 K is approximately 1%.

In summary, the pathways which alkyl-substituted peroxy radicals follow depend on which QOOH species can be formed. This is heavily impacted by the initial radical's stereochemistry. The carbon of the QOOH on which the radical is centered determines how favorable ring-opening is. Although ring-opening of QOOH species with the radical centered on a carbon adjacent to the ether group are exothermic, they have

higher barriers to ring opening than QOOH species with the radical center located on the 3-position of the oxetane ring or on an alkyl substituent. Favorable ring opening pathways can shift flux away from conventional QOOH-mediated pathways such as bicyclic ether formation. Many of the significant ring opening pathways found in the present work form an important link between cyclic ethers and ketohydroperoxides, which has not been investigated previously. This class of reactions likely contributes the discrepancies between modeled and experimentally measured species profiles in combustion experiments.[15]

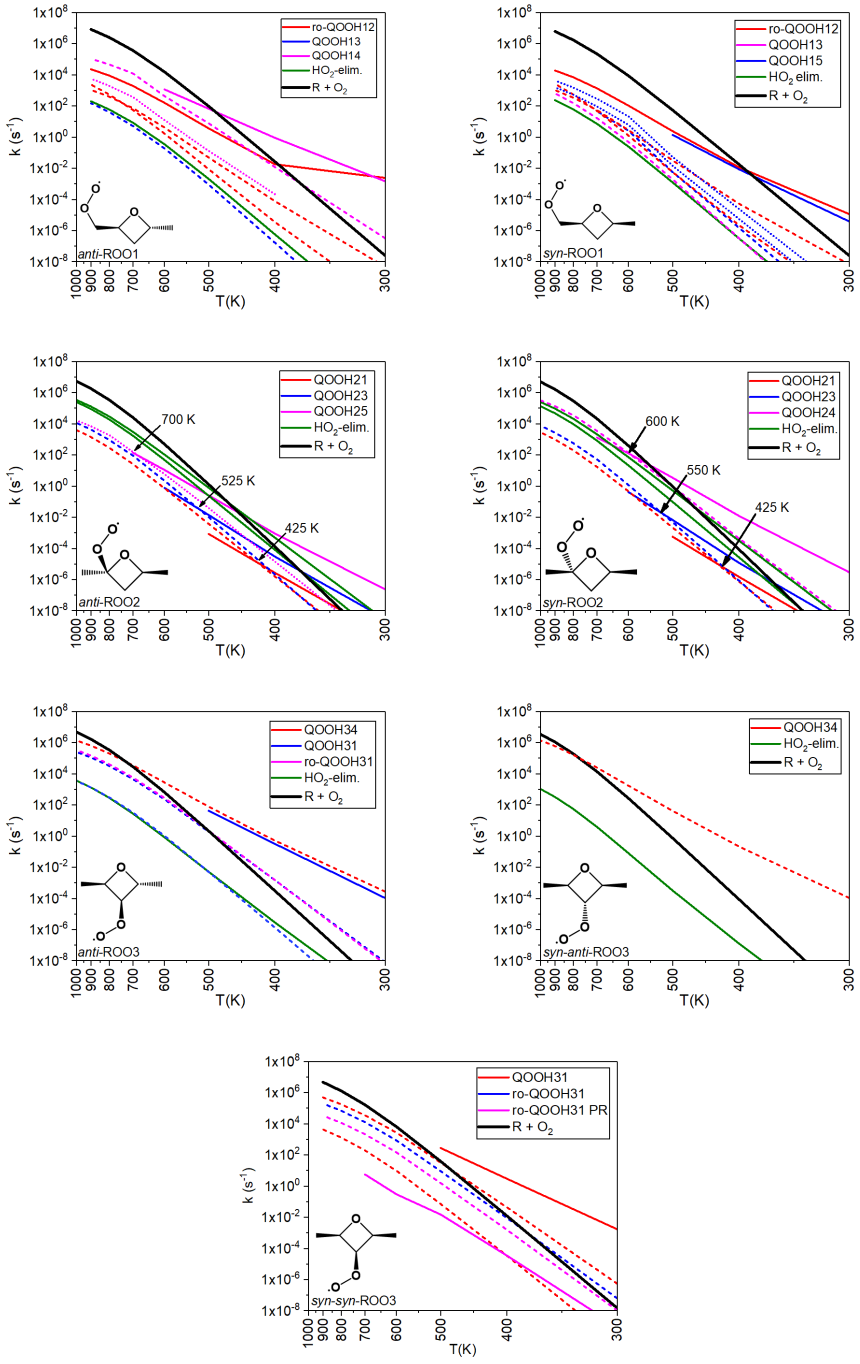

Figure 6.7: The rate coefficients for each DMO peroxy radical at 1 atm are given from 300 K to 1000 K. Solid red, blue, and magenta lines denote the rate coefficient for isomerization to QOOH. Dashed lines denote well-skipping rate coefficients which skip over the QOOH of the same color. The prefix "ro" denotes ring-opening pathways.

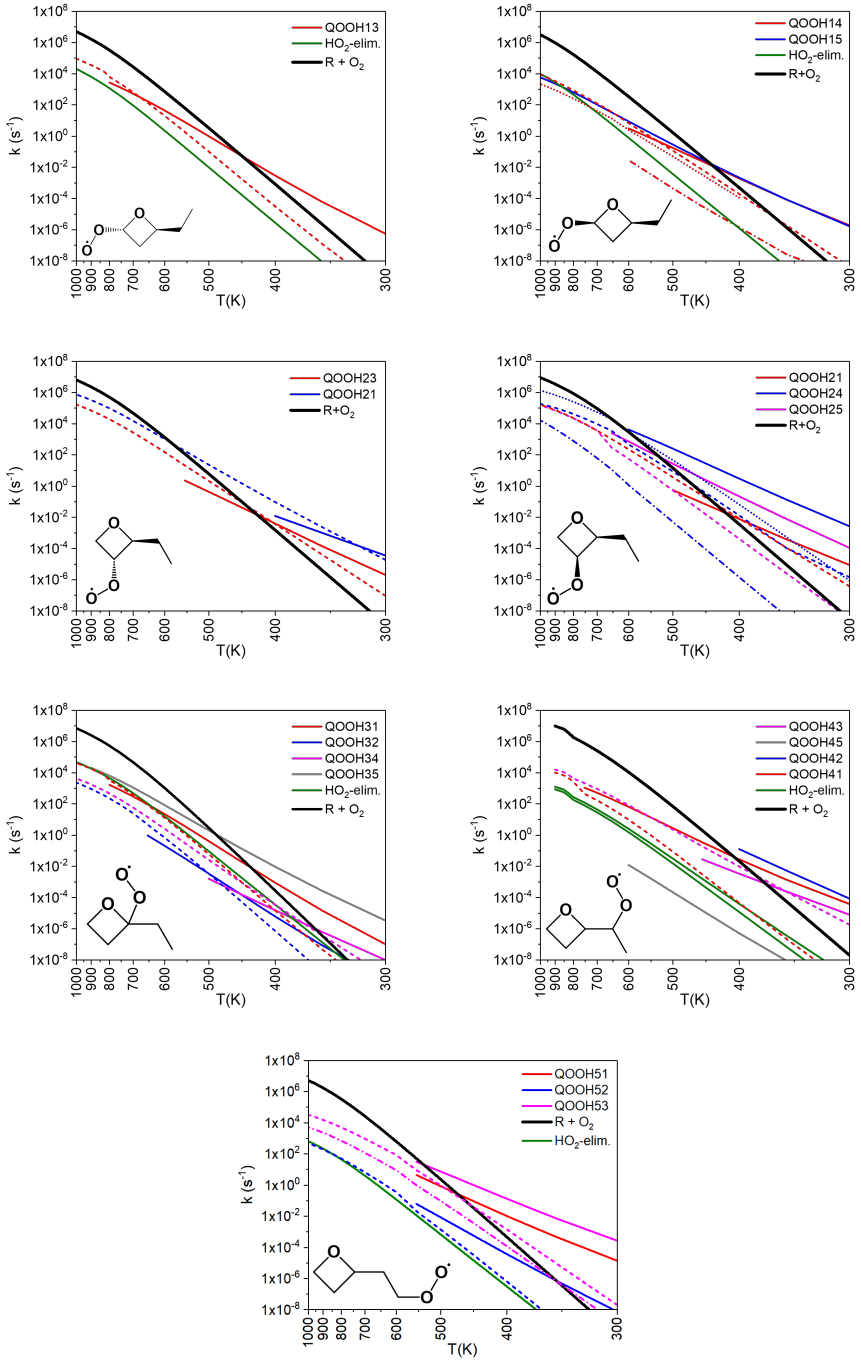

Figure 6.8: The rate coefficients for each EO peroxy radical at 1 atm are given from 300 K to 1000 K. Solid red, blue, and magenta lines denote the rate coefficient for isomerization to QOOH. Dashed lines denote well-skipping rate coefficients which skip over the QOOH of the same color.

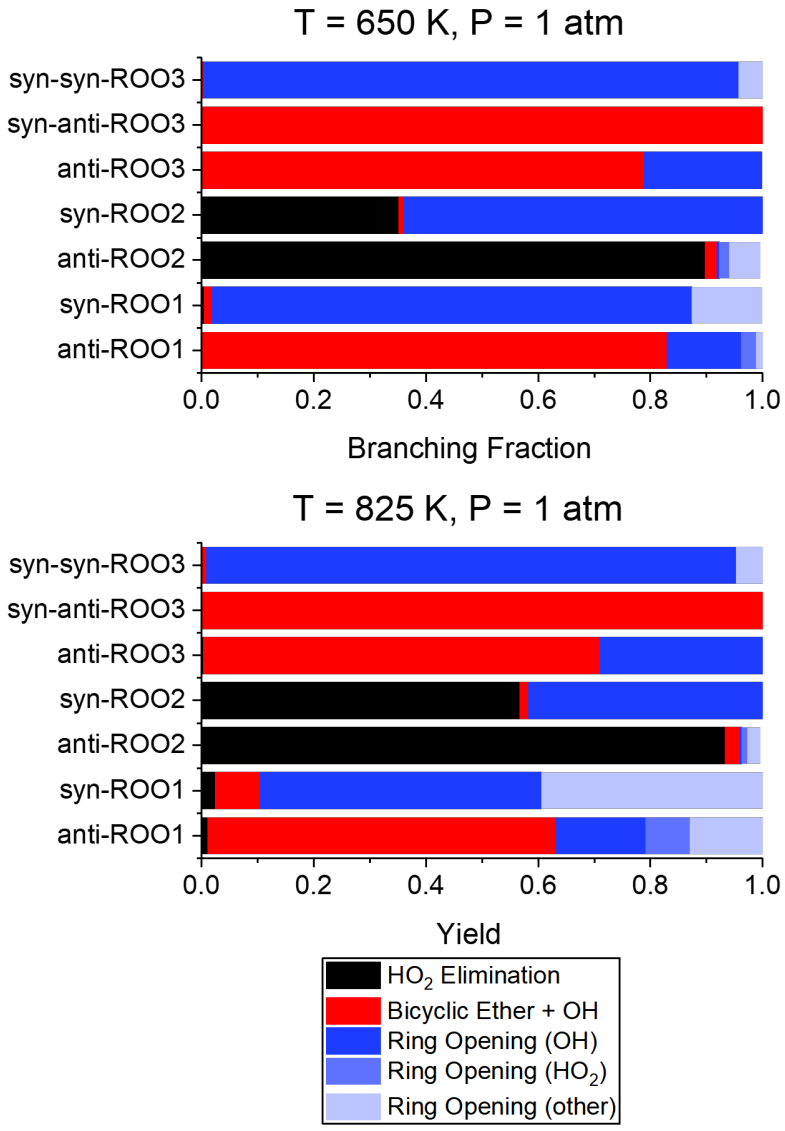

Figure 6.9: Theoretical branching fractions are given for each DMO peroxy radical at 1 atm at 650 K (top) and 825 K (bottom). Red denotes bicyclic ether products, black denotes HO_2-elimination products, and blue denotes ring-opening products. The ring-opening branching fractions are subdivided by what radical is produced, OH, HO_2, or other.

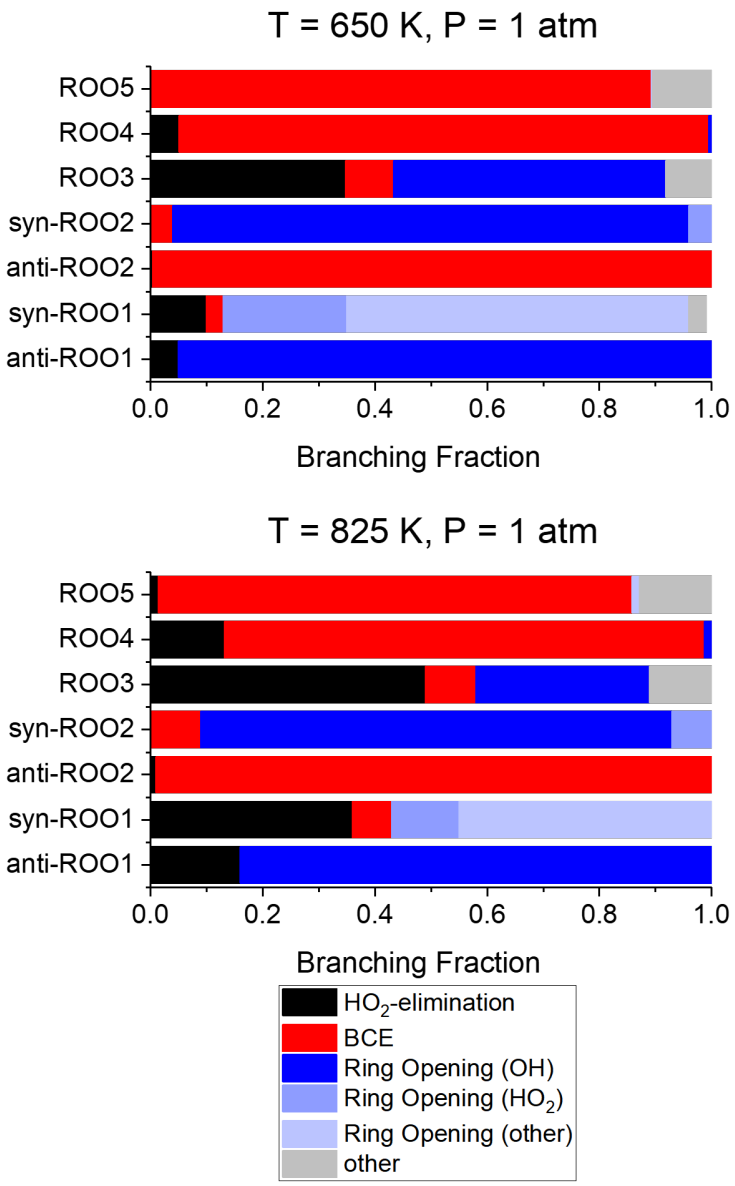

Figure 6.10: Theoretical branching fractions are given for each EO peroxy radical at 1 atm at 650 K (top) and 825 K (bottom). Red denotes bicyclic ether products, black denotes HO_2-elimination products, and blue denotes ring-opening products. The ring-opening branching fractions are subdivided by what radical is produced, OH, HO_2, or other. In gray are products arise from other pathways.

Chapter 7

Vacuum Ultraviolet (VUV) Absorption Spectroscopy

Historically, quantitative VUV absorption cross-sections have been published for a variety of functionalized hydrocarbons.[23] However, measurements have been limited by the reliance on synchrotron radiation and vacuum conditions to prevent absorption from contaminating atmospheric gases (N_2, O_2, CO_2, H_2O, etc.). The method described in the Computational Methods chapter has facilitated the measurement of dozens more combustion-relevant functionalized hydrocarbon intermediates.[46,48,47] The following sections include (1) literature comparisons of known VUV absorption cross-sections and (2) VUV absorption cross-sections for species measured for the first time.

7.1 Literature Comparisons

The sources of discrepancies between VUV absorption cross-sections from the present work and previous work include differences in conditions and detection. Most previous measurements have been conducted at ambient temperature and low pressure (< 10 Torr), while the measurements from the present work are obtained at 800 Torr to prevent contamination from atmospheric gases and 50°C to prevent condensation in the flow cell. These conditions make the spectrum

prone to peak-broadening.[65] Additionally, some of the first measurements of VUV absorption cross-sections, conducted as early as the 1950s,[66,67] used photographic plates to quantify the absorption cross-section which are prone to error.

Figure 7.1 provides literature comparisons of VUV absorption cross-sections measured by Doner et al.[24] for two constitutional isomers, dimethyl ether and ethanol. Dimethyl ether

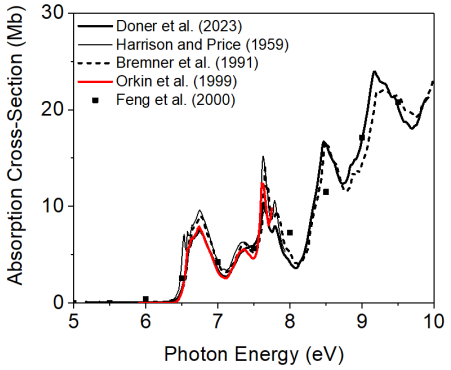

a)

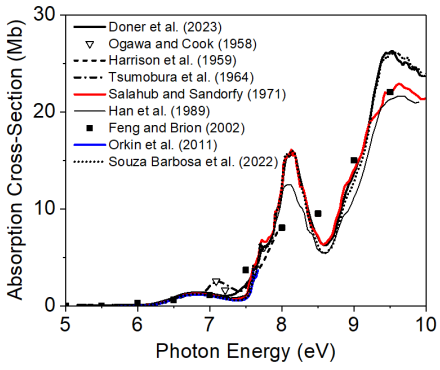

b)

Figure 7.1: VUV absorption cross-sections of (a) dimethyl ether measured by Doner et al.[24] are in excellent agreement with measurements from several previous studies.[66,68,69,70] Likewise, VUV absorption cross-sections of (b) ethanol measured by Doner et al.[24] are in good agreement with previous measurements,[66,67,71,72,73,74,75,76] especially the most recent by Souza Barbosa et al.[76]

has three large sharp peaks centered at 6.8 eV, 7.7 eV, and 8.5 eV. Bremner et al.[68] has assigned these as the 3s, 3p, 3d Rydberg series, respectively. Ethanol has a large peak centered at 8.1 eV corresponds to the 3pπ Rydberg transition.[76] The

smaller, broader peak centered at 6.8 eV represents the 3s Rydberg transition and is prototypical of simple alcohols.[23,76]

7.2 New Reference Measurements

In the present work, VUV absorption cross-sections for many multi-functionalized hydrocarbons were measured for the first time. Figure 7.2 gives four examples of VUV absorption cross-sections published for the first time by Doner et al.[46,48,24] Vinyl acetate is a ring-opening product of 2,3-dimethyloxirane + O_2 which was detected by Doner et al.[20] using multiplexed photoionization mass spectrometry (MPIMS). Vinyl acetate has a large broad peak centered at 6.6 eV due to its conjugated π-system spanning 5 atoms. 1,4-dioxene has the same chemical formula as vinyl acetate, $C_4H_6O_2$, and a conjugated π-system spanning 4 atoms. Consequently 1,4-dioxene also absorbs in the low energy region (< 6 eV). However, the broad peak centered at 6.6 eV in the 1,4-dioxene cross-section is smaller and shows vibrational structure.

3-methyl-2-buten-1-ol and 3-methyl-3-buten-1-ol are constitutional isomers which differ only in the position of the π-bond. They are potential products in *iso*-pentane combustion. The most obvious difference in their VUV absorption spectra is that 3-methyl-2-buten-1-ol first absorbs at 0.3 eV lower than 3-methyl-3-buten-1-ol. This is likely due to electron delocalization from the π-bond to the alcohol group for 3-methyl-2-buten-1-ol, in which the alcohol group and π-bond are only separated by one carbon. These examples demonstrate the powerful isomer-resolution of VUV absorption spectroscopy.

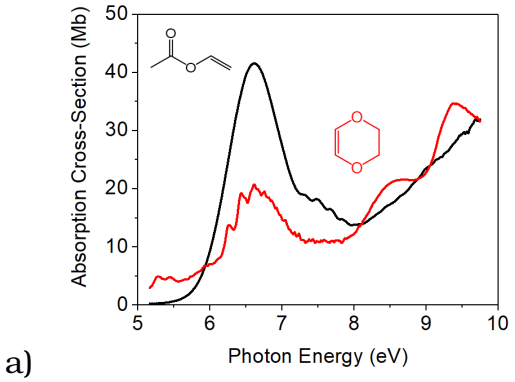

a)

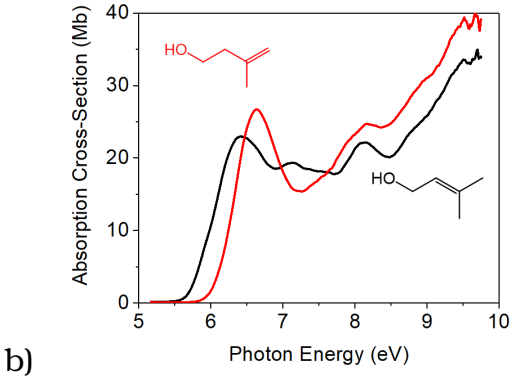

b)

Figure 7.2: The VUV absorption cross-sections for two sets of constitutional isomers, (a) vinyl acetate[48] and 1,4-dioxene[46] and (b) 3-methyl-2-buten-1-ol[24] and 3-methyl-3-buten-1-ol[24] first published by Doner et al. are shown.

Chapter 8

Classification of Vacuum Ultraviolet (VUV) Absorption Spectra

Machine learning methods were applied to a library of 102 VUV absorption cross-section reference measurements to build binary classification models that can be used to predict molecular structure features of unknown species given their absorbance spectrum. The first section of this chapter analyzes the results of exploratory Principal Components Analysis (PCA), which provides information about the variance in the dataset. The second section assesses the accuracy and reliability of the models built with various pre-processing methods, PLS-DA, and decision trees classifiers. Finally the third section contains analysis of the results of "binning analysis" in which the models were applied to only a fraction of the photon energy range to determine which slices of the absorption spectra were critical to correct classification. The results indicate that different molecular structure classifications benefit from widely different pre-processing methods and photon energy ranges.

8.1 Principal Components Analysis

The natural clusters in the dataset revealed by PCA were saturated species, unsaturated but not conjugated species, and conjugated species. The clustering is demonstrated in Figure 8.1, where Figure 8.1a shows the separation between non-conjugated alkenes in red and the remaining species in black. Non-conjugated alkene species, such as 1,4-cyclohexadiene, are clustered around positive PC1 scores, high PC2 scores (> 15), and negative PC3 values. Saturated species, such as *n*-butane, are clustered around negative PC1 scores and low PC2 scores. Conjugated species, such as benzene, are clustered around positive PC1 and PC3 scores. PCA alone could be reasonably applied for classification into these groups. On the contrary, Figure 8.1b shows the lack of separation between homocyclic species in red and the remaining species in black. Homocyclic species include saturated species such as cyclohexane, non-conjugated alkenes such as cyclohexene, and conjugated species, such as benzene. Therefore, they are not clustered to any specific area of principal component space.

The coefficients that transform the original variables to the principal component, or loadings, provide information on contributions of the initial dataset variables to that particular principal component. In chemometrics, loadings often resemble certain spectral features that account for the most variance in the dataset. Figure 8.2 gives the loadings for the first three principal components, PC1, PC2, and PC3, which explain 28.8%, 13.8%, and 12.5% of the variance in the dataset, respectively.

The PC1 loadings have a broad peak at 6.8 eV with positive values at low photon energies and negative values at high photon energies. The PC2 loadings are positive across the spectrum and increase as photon energy increases. Similarly, alkanes absorb at high photon energies, with little to no absorbance below 8 eV. The PC3 loadings are positive at low and high photon energies and negative in the mid-photon energy region (6.5-8.5 eV). Peaks in the low photon energy region (<6 eV) usually correspond to transitions from conjugated π-

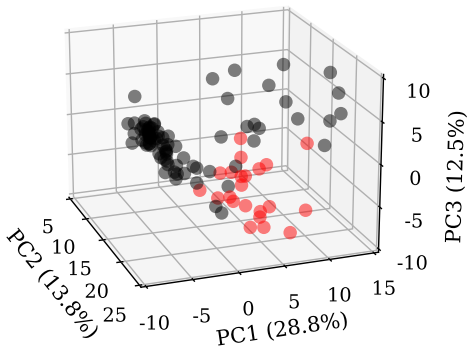

a)

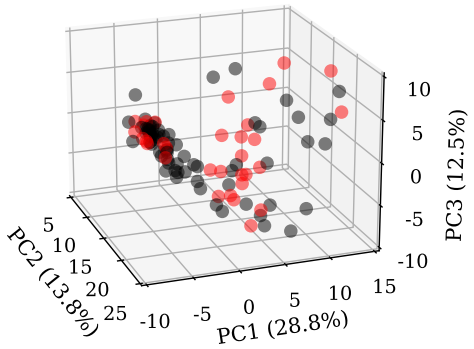

b)

Figure 8.1: The PCA decomposition for the VUV absorption spectra dataset is given with (a) the non-conjugated alkenes in red and (b) the homocyclic species highlighted in red. The natural clustering in the dataset easily separates the non-conjugated alkenes, but not the homocyclic species.[24]

systems. Therefore, conjugated species typically have positive PC3 scores as discussed previously.

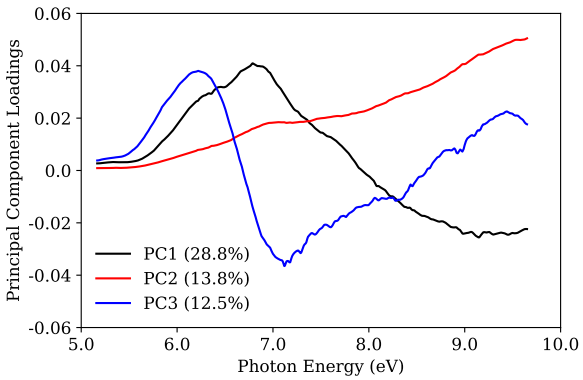

Figure 8.2: The loadings for each of the first three principal components, which provide the contribution of each wavelength to a given principal component, are plotted against photon energy (eV).

8.2 Classification Results

The highest accuracy achieved by each model-type for each classification is given by Figure 8.3. Details of each of these models are given by Table 8.1. Each of the pre-processing methods and decision trees models improved accuracy compared to PLS-DA alone. The accuracy of PLS-DA with additional pre-processing was, in general, comparable to the accuracy of the decision trees methods. Neither the random forest classifier, nor the extra trees classifier had a significant advantage over the other.

For alkanes, the PLS-DA classifier with function transformation pre-processing gave the highest accuracy at 99%. For conjugation with oxygen, the PLS-DA classifier with functional transformations, and stacking gave the highest accuracy at 87.3%. For non-conjugated alkenes, the the PLS-DA classifier with function transformations and stacking gave the highest accuracy at 94.1%. For oxygen-containing species, the PLS-DA classifier with function transformations gave the highest accuracy at 92.2%. For homocyclic species, the PLS-DA classifier with function transformations gave the highest

Table 8.1: The pre-processing and classification methods are given for the most accurate model for each molecular structure classification and model-type combination.

Classification	Function Transformation + PLS-DA	Stacking + PLS-DA	Decision Trees
alkane	$y = \ln(x)$ $y = \frac{1}{\sqrt{2\pi(x+1)^3}} e^{-\frac{-x^2}{2(x+1)}}$	conjugation, $y = \ln(\frac{1}{1-\sqrt{x}})$	RandomForestClassifier, $y = \ln(x)$, $y = \frac{1}{\sqrt{2\pi(x+1)^3}} e^{-\frac{-x^2}{2(x+1)}}$
non-conjugated alkene	$y = \sqrt{x}$, $y = (1 - e^{-x})^2$	cyclic, $y = \sqrt{x}$, $y = (1 - e^{-x})^2$	ExtraTreesClassifier, $y = \frac{1}{\sqrt{2\pi x^3}} e^{-\frac{x^2}{2x}}$, $y = \frac{1}{\pi x} + 1$
conjugation with oxygen	$y = \frac{1}{\pi x} + 1$	ether, $y = \ln(x)$, $y = \frac{1}{\sqrt{2\pi(x+1)^3}} e^{-\frac{-x^2}{2(x+1}}$	RandomForestClassifier, oxygen stacking, $y = \ln(x)$, $y = e^{-x^2}$
oxygen-containing	$y = \ln(x)$, $y = e^{-x^2}$	non-conjugated alkene,$y = \ln(x)$ $y = (1 - e^{-x})^2$	ExtraTreesClassifier, oxygen stacking, $y = \ln(x)$, $y = e^{-x^2}$
homocyclic	$y = \ln(x)$, $y = (1 - e^{-x})^2$	cycloalkane, $y = \frac{1}{\pi x} + 1$	RandomForestClassifier

accuracy at 82.4%. Although the decision trees models did not give the best accuracy for any molecular structure classification, the accuracy of the decision trees classifiers for the alkane species, non-conjugated alkene species, and homocyclic species, was only 1-2% less than the highest accuracy.

In addition to accuracy, recall and precision were used as metrics for the classification models. The recall of the most accurate classification model for each molecular structure classification and model-type combination is given by Figure 8.4a. Recall refers to the portion of true positives or negatives which are predicted as positive or negative, respectively. It is favorable to maximize the recall of both positive and negative samples. For example, the PLS-DA model without pre-processing has 100% recall of the negative species, meaning that 100% of the negative, non-alkane samples were classified as such. The same model has 0% recall of positive samples, meaning that 0% of the positive, alkane samples were predicted as such. Therefore, even though the PLS-DA model is 94% accurate for alkanes, there is a 0% chance that

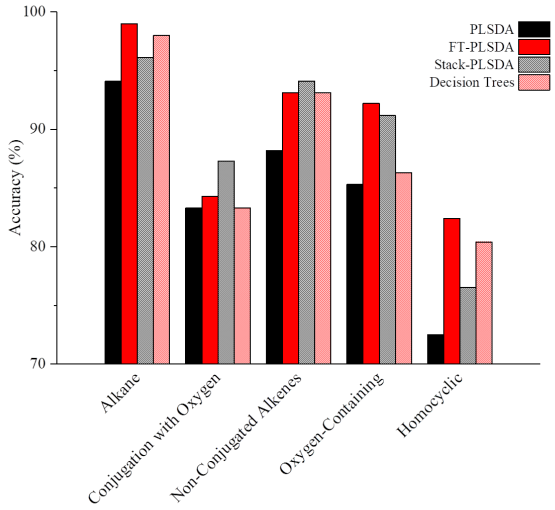

Figure 8.3: The best accuracy achieved for four model-types is given for each of the five classifications, alkanes, conjugated with oxygen, non-conjugated alkenes, oxygen-containing, and homocyclic species.

it will predict that an unknown alkane spectrum came from an alkane species.

The precision refers to the portion of the predicted positive or negative samples which are actually positive or negative, respectively. Like recall, it is favorable to maximize precision for both positive and negative predicted sample. For example, the decision trees model for classification of oxygen containing species has 89% precision for samples predicted positive, meaning that 89% of the samples predicted to contain oxygen by this model are actually do contain oxygen. The same model has only 71% precision for samples predicted negative, meaning that 71% of the samples which are predicted to be non-oxygen-containing actually do not contain oxygen.

8.3 Binning Analysis

The accuracy of the four model-types on five sections of the photon energy range are given for non-conjugated alkenes and

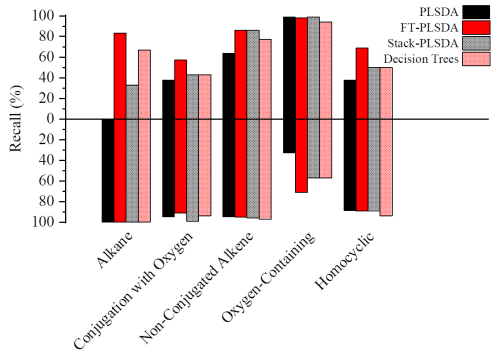

a)

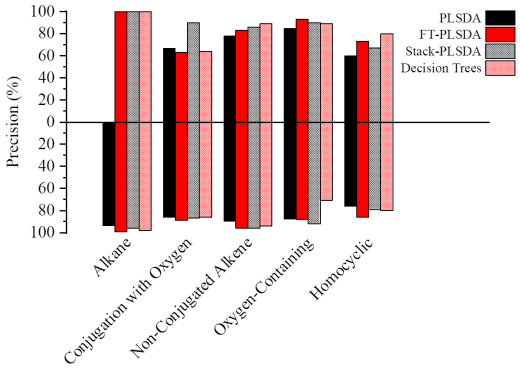

b)

Figure 8.4: The recall is given for four model-types for each of the five binary classifications is given by (a). In the negative direction is the percent of negative samples that are predicted negative. In the positive direction is the percent of positive samples that are predicted positive. The precision is given for the same four model-types for each of the five binary classifications is given by (b). In the negative direction is the percent of predicted negatives that are actually negative for the classification. In the positive direction is the percent of predicted positives that are actually positive.

conjugation with oxygen in Figure 8.5. The photon energy bin for which the best accuracy occurs depends heavily on the binary classification performed. While the best photon energy

bin could be selected to reduce computational time, none of the models were more accurate on a single portion of the spectrum compared to using the entire spectrum.

The best accuracy for classification of non-conjugated alkenes (Figure 8.5a) occurs in the middle photon energy range (6.35-7.16 eV) for every method except the extra trees classifier. This trend can be rationalized because 6.35-7.16 eV is the region where peaks corresponding to π-π* transitions that do not involve conjugation are found.[23] Conjugated alkenes have lower photon energy π-π* transitions, which absorb in the UV-vis photon energy range. The highest accuracy achieved with a single photon energy bin, 92%, was achieved by PLS-DA with and without function transformation pre-processing in the 6.35-7.16 eV bin.

For the conjugation with oxygen classification models (Figure 8.5b), there is no such general trend that each model follows. The accuracy of the PLS-DA model with function transformation increases with photon energy, while the accuracy of the extra trees classifier decreases with photon energy. The highest accuracy achieved with a single photon energy bin, 87% was achieved by the PLS-DA model with function transformation pre-processing in the 8.22-9.65 eV bin. The importance of the lowest photon energy bin (5.17-5.70 eV) to the extra trees classifier can be easily rationalized by the low-photon energy transitions associated with conjugated π-systems. However, it is unclear why the highest photon energy bin (8.22-9.65 eV) is important for the PLS-DA model with function transformation pre-processing.

The accuracy of the models described in this chapter could be improved by training the models on more VUV absorption spectra, incorporating data from other diagnostics like mass spectrometry, and applying other machine learning methods, such as neural networks. The disadvantage of neural networks for this application is that the classification results are more difficult to rationalize and understand than for PLS-DA.

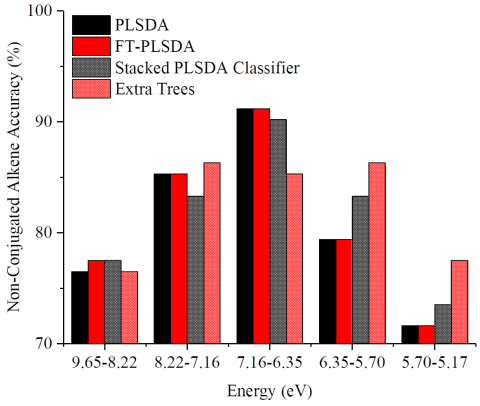

a)

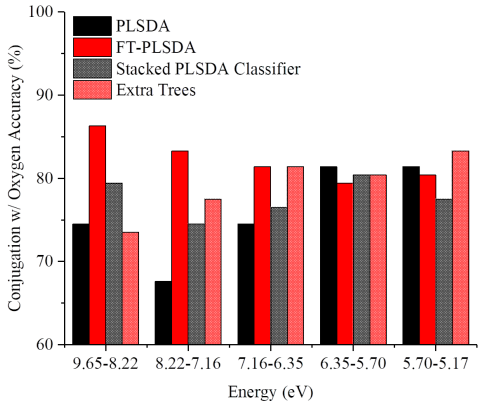

b)

Figure 8.5: The accuracy of four model-types on five subsets of the wavelength range for the non-conjugated alkene and conjugation with oxygen classifications. While the non-conjugated alkene classification models are generally more accurate in the middle energy range (6.35-7.16 eV), the conjugation with oxygen models show drastically different trends.

Chapter 9

Conclusion

The first section below summarizes the key outcomes of this dissertation. In addition to improving the accuracy of detailed chemical kinetics mechanisms for low-temperature combustion, the present work contributes to the understanding of several fundamental chemical kinetics phenomena which are the focus of ongoing research efforts in the field. The second section discusses the limitations of the methods and breadth of the present work and suggests additional studies to address them.

9.1 Key Outcomes

The joint experimental and theoretical studies by Doner et al.[20] and Christianson et al.[21] demonstrated that alkyl-substituted cyclic ether radicals produced in low-temperature combustion of alkanes, can and do react with molecular reaction in addition to pathways for unimolecular decomposition following H-abstraction (Chapter 4). Another key finding from the work by Doner et al.[20] concerning *cis*- and *trans*-2,3-dimethyloxirane, was that the stereochemistry of the initial radical impacts relative yields of peroxy radical decomposition products. Expanding this investigation to four-membered cyclic ethers, the consumption pathways for the two alkyl-substituted oxetanes produced in low-temperature combustion of *n*-pentane were characterized by the computation of theoretical master equation rate coefficients for the reactive potential energy surfaces

of each radical resulting from H-abstraction and subsequent O_2-addition.

In addition to providing theoretical rate coefficients which can replace arbitrary rate coefficients for alkyl-substituted oxetane decomposition in the mechanism for *n*-pentane from Bugler et al.[15], several new decomposition pathways which lead to products already included elsewhere in the mechanism were discovered (Chapter 5). While the prescribed decomposition products for DMO from the *n*-pentane mechanism from Bugler et al.[15] were fairly accurate, the same cannot be said for EO. Transition states corresponding to pathways to each of the products of EO decomposition in the Bugler et al.[15] were located at at least the L1 level of theory, but several were excluded due to either large barrier heights or low branching fraction. The longer alkyl chain substituent in EOR radials increases the flexibility of the molecule, facilitating a wider range of reactions, such as H-shifts, compared to DMOR radicals. This makes accurately prediction of decomposition products from "chemical intuition" substantially more difficult.

DMOR diastereomers exclusively undergo ring-opening, resulting in loss of one of two chiral centers. Because the barriers to ring-opening are nearly identical for DMOR diastereomer pairs, stereochemistry has effectively no impact on the kinetics of DMOR decomposition.

Another important outcome in Chapter 4 and Chapter 6 is the discovery of several links between alkyl-substituted cyclic ether oxidation and ketohydroperoxide kinetics. Alkyl-substitued oxetane peroxy radicals can decompose via ring-opening and β-scission, producing small, closed-shell KHP molecules, KHP radicals which are also produced from H-abstraction from closed-shell KHP, and dicarbonyls, which are commonly used as proxy species for KHP. Incorporation of all analogous pathways for each cyclic ether in alkane mechanisms (e.g. *n*-pentane) may reveal that these pathways contribute substantially to chain-branching in low-temperature combustion of alkanes.

9.2 Outlook

Jet-stirred reactor experiments at variable temperatures, pressures, and oxygen concentrations in the Rotavera Laboratory at UGA will provide additional insight into stereoisomer-dependent alkyl-substituted oxetane submechanisms. The VUV absorption spectroscopy diagnostic discussed in Chapter 7 will aid in the identification of specific intermediates predicted from the results of the present work.[46,48] Two approaches to matching unknown spectra to specific chemical structures are under development. The first is theoretical simulation of electronic absorption spectra.[77] The second is machine learning classification of VUV absorption spectra. Several reasonably accurate models for binary classification of VUV absorption spectra have been developed and discussed in Chapter 8. These models may be improved in the future by adding more reference measurements and incorporating data from other diagnostics, such as electron-impact mass spectrometry.

The present work is focused on unimolecular decomposition of radicals relevant to the oxidation of alkyl-substituted oxetanes. For this reason, H-abstraction rates and R + O_2 rates were merely estimated based on analogy to previous literature. Theoretical rate coefficients for both of these steps will further narrow the uncertainty in the overall rate of consumption of alkyl-substituted oxetanes, which are direct products of QOOH. Another source of uncertainty in the present work which needs further investigation is the computation of rate coefficients when states cannot be assumed to follow a Boltzmann distribution.

In the present work, stereochemistry was tracked only when there were two chiral centers, and inversion reactions were not considered. While significant inversion about closed shell carbons likely requires much higher temperatures than those in the present work, it would be helpful to pinpoint when inversion reactions need to be considered. The conformers of unsaturated radicals, which are abundant in the mechanisms of 2,4-dimethyloxetanyl and 2-ethyloxetanyl radicals, were not treated separately and may affect the kinetics of

the system. Moreover, isomerization pathways for alkene radicals were identified and are accessible under low-temperature combustion-relevant conditions.

Exploring chemical kinetics mechanisms for large reactive systems with quantum chemistry would benefit from more effective, on-the-fly pruning methods. The flux criterion applied in the present work has an advantage over the use of a simple barrier threshold alone. However, 5% of flux from an early well is usually more significant than 5% of flux from a later well, which itself may represent as little as 5% of the flux from previous wells. Furthermore, there are some pathways with low flux, such as ketohydroperoxides, which have a dramatic effect on observables like ignition delay time. The Reaction Mechanism Generator (RMG) software from MIT[78,79] has a parameter used to select reactions to be included in a chemical kinetics mechanism, which is based on this idea.

As a whole, this body of will strengthen the community's understanding of the balance between chain-propagation and chain-branching reactions of QOOH, which determines the reactivity of alkane fuels.

Appendix A

Potential Energy Surfaces

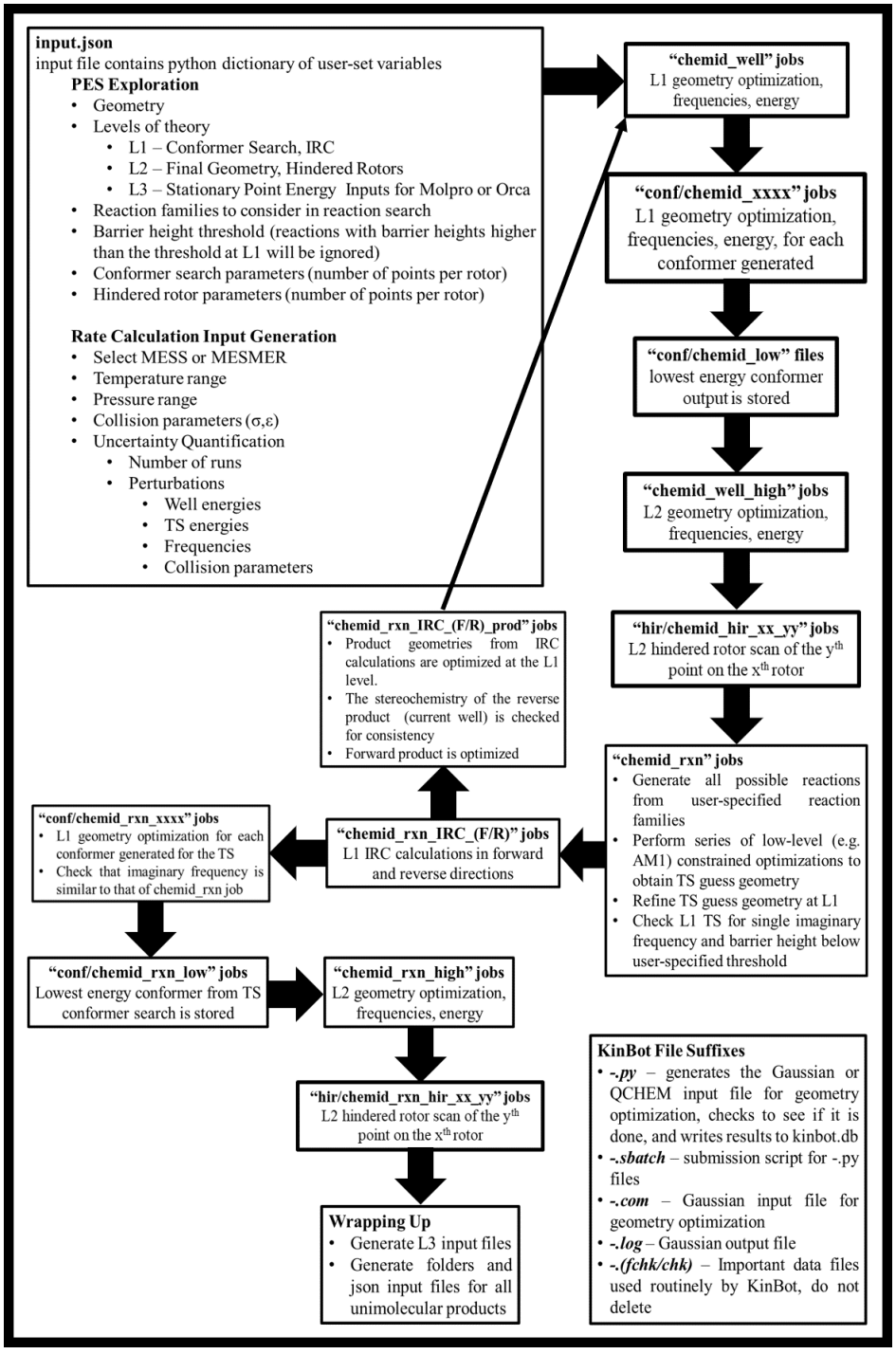

Figure A.1: An overview of the KinBot algorithm is provided.

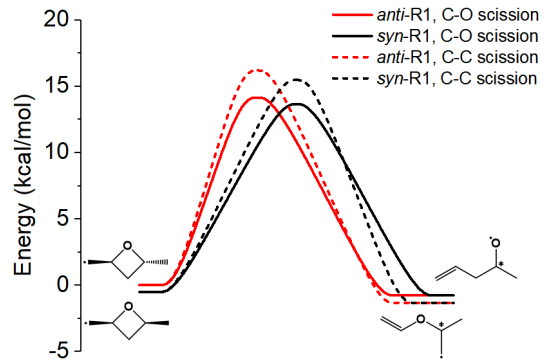

(a)

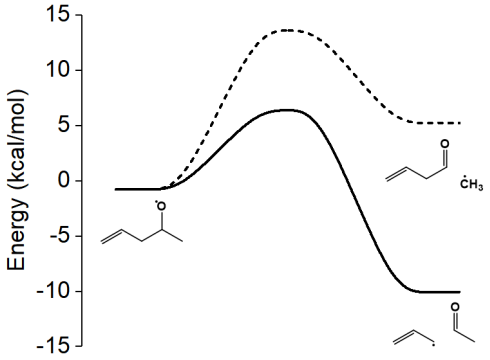

(b)

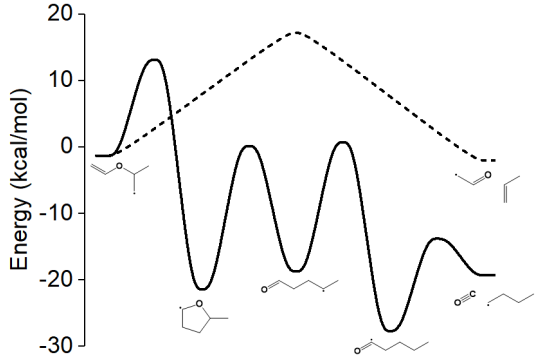

(c)

Figure A.2: Potential energy surfaces for the unimolecular decomposition of *syn*- and *anti*-DMOR1 at the L3 = CCSD(T)-F12/cc-pVTZ-F12 level of theory.

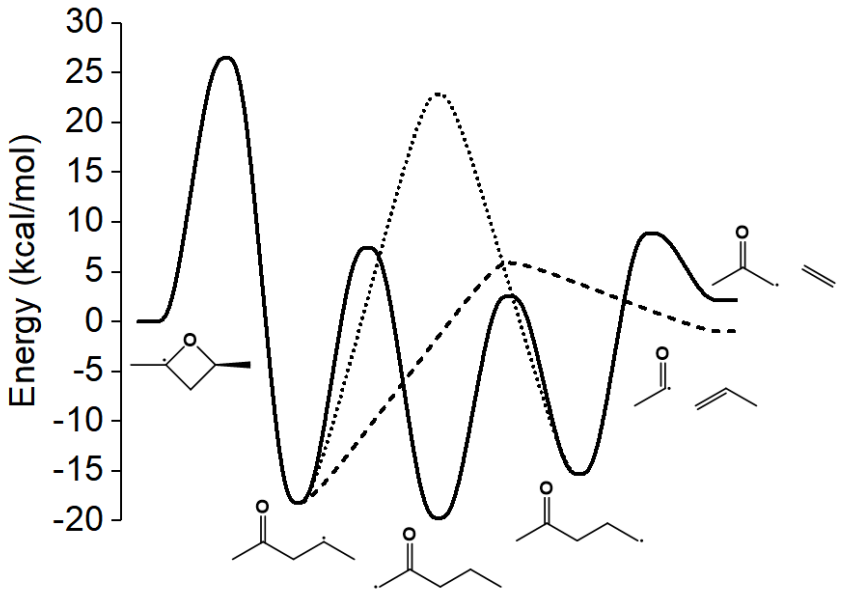

Figure A.3: Potential energy surface for unimolecular decomposition of DMOR2 at the L3 = CCSD(T)-F12/cc-pVTZ-F12 level of theory.

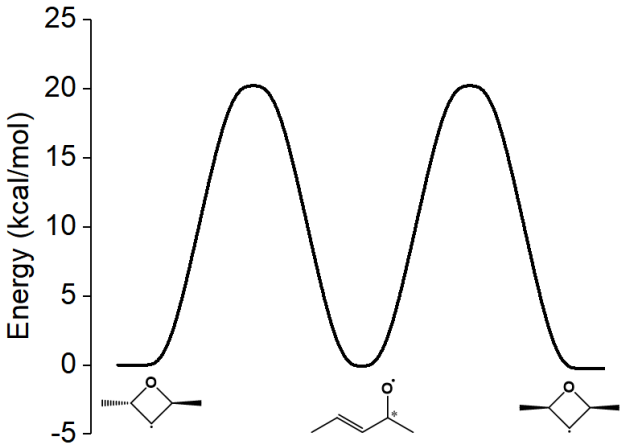

a)

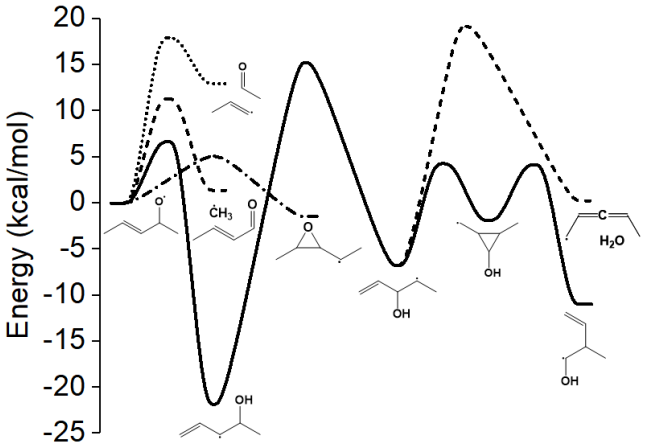

b)

Figure A.4: Potential energy surfaces for unimolecular decomposition of *syn*- and *anti*-DMOR3 at the L3 = CCSD(T)-F12/cc-pVTZ-F12 level of theory.

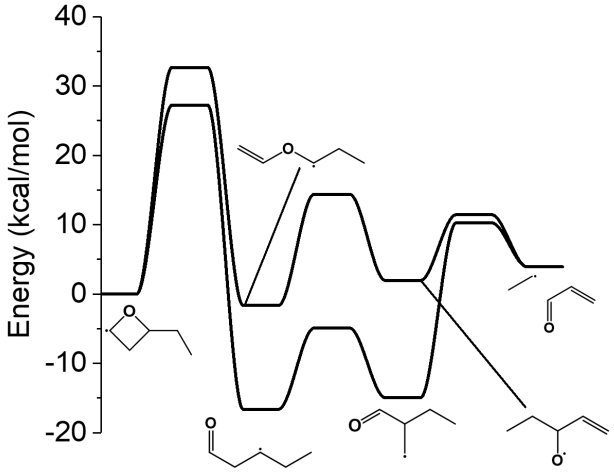

Figure A.5: Potential energy surface for unimolecular decomposition of EOR1 at the L3 = CCSD(T)-F12/cc-pVTZ-F12 level of theory.

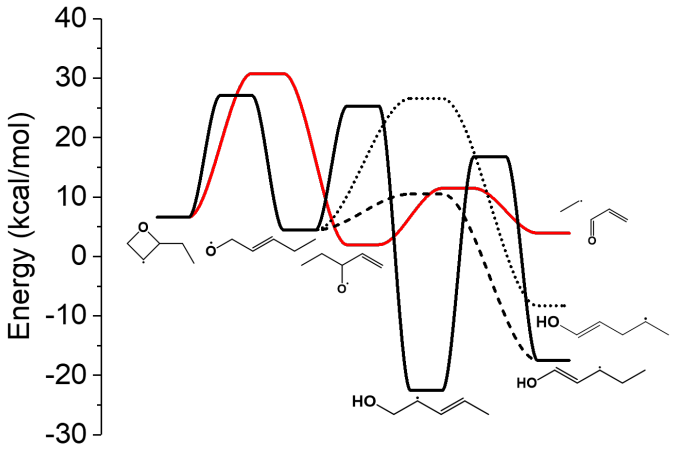

a)

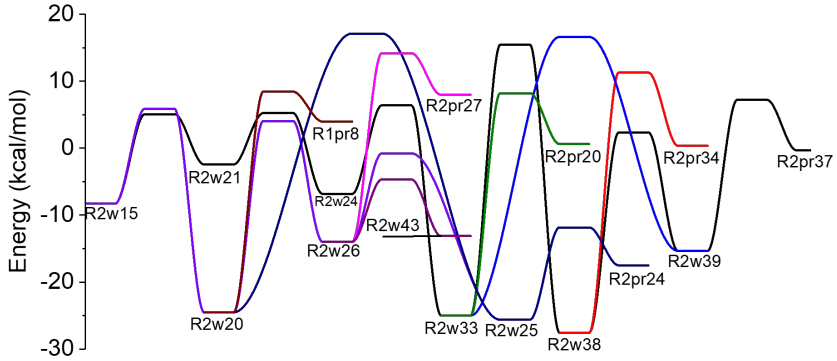

b)

Figure A.6: Potential energy surfaces for unimolecular decomposition of EOR2 are provided at the L3 = CCSD(T)-F12/cc-pVTZ-F12 level of theory.

Abbreviation	SMILES	Structure
R2w15	C[CH]C/C=C\O	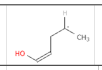
R2w20	CCCC=C[O]	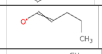
R2w21	C[C@@H]1C[C@@H]1[CH]O	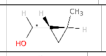
R2w24	[CH2][C@@H](C)/C=C/O	
R2w26	[CH2]CCCC=O	
R2w43	C1CCC(C1)[O]	
R2w33	CC(C)C=C[O]	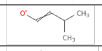
R2w25	CCCC[C]=O	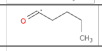
R2w38	CC(C)C[C]=O	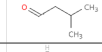
R2w39	[CH2][C@@H](C)CC=O	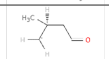
R1pr8	[H][C](=[O])[C]([H])=[C]([H])[H] [H][C]([H])[C]([H])([H])[H]	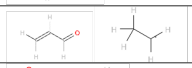
R2pr27	[CH2]CC=O C=C	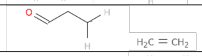
R2pr20	C/C=C/C=O [CH3]	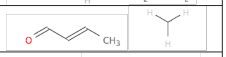
R2pr24	[C-]#[O+] [CH2]CCC	
R2pr34	C=C=O C[CH]C	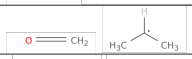
R2pr37	C=C[O] C=CC	

Figure A.7: A key for the structures referenced in Figure A.6b is given including the abbreviation, the SMILES code, and the structure.

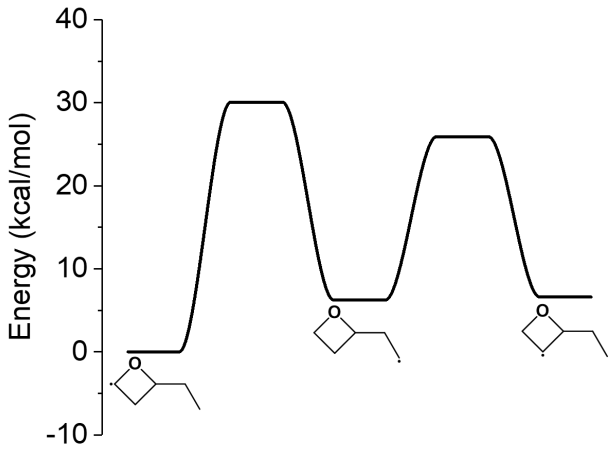

Figure A.8: Potential energy surface for unimolecular decomposition of EOR5 at the L3 = CCSD(T)-F12/cc-pVTZ-F12 level of theory.

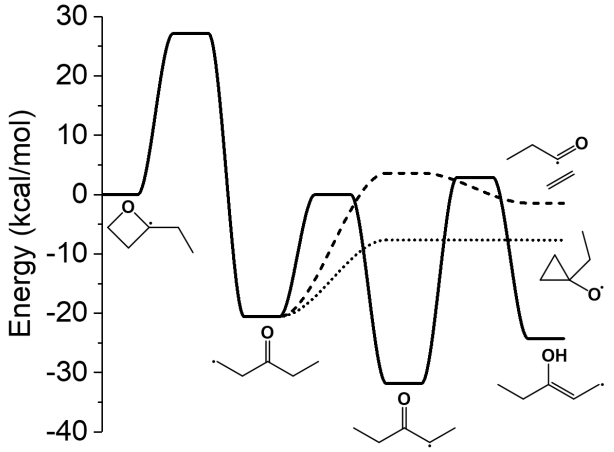

Figure A.9: Potential energy surface for unimolecular decomposition of EOR3 at the L3 = CCSD(T)-F12/cc-pVTZ-F12 level of theory.

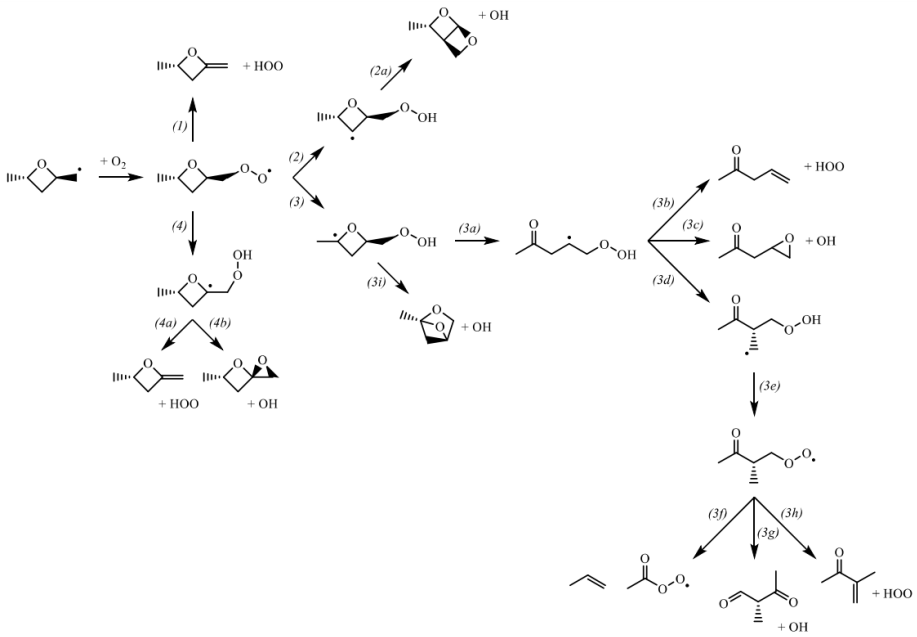

Figure A.10: Reaction scheme for *anti*-DMOROO1

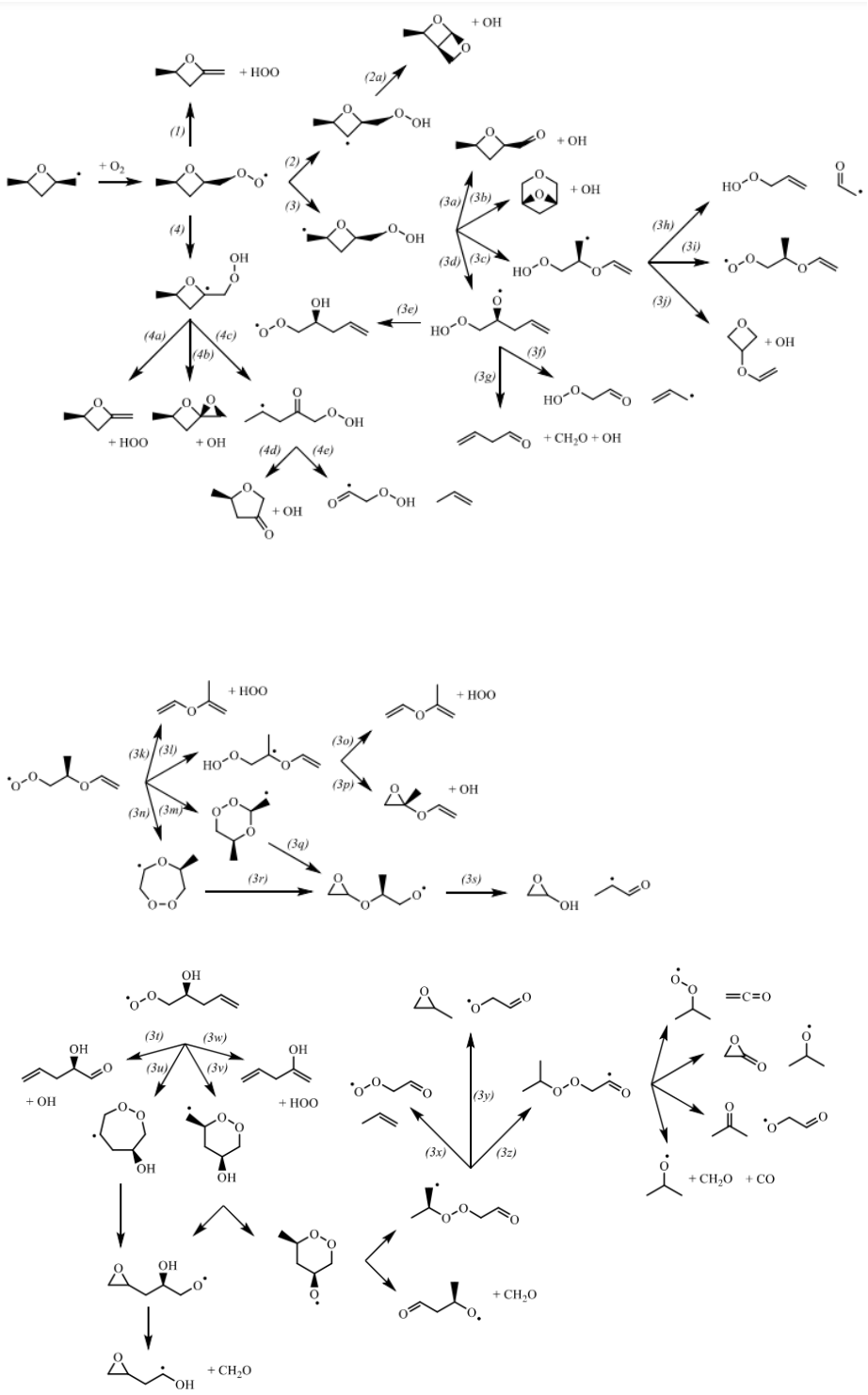

Figure A.11: Reaction scheme for *syn*-DMOROO1

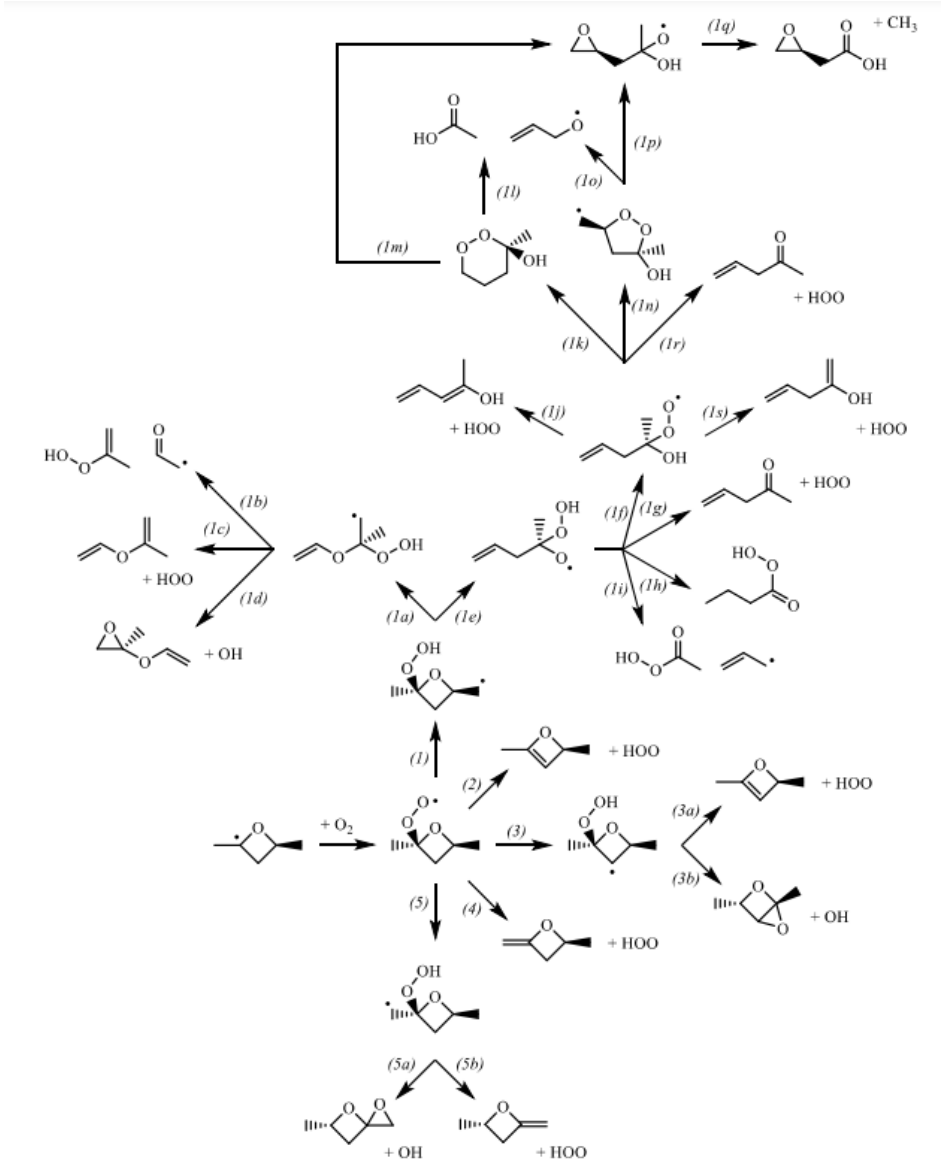

Figure A.12: Reaction scheme for *anti*-DMOROO2

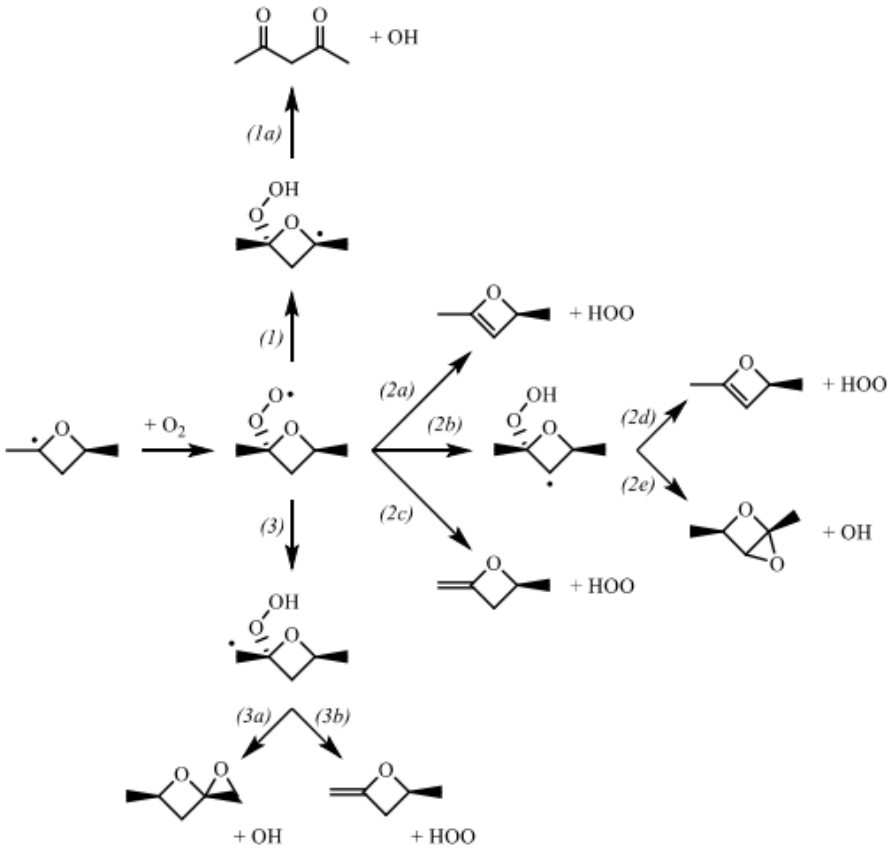

Figure A.13: Reaction scheme for *syn*-DMOROO2

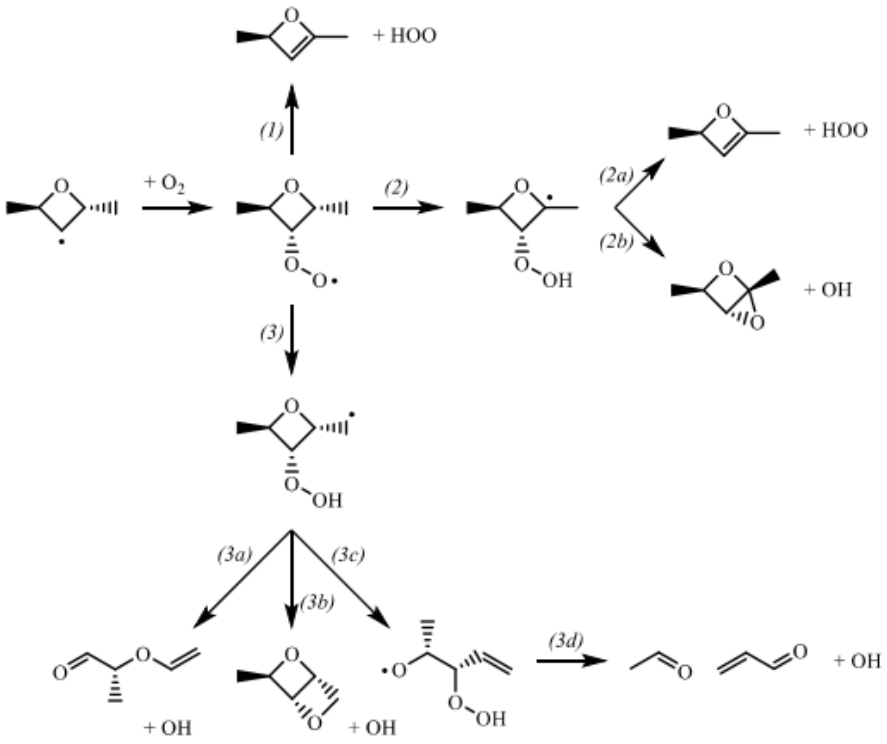

Figure A.14: Reaction scheme for *anti*-DMOROO3

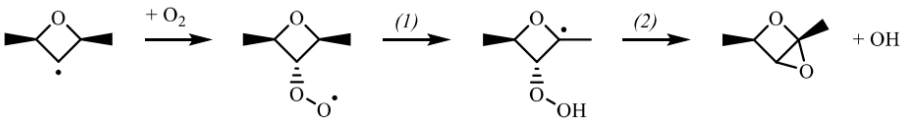

Figure A.15: Reaction scheme for *syn-anti*-DMOROO3

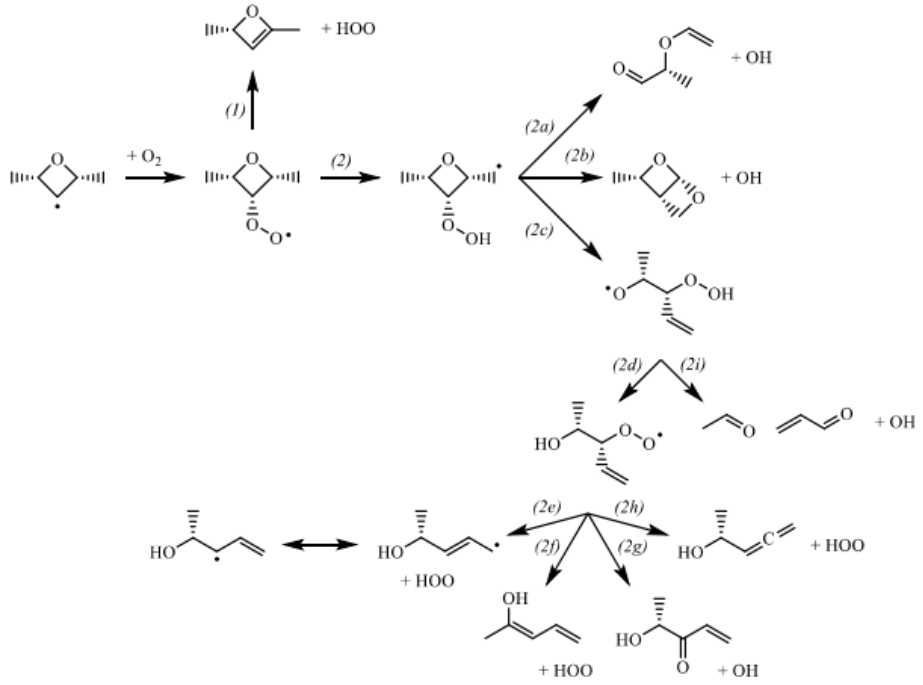

Figure A.16: Reaction scheme for *syn*-*syn*-DMOROO3

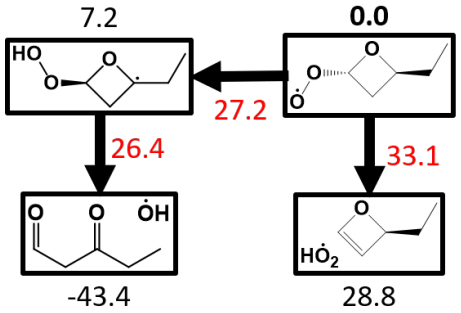

Figure A.17: Potential energy surface at the L3 = CCSD(T)-F12/cc-pVDZ-F12 level of theory for *anti*-EOROO1

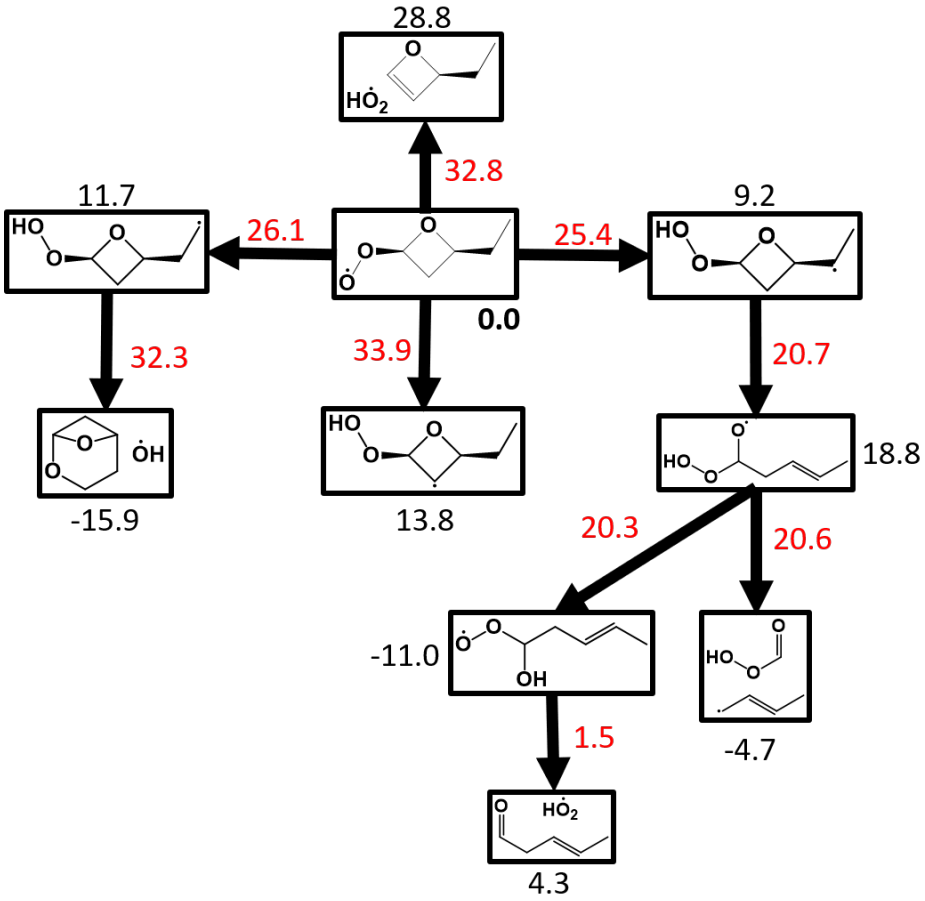

Figure A.18: Potential energy surface at the L3 = CCSD(T)-F12/cc-pVDZ-F12 level of theory for *syn*-EOROO1

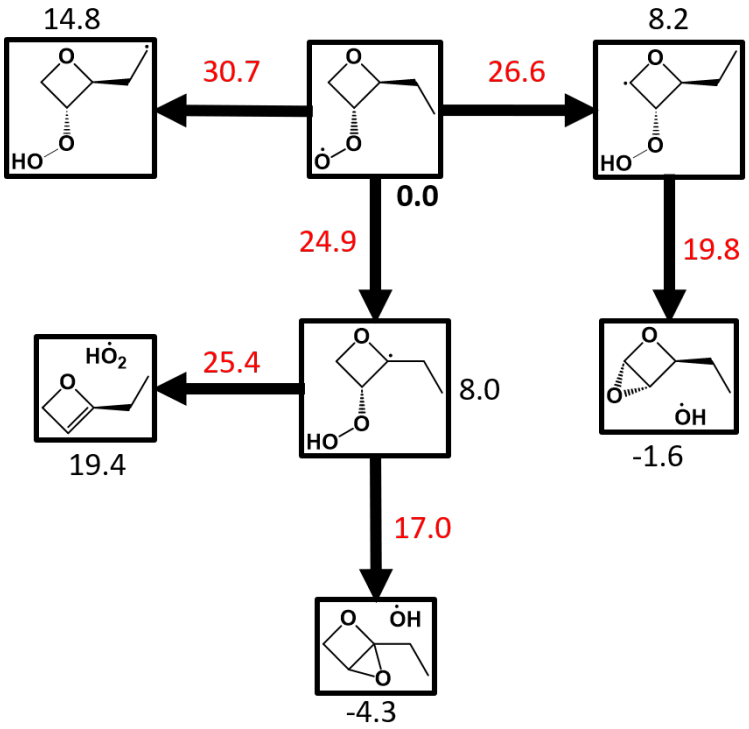

Figure A.19: Potential energy surface at the L3 = CCSD(T)-F12/cc-pVDZ-F12 level of theory for *anti*-EOROO2

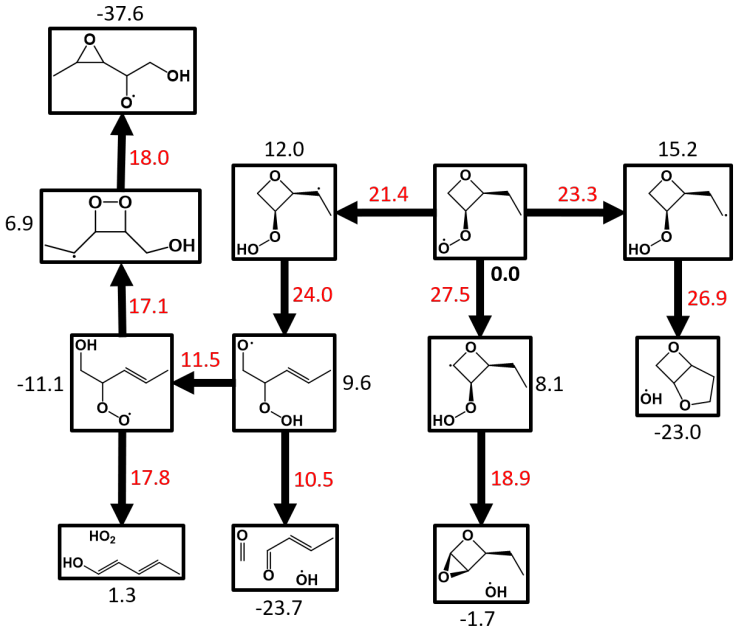

Figure A.20: Potential energy surface at the L3 = CCSD(T)-F12/cc-pVDZ-F12 level of theory for *syn*-EOROO2

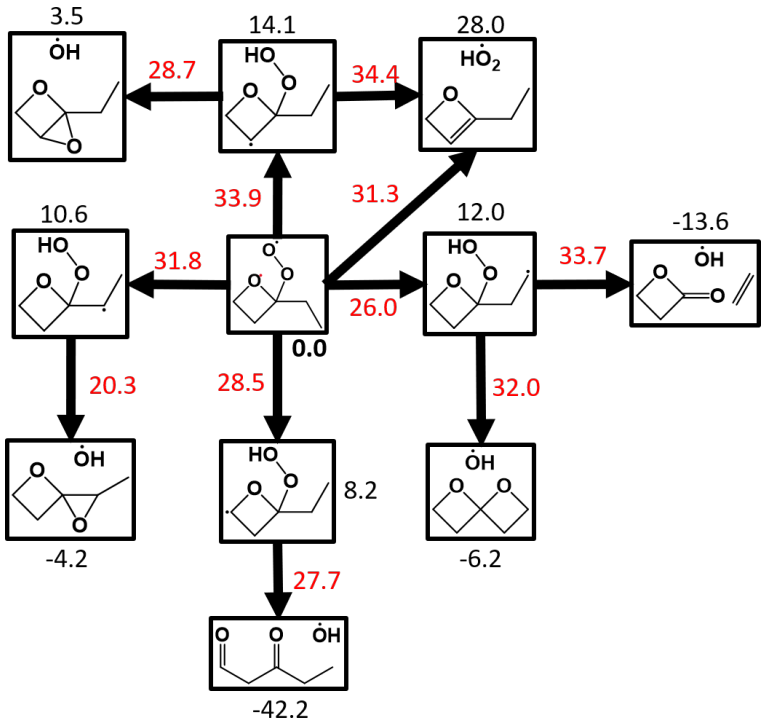

Figure A.21: Potential energy surface at the L3 = CCSD(T)-F12/cc-pVDZ-F12 level of theory for EOROO3

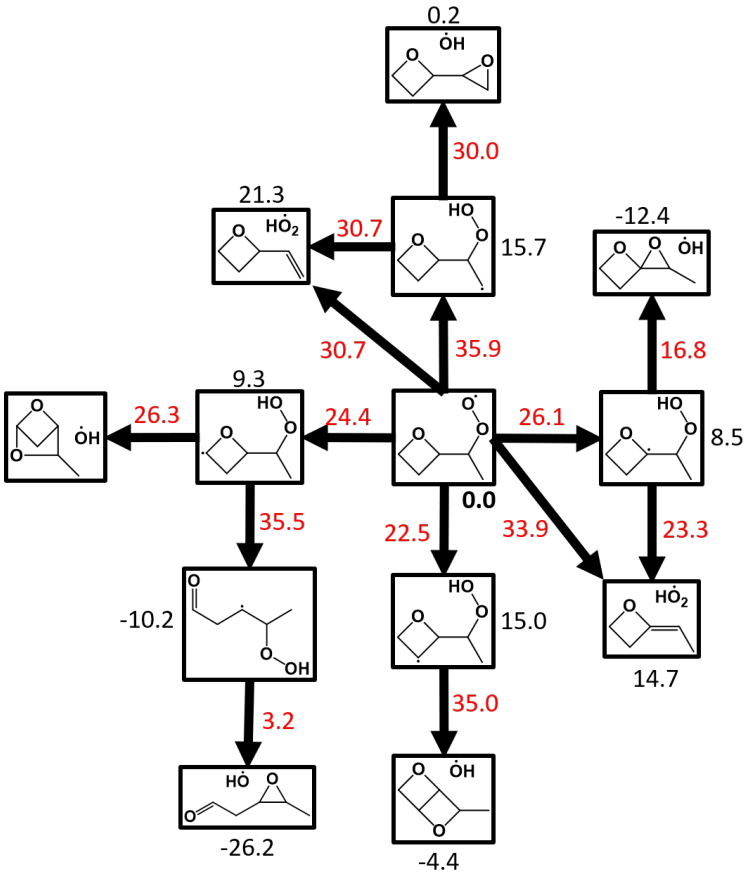

Figure A.22: Potential energy surface at the L3 = CCSD(T)-F12/cc-pVDZ-F12 level of theory for EOROO4

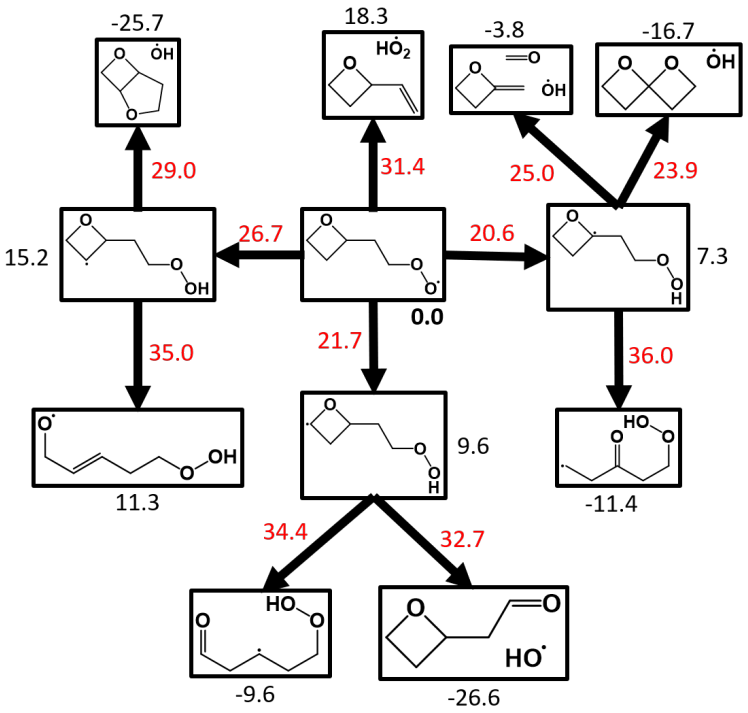

Figure A.23: Potential energy surface at the L3 = CCSD(T)-F12/cc-pVDZ-F12 level of theory for EOROO5

Appendix B

Rate Coefficients and Branching Fractions

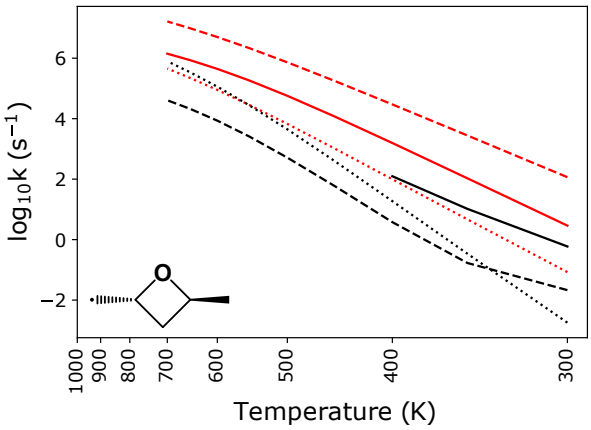

Figure B.1: The rate coefficients for unimolecular decomposition of *anti*-DMOR1 is given with the same legend as *syn*-DMOR1 in Chapter 5.

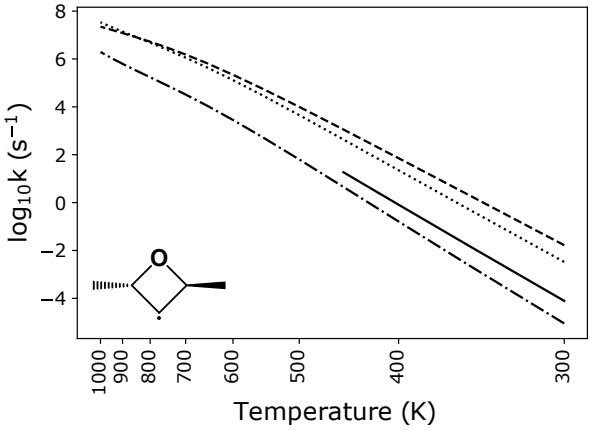

Figure B.2: The rate coefficients for unimolecular decomposition of *anti*-DMOR3 is given with the same legend as *syn*-DMOR3 in Chapter 5.

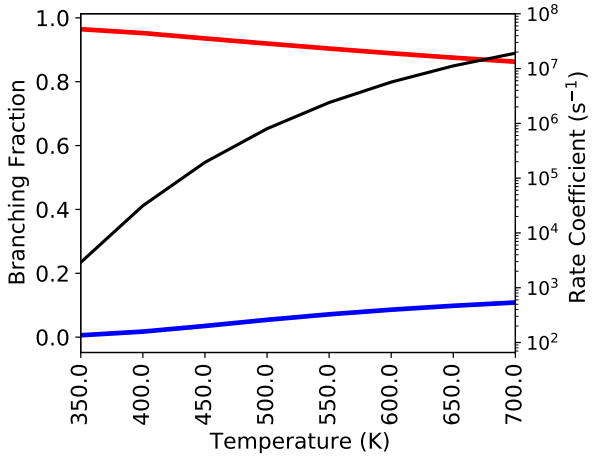

Figure B.3: The branching fractions for decomposition of anti-DMOR1 are shown. Red corresponds to acetaldehyde and allyl. Blue corresponds to vinoxy and propene. In black, the total rate coefficient is provided on a logarithmic scale.

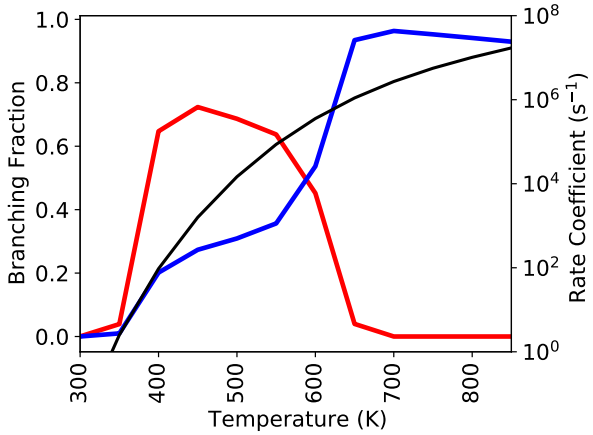

Figure B.4: The branching fractions for decomposition of anti-DMOR3 are shown. Blue corresponds to 2-butenal and methyl. Red corresponds to 1-penten-4-ol-3-yl. In black, the total rate coefficient is provided on a logarithmic scale.

Appendix C

Binary Classification of VUV Absorption Spectra

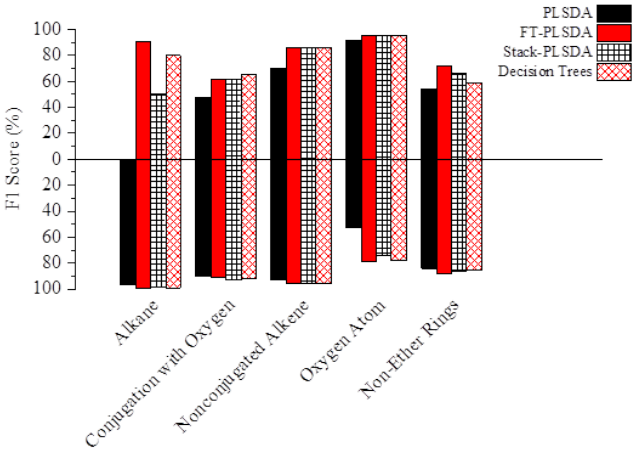

Figure C.1: The F1 scores for each binary classification model is provided.

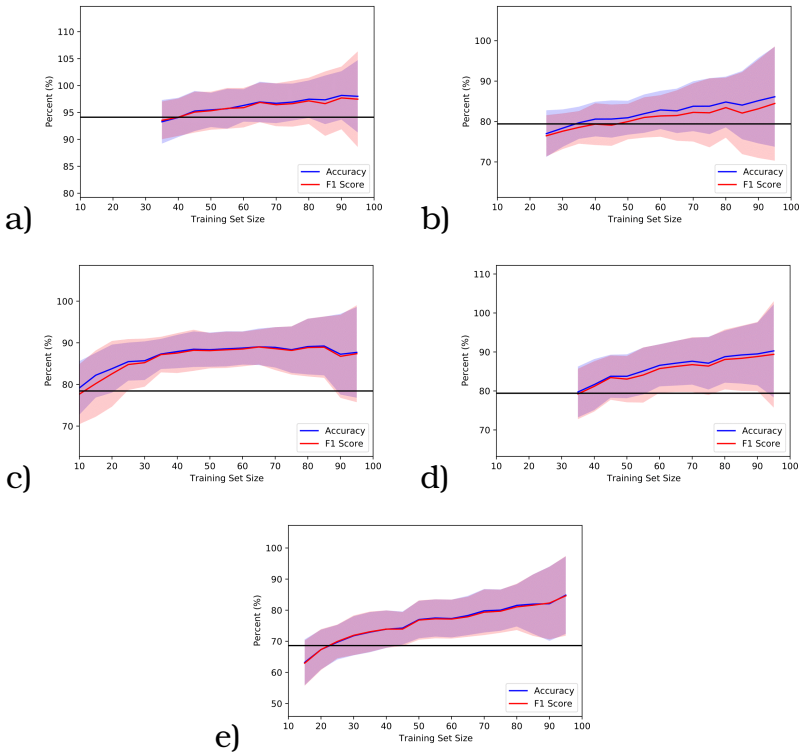

Figure C.2: Learning curves for each of the most accurate binary classification mdoels are provided. (a) is the alkanes model which uses function transformations and PLS-DA. (b) is the conjugation with oxygen model, which uses function transformations, stacking, and PLS-DA. (c) is the non-conjugated alkenes model, which uses decision trees. (d) is the oxygen presence model which uses function transformations and PLS-DA. (e) is the homocyclic model which uses function transformations and PLS-DA.

cross_validate_it(classifier, data, y, functions = None, stack = None, nc = 10)

- uses “leave-one-out” cross validation
- prints misclassified species
- prints accuracy metrics (accuracy, false positive rate, false negative rate, precision, recall)
- classifier (*function*) options
  - plsda (partial least squares discriminant analysis)
  - rfc (sklearn’s random forest classifier)
  - etc (sklearn’s extra trees classifier)
- data (*pandas df*) is read in from excel file in pandas format where rows are samples and columns are absorption cross-section values in Mb
- y (*str*) options
  - ‘alkane’
  - ‘nonconjugated alkene’
  - ‘conjugation with oxygen’
  - ‘rings noncyclic ether’
  - ‘oxygen atom’
  - additional categories may be added as entries in the y_dict where the key is a string describing the classification and the value is a list of binary classifications for each species in order
- functions (*list of functions*) options
  - inverse_morse
  - expm1
  - sqrt
  - morse
  - inverse_gauss_p1
  - inverse_laplace
  - sin2
  - squared
  - cubedx
  - inverse_cauchy
- stack (*str*) options are same as y
- nc (*int*) number of components

Figure C.3: A color-coded guide is provided for the function which cross-validates a model with the parameters supplied by the user.

```
pd_excel = pd.read_excel("dataset.xlsx") #read data from file in quotes
energies = pd_excel.iloc[:,0] #get the photon energies from the zeroth col
data =pd_excel.iloc[:,1:] # get the spectra from the first column and beyond
col = list(data.columns) # get the species names in order
y_dict['oxygen'] = [1,0,1,1,1,0,1,1,1,1,1,0,0,1,1,1,1,1,1,1,1,1,1,1,0,0,1,1,1,1,1,1,1,1,1,1,0,
                    1,1,1,1,1,1,1,1,1,0,1,1,1,1,1,0,1,1,1,0,1,1,0,1,1,0,1,1,0,0,1,1,0,1,1,1,0,1,1,0,
                    1,1,1,1,1,1,1,0,1,1,1,0,0,1,1,1,1,1,1,1,0,1,1,1,1] # 0 if no oxygen, 1 if oxygen
nco=1 # number of components for the extra (stacked) PLS regression data
nc_ft=[4,7] # number of components for each function transformation in the same order supplied below
cross_validate_it(etc, #extra trees classifier
                  data, #read from excel file
                  'oxygen', #classification selected, str is key for y_dict as shown above
                  functions=[np.log1p, gaussian], # function transformations to be applied
                  stack ='oxygen', # y_dict key corresponding to classification to be "stacked"
                  nc =1) #number of components for the final prediction
```

```
Species Classified Incorrectly:
    1,5-hexadiene-3-ol
    cis-2-butene
    cyclohexane
    cyclopentene
    ethane
    ethylene
    n-butane
    propene

Cross-Validation Accuracy: 92.2%

False Positive Rate: 33.3%
(portion of negatives predicted positive)

False Negative Rate: 1.2%
(portion of positives predicted negative)

              precision    recall  f1-score   support

           0       0.93      0.67      0.78        21
           1       0.92      0.99      0.95        81

    accuracy                           0.92       102
   macro avg       0.93      0.83      0.87       102
weighted avg       0.92      0.92      0.92       102


Precision: portion of predicted positives that are actually positive
Recall: portion of positives predicted positive
F1-score: weighted average of precision and recall
Macro average: mean of the binary metrics
Weighted average: average of binary metrics in which each class's score is weighted by its presence in th
e true data sample
```

Figure C.4: A sample input and output for a model for binary classification of spectra based on presence of oxygen are provided.

Bibliography

[1] Energy Information Administration. *INTERNATIONAL ENERGY OUTLOOK 2021*. 2021. URL: https://www.eia.gov/outlooks/ieo/.

[2] N Blin-Simiand et al. "Hydroperoxides with zero, one, two or more carbonyl groups formed during the oxidation of n-dodecane". In: *Combustion and Flame* 126.1 (2001), pp. 1524–1532. ISSN: 0010-2180. DOI: https://doi.org/10.1016/S0010-2180(01)00264-4. URL: https://www.sciencedirect.com/science/article/pii/S0010218001002644.

[3] Yan-Ting Ke et al. "Multigram Synthesis of a Combustion-Relevant -Ketohydroperoxide through Sulfonylhydrazine Substitution". In: *Chemistry – A European Journal* 28.62 (2022), e202202266. DOI: https://doi.org/10.1002/chem.202202266. eprint: https://chemistry-europe.onlinelibrary.wiley.com/doi/pdf/10.1002/chem.202202266. URL: https://chemistry-europe.onlinelibrary.wiley.com/doi/abs/10.1002/chem.202202266.

[4] Colin A. Grambow et al. "Unimolecular Reaction Pathways of a -Ketohydroperoxide from Combined Application of Automated Reaction Discovery Methods". In: *Journal of the American Chemical Society* 140.3 (2018). PMID: 29271202, pp. 1035–1048. DOI: 10.1021/jacs.7b11009. eprint: https://doi.org/10.1021/jacs.7b11009. URL: https://doi.org/10.1021/jacs.7b11009.

[5] Amrit Jalan et al. "New Pathways for Formation of Acids and Carbonyl Products in Low-Temperature Oxidation: The Korcek Decomposition of -Ketohydroperoxides". In: *Journal of the American Chemical Society* 135.30 (2013). PMID: 23862563, pp. 11100–11114. DOI: 10.1021/

ja4034439. eprint: https://doi.org/10.1021/ja4034439. URL: https://doi.org/10.1021/ja4034439.

[6] Liming Cai et al. "Optimized reaction mechanism rate rules for ignition of normal alkanes". In: *Combustion and Flame* 173 (2016), pp. 468–482. ISSN: 0010-2180. DOI: https://doi.org/10.1016/j.combustflame.2016.04.022. URL: https://www.sciencedirect.com/science/article/pii/S0010218016300724.

[7] Kevin J. Hughes et al. "Evaluation of models for the low temperature combustion of alkanes through interpretation of pressure–temperature ignition diagrams". In: *Phys. Chem. Chem. Phys.* 8 (27 2006), pp. 3197–3210. DOI: 10.1039/B605379C. URL: http://dx.doi.org/10.1039/B605379C.

[8] Brandon Rotavera and Craig A. Taatjes. "Influence of functional groups on low-temperature combustion chemistry of biofuels". In: *Progress in Energy and Combustion Science* 86 (2021), p. 100925. ISSN: 0360-1285. DOI: https://doi.org/10.1016/j.pecs.2021.100925. URL: https://www.sciencedirect.com/science/article/pii/S036012852100023X.

[9] J. A. Montgomery et al. "A complete basis set model chemistry. VII. Use of the minimum population localization method". In: *The Journal of Chemical Physics* 112.15 (2000), pp. 6532–6542. DOI: 10.1063/1.481224. eprint: https://doi.org/10.1063/1.481224. URL: https://doi.org/10.1063/1.481224.

[10] Kieran P. Somers and John M. Simmie. "Benchmarking Compound Methods (CBS-QB3, CBS-APNO, G3, G4, W1BD) against the Active Thermochemical Tables: Formation Enthalpies of Radicals". In: *The Journal of Physical Chemistry A* 119.33 (2015). PMID: 26171842, pp. 8922–8933. DOI: 10.1021/acs.jpca.5b05448. eprint: https://doi.org/10.1021/acs.jpca.5b05448. URL: https://doi.org/10.1021/acs.jpca.5b05448.

[11] Ahren W. Jasper and James A. Miller. "Lennard–Jones parameters for combustion and chemical kinetics modeling from full-dimensional intermolecular potentials".

In: *Combustion and Flame* 161.1 (2014), pp. 101–110. ISSN: 0010-2180. DOI: https://doi.org/10.1016/j.combustflame.2013.08.004. URL: https://www.sciencedirect.com/science/article/pii/S0010218013002988.

[12] Ahren W. Jasper. ""Third-body" collision parameters for hydrocarbons, alcohols, and hydroperoxides and an effective internal rotor approach for estimating them". In: *International Journal of Chemical Kinetics* 52.6 (2020), pp. 387–402. ISSN: 0538-8066. DOI: https://doi.org/10.1002/kin.21358. URL: https://onlinelibrary.wiley.com/doi/abs/10.1002/kin.21358.

[13] Yuri Georgievskii and Stephen J. Klippenstein. "Variable reaction coordinate transition state theory: Analytic results and application to the C2H3+H→C2H4 reaction". In: *The Journal of Chemical Physics* 118.12 (2003), pp. 5442–5455. DOI: 10.1063/1.1539035. eprint: https://doi.org/10.1063/1.1539035. URL: https://doi.org/10.1063/1.1539035.

[14] Maximilien Cord et al. "Improvement of the Modeling of the Low-Temperature Oxidation of n-Butane: Study of the Primary Reactions". In: *The Journal of Physical Chemistry A* 116.24 (2012). PMID: 22257166, pp. 6142–6158. DOI: 10.1021/jp211434f. eprint: https://doi.org/10.1021/jp211434f. URL: https://doi.org/10.1021/jp211434f.

[15] John Bugler et al. "An experimental and modelling study of n-pentane oxidation in two jet-stirred reactors: The importance of pressure-dependent kinetics and new reaction pathways". In: *Proceedings of the Combustion Institute* 36.1 (2017), pp. 441–448. ISSN: 1540-7489. DOI: https://doi.org/10.1016/j.proci.2016.05.048. URL: https://www.sciencedirect.com/science/article/pii/S1540748916300487.

[16] Anna C. Doner, Judit Zádor, and Brandon Rotavera. "Stereoisomer-dependent unimolecular kinetics of 2,4-dimethyloxetanyl peroxy radicals". In: *Faraday Discuss.* 238 (0 2022), pp. 295–319. DOI: 10.1039/D2FD00029F. URL: http://dx.doi.org/10.1039/D2FD00029F.

[17] Aaron D. Danilack et al. “Diastereomers and Low-Temperature Oxidation”. In: *The Journal of Physical Chemistry A* 125.36 (2021). PMID: 34469163, pp. 8064–8073. DOI: 10.1021/acs.jpca.1c05635. eprint: https://doi.org/10.1021/acs.jpca.1c05635. URL: https://doi.org/10.1021/acs.jpca.1c05635.

[18] Jacob C. Davis et al. “Influence of the Ether Functional Group on Ketohydroperoxide Formation in Cyclic Hydrocarbons: Tetrahydropyran and Cyclohexane”. In: *The Journal of Physical Chemistry A* 123.17 (2019). PMID: 30865470, pp. 3634–3646. DOI: 10.1021/acs.jpca.8b12510. eprint: https://doi.org/10.1021/acs.jpca.8b12510. URL: https://doi.org/10.1021/acs.jpca.8b12510.

[19] Alanna L. Koritzke et al. “QOOH-mediated reactions in cyclohexene oxidation”. In: *Proceedings of the Combustion Institute* 37.1 (2019), pp. 323–335. ISSN: 1540-7489. DOI: https://doi.org/10.1016/j.proci.2018.05.029. URL: https://www.sciencedirect.com/science/article/pii/S1540748918300300.

[20] Anna C. Doner et al. “Isomer-dependent reaction mechanisms of cyclic ether intermediates: cis-2,3-dimethyloxirane and trans-2,3-dimethyloxirane”. In: *International Journal of Chemical Kinetics* 53.1 (2021), pp. 127–145. DOI: https://doi.org/10.1002/kin.21429. eprint: https://onlinelibrary.wiley.com/doi/pdf/10.1002/kin.21429. URL: https://onlinelibrary.wiley.com/doi/abs/10.1002/kin.21429.

[21] Matthew G. Christianson et al. “Reaction mechanisms of a cyclic ether intermediate: Ethyloxirane”. In: *International Journal of Chemical Kinetics* 53.1 (2021), pp. 43–59. DOI: https://doi.org/10.1002/kin.21423. eprint: https://onlinelibrary.wiley.com/doi/pdf/10.1002/kin.21423. URL: https://onlinelibrary.wiley.com/doi/abs/10.1002/kin.21423.

[22] Alanna L. Koritzke et al. “Fragmentation mechanisms from electron-impact of complex cyclic ethers formed in combustion”. In: *International Journal of Mass Spec-*

trometry 454 (2020), p. 116342. ISSN: 1387-3806. DOI: https://doi.org/10.1016/j.ijms.2020.116342. URL: https://www.sciencedirect.com/science/article/pii/S138738062030049X.

[23] Melvin B. Robin. "CHAPTER I - A Catalog of Orbitals and Excitations in Polyatomic Molecules". In: *Higher Excited States of Polyatomic Molecules*. Ed. by Melvin B. Robin. Academic Press, 1985, pp. 1–47. ISBN: 978-0-12-589903-1. DOI: https://doi.org/10.1016/B978-0-12-589903-1.50005-9. URL: https://www.sciencedirect.com/science/article/pii/B9780125899031500059.

[24] Anna C. Doner et al. "Machine learning models for binary molecular classification using VUV absorption spectra". In: *Journal of Quantitative Spectroscopy and Radiative Transfer* 297 (2023), p. 108438. ISSN: 0022-4073. DOI: https://doi.org/10.1016/j.jqsrt.2022.108438. URL: https://www.sciencedirect.com/science/article/pii/S0022407322003739.

[25] Anne S. Hansen et al. "Watching a hydroperoxyalkyl radical (•QOOH) dissociate". In: *Science* 373.6555 (2021), pp. 679–682. DOI: 10.1126/science.abj0412. eprint: https://www.science.org/doi/pdf/10.1126/science.abj0412. URL: https://www.science.org/doi/abs/10.1126/science.abj0412.

[26] John Bugler, Jennifer Power, and Henry J. Curran. "A theoretical study of cyclic ether formation reactions". In: *Proceedings of the Combustion Institute* 36.1 (2017), pp. 161–167. ISSN: 1540-7489. DOI: https://doi.org/10.1016/j.proci.2016.05.006. URL: https://www.sciencedirect.com/science/article/pii/S1540748916300062.

[27] Alanna L. Koritzke et al. "Probing O2-dependence of tetrahydrofuranyl reactions via isomer-resolved speciation". In: *Combustion and Flame* (2023), p. 112640. ISSN: 0010-2180. DOI: https://doi.org/10.1016/j.combustflame.2023.112640. URL: https://www.sciencedirect.com/science/article/pii/S0010218023000251.

[28] Ivan O. Antonov et al. "Pressure-Dependent Competition among Reaction Pathways from First- and Second-O2 Additions in the Low-Temperature Oxidation of Tetrahydrofuran". In: *The Journal of Physical Chemistry A* 120.33 (2016). PMID: 27441526, pp. 6582–6595. DOI: 10.1021/acs.jpca.6b05411. eprint: https://doi.org/10.1021/acs.jpca.6b05411. URL: https://doi.org/10.1021/acs.jpca.6b05411.

[29] Yann Fenard et al. "A model of tetrahydrofuran low-temperature oxidation based on theoretically calculated rate constants". In: *Combustion and Flame* 191 (2018), pp. 252–269. ISSN: 0010-2180. DOI: https://doi.org/10.1016/j.combustflame.2018.01.006. URL: https://www.sciencedirect.com/science/article/pii/S0010218018300105.

[30] John M. Simmie. "Kinetics and Thermochemistry of 2,5-Dimethyltetrahydrofuran and Related Oxolanes: Next Next-Generation Biofuels". In: *The Journal of Physical Chemistry A* 116.18 (2012). PMID: 22494635, pp. 4528–4538. DOI: 10.1021/jp301870w. eprint: https://doi.org/10.1021/jp301870w. URL: https://doi.org/10.1021/jp301870w.

[31] Y. Fenard, M.A. Boumehdi, and G. Vanhove. "Experimental and kinetic modeling study of 2-methyltetrahydrofuran oxidation under engine-relevant conditions". In: *Combustion and Flame* 178 (2017), pp. 168–181. ISSN: 0010-2180. DOI: https://doi.org/10.1016/j.combustflame.2017.01.008. URL: https://www.sciencedirect.com/science/article/pii/S0010218017300081.

[32] Josep M. Anglada, Ramon Crehuet, and Joseph S. Francisco. "The Stability of -Hydroperoxyalkyl Radicals". In: *Chemistry – A European Journal* 22.50 (2016), pp. 18092–18100. DOI: https://doi.org/10.1002/chem.201604499. eprint: https://chemistry-europe.onlinelibrary.wiley.com/doi/pdf/10.1002/chem.201604499. URL: https://chemistry-europe.onlinelibrary.wiley.com/doi/abs/10.1002/chem.201604499.

[33] Judit Zádor et al. "Automated Reaction Kinetics of Gas-Phase Organic Species over Multiwell Potential Energy

Surfaces". In: *The Journal of Physical Chemistry A* 0.0 (2023). PMID: 36607817, null. DOI: 10.1021/acs.jpca.2c06558. eprint: https://doi.org/10.1021/acs.jpca.2c06558. URL: https://doi.org/10.1021/acs.jpca.2c06558.

[34] Ruben Van de Vijver and Judit Zádor. "KinBot: Automated stationary point search on potential energy surfaces". In: *Computer Physics Communications* 248 (2020), p. 106947.

[35] *KinBot*. Computer Program. Version 2.1. 2019. URL: https://github.com/zadorlab/KinBot.

[36] Anna C. Doner, Judit Zádor, and Brandon Rotavera. "Unimolecular Reactions of 2,4-Dimethyloxetanyl Radicals". In: *The Journal of Physical Chemistry A* 0.0 (0). PMID: 36898134, null. DOI: 10.1021/acs.jpca.2c08290. eprint: https://doi.org/10.1021/acs.jpca.2c08290. URL: https://doi.org/10.1021/acs.jpca.2c08290.

[37] Nathan J. DeYonker, Thomas R. Cundari, and Angela K. Wilson. "The correlation consistent composite approach (ccCA): An alternative to the Gaussian-n methods". In: *The Journal of Chemical Physics* 124.11 (2006), p. 114104. DOI: 10.1063/1.2173988. eprint: https://doi.org/10.1063/1.2173988. URL: https://doi.org/10.1063/1.2173988.

[38] Nathan J. DeYonker et al. "Towards the intrinsic error of the correlation consistent Composite Approach (ccCA)". In: *Molecular Physics* 107.8-12 (2009), pp. 1107–1121. DOI: 10.1080/00268970902744359. eprint: https://doi.org/10.1080/00268970902744359. URL: https://doi.org/10.1080/00268970902744359.

[39] Akira Miyoshi. "Systematic Computational Study on the Unimolecular Reactions of Alkylperoxy (RO2), Hydroperoxyalkyl (QOOH), and Hydroperoxyalkylperoxy (O2QOOH) Radicals". In: *The Journal of Physical Chemistry A* 115.15 (2011). PMID: 21446694, pp. 3301–3325. DOI: 10.1021/jp112152n. eprint: https://doi.org/10.1021/jp112152n. URL: https://doi.org/10.1021/jp112152n.

[40] Y. Georgievskii and S. J. Klippenstein. *MESS.2016.3.23.* Computer Program.

[41] Yuri Georgievskii and Stephen J. Klippenstein. "Long-range transition state theory". In: *The Journal of Chemical Physics* 122.19 (2005), p. 194103. DOI: 10.1063/1.1899603. eprint: https://doi.org/10.1063/1.1899603. URL: https://doi.org/10.1063/1.1899603.

[42] T. M. Lenhardt, C. E. McDade, and K. D. Bayes. "RATES OF REACTION OF BUTYL RADICALS WITH MOLECULAR-OXYGEN". In: *Journal of Chemical Physics* 72.1 (1980). ISI Document Delivery No.: JB999 Times Cited: 91 Cited Reference Count: 38 Lenhardt, tm mcdade, ce bayes, kd Amer inst physics Woodbury, pp. 304–310. ISSN: 0021-9606. DOI: 10.1063/1.438848. URL: %3CGo%20to%20ISI%3E://WOS:A1980JB99900042.

[43] D. Wu and K. D. Bayes. "Rate constants for the reactions of isobutyl, neopentyl, cyclopentyl, and cyclohexyl radicals with molecular oxygen". In: *Int. J. Chem. Kinet.* 18 (1986), p. 547.

[44] F. Pedregosa et al. "Scikit-learn: Machine Learning in Python". In: *Journal of Machine Learning Research* 12 (2011), pp. 2825–2830.

[45] Samuel W. Hartness et al. "Probing O2 dependence of hydroperoxy-butyl reactions via isomer-resolved speciation". In: *Proceedings of the Combustion Institute* (2022). ISSN: 1540-7489. DOI: https://doi.org/10.1016/j.proci.2022.09.066. URL: https://www.sciencedirect.com/science/article/pii/S1540748922004837.

[46] Anna C. Doner et al. "Vacuum-ultraviolet absorption cross-sections of functionalized cyclic hydrocarbons: Six-membered rings". In: *Journal of Quantitative Spectroscopy and Radiative Transfer* 236 (2019), p. 106603. ISSN: 0022-4073. DOI: https://doi.org/10.1016/j.jqsrt.2019.106603. URL: https://www.sciencedirect.com/science/article/pii/S0022407319304637.

[47] Matthew G. Christianson et al. “Vacuum-ultraviolet absorption cross-sections of functionalized cyclic hydrocarbons: Five-membered rings”. In: *Journal of Quantitative Spectroscopy and Radiative Transfer* 258 (2021), p. 107274. ISSN: 0022-4073. DOI: https://doi.org/10.1016/j.jqsrt.2020.107274. URL: https://www.sciencedirect.com/science/article/pii/S0022407320304908.

[48] Anna C. Doner et al. “Vacuum-ultraviolet absorption cross-sections of functionalized four-carbon species”. In: *Journal of Quantitative Spectroscopy and Radiative Transfer* 292 (2022), p. 108346. ISSN: 0022-4073. DOI: https://doi.org/10.1016/j.jqsrt.2022.108346. URL: https://www.sciencedirect.com/science/article/pii/S0022407322002813.

[49] Olivier Herbinet et al. “Detailed product analysis during the low temperature oxidation of n-butane”. In: *Phys. Chem. Chem. Phys.* 13 (1 2011), pp. 296–308. DOI: 10.1039/C0CP00539H. URL: http://dx.doi.org/10.1039/C0CP00539H.

[50] Richard R. Baker, Roy R. Baldwin, and Raymond W. Walker. “Addition of n-butane to slowly reacting mixtures of hydrogen and oxygen at 480°C. Part 2.—Formation of oxygenated products”. In: *J. Chem. Soc., Faraday Trans. 1* 71 (0 1975), pp. 756–779. DOI: 10.1039/F19757100756. URL: http://dx.doi.org/10.1039/F19757100756.

[51] R. Minetti et al. “Experimental and modeling study of oxidation and autoignition of butane at high pressure”. In: *Combustion and Flame* 96.3 (1994), pp. 201–211. ISSN: 0010-2180. DOI: https://doi.org/10.1016/0010-2180(94)90009-4. URL: https://www.sciencedirect.com/science/article/pii/0010218094900094.

[52] Arkke J. Eskola et al. “Synchrotron Photoionization Mass Spectrometry Measurements of Product Formation in Low-Temperature n-Butane Oxidation: Toward a Fundamental Understanding of Autoignition Chemistry and n-C4H9 + O2/s-C4H9 + O2 Reactions”. In: *The Journal of Physical Chemistry A* 117.47 (2013). PMID:

24125058, pp. 12216–12235. DOI: 10.1021/jp408467g. eprint: https://doi.org/10.1021/jp408467g. URL: https://doi.org/10.1021/jp408467g.

[53] Jorge Aguilera-Iparraguirre et al. "Accurate Benchmark Calculation of the Reaction Barrier Height for Hydrogen Abstraction by the Hydroperoxyl Radical from Methane. Implications for CnH2n+2 where n = 2 → 4". In: *The Journal of Physical Chemistry A* 112.30 (2008). PMID: 18610940, pp. 7047–7054. DOI: 10.1021/jp8012464. eprint: https://doi.org/10.1021/jp8012464. URL: https://doi.org/10.1021/jp8012464.

[54] John D. DeSain et al. "Measurements, Theory, and Modeling of OH Formation in Ethyl + O2 and Propyl + O2 Reactions". In: *The Journal of Physical Chemistry A* 108.34 (2004), pp. 7127–7128. DOI: 10.1021/jp040467m. eprint: https://doi.org/10.1021/jp040467m. URL: https://doi.org/10.1021/jp040467m.

[55] Nils Hansen, Kai Moshammer, and Ahren W. Jasper. "Isomer-Selective Detection of Keto-Hydroperoxides in the Low-Temperature Oxidation of Tetrahydrofuran". In: *The Journal of Physical Chemistry A* 123.38 (2019). PMID: 31483667, pp. 8274–8284. DOI: 10.1021/acs.jpca.9b07017. eprint: https://doi.org/10.1021/acs.jpca.9b07017. URL: https://doi.org/10.1021/acs.jpca.9b07017.

[56] Jared D. Weidman et al. "High-level theoretical characterization of the vinoxy radical (•CH2CHO) + O2 reaction". In: *The Journal of Chemical Physics* 148.18 (2018), p. 184308. DOI: 10.1063/1.5026295. eprint: https://doi.org/10.1063/1.5026295. URL: https://doi.org/10.1063/1.5026295.

[57] Matthew M. Davis et al. "Characterization of the 2-methylvinoxy radical + O2 reaction: A focal point analysis and composite multireference study". In: *The Journal of Chemical Physics* 151.12 (2019), p. 124302. DOI: 10.1063/1.5113800. eprint: https://doi.org/10.1063/1.5113800. URL: https://doi.org/10.1063/1.5113800.

[58] Sukhdip Singh et al. "Kinetics and mechanism of the reactions of n-butanal and n-pentanal with chlorine atoms". In: *International Journal of Chemical Kinetics* 41.2 (2009), pp. 133–141. DOI: https://doi.org/10.1002/kin.20383. eprint: https://onlinelibrary.wiley.com/doi/pdf/10.1002/kin.20383. URL: https://onlinelibrary.wiley.com/doi/abs/10.1002/kin.20383.

[59] Enoch E. Dames et al. "An improved kinetic mechanism for 3-pentanone pyrolysis and oxidation developed using multispecies time histories in shock-tubes". In: *Combustion and Flame* 161.5 (2014), pp. 1135–1145. ISSN: 0010-2180. DOI: https://doi.org/10.1016/j.combustflame.2013.11.010. URL: https://www.sciencedirect.com/science/article/pii/S0010218013004239.

[60] Michael P. Burke, Qinghui Meng, and Christopher Sabaitis. "Dissociation-induced depletion of high-energy reactant molecules as a mechanism for pressure-dependent rate constants for bimolecular reactions". In: *Faraday Discuss.* 238 (0 2022), pp. 355–379. DOI: 10.1039/D2FD00054G. URL: http://dx.doi.org/10.1039/D2FD00054G.

[61] Frank Neese. "Software update: the ORCA program system, version 4.0". In: *WIREs Computational Molecular Science* 8.1 (2018), e1327. DOI: https://doi.org/10.1002/wcms.1327. eprint: https://wires.onlinelibrary.wiley.com/doi/pdf/10.1002/wcms.1327. URL: https://wires.onlinelibrary.wiley.com/doi/abs/10.1002/wcms.1327.

[62] Hans-Joachim Werner et al. "The Molpro quantum chemistry package". In: *The Journal of Chemical Physics* 152.14 (2020). doi: 10.1063/5.0005081, p. 144107. ISSN: 0021-9606. DOI: 10.1063/5.0005081. URL: https://doi.org/10.1063/5.0005081.

[63] Richard A. Messerly et al. "Understanding how chemical structure affects ignition-delay-time -sensitivity". In: *Combustion and Flame* 225 (2021), pp. 377–387. ISSN: 0010-2180. DOI: https://doi.org/10.1016/j.combustflame.2020.11.004. URL: https://www.sciencedirect.com/science/article/pii/S0010218020304958.

[64] Adam M. Scheer et al. "Facile Rearrangement of 3-Oxoalkyl Radicals is Evident in Low-Temperature Gas-Phase Oxidation of Ketones". In: *Journal of the American Chemical Society* 135.38 (2013). PMID: 23971980, pp. 14256–14265. DOI: 10.1021/ja405892y. eprint: https://doi.org/10.1021/ja405892y. URL: https://doi.org/10.1021/ja405892y.

[65] Et-touhami Es-sebbar, Yves Benilan, and Aamir Farooq. "Temperature-dependent absorption cross-section measurements of 1-butene (1-C4H8) in VUV and IR". In: *Journal of Quantitative Spectroscopy and Radiative Transfer* 115 (2013), pp. 1–12. ISSN: 0022-4073. DOI: https://doi.org/10.1016/j.jqsrt.2012.09.014. URL: https://www.sciencedirect.com/science/article/pii/S0022407312004190.

[66] Anna J. Harrison, Betty J. Cederholm, and Margery A. Terwilliger. "Absorption of Acyclic Oxygen Compounds in the Vacuum Ultraviolet. I. Alcohols". In: *The Journal of Chemical Physics* 30.2 (1959), pp. 355–356. DOI: 10.1063/1.1729952. eprint: https://doi.org/10.1063/1.1729952. URL: https://doi.org/10.1063/1.1729952.

[67] M. Ogawa and G. R. Cook. "Absorption Coefficients of Methyl, Ethyl, n-Propyl, and n-Butyl Alcohols". In: *The Journal of Chemical Physics* 28.4 (1958), pp. 747–748. DOI: 10.1063/1.1744253. eprint: https://doi.org/10.1063/1.1744253. URL: https://doi.org/10.1063/1.1744253.

[68] Lisa J. Bremner, Martin G. Curtis, and Isobel C. Walker. "Electronic states of some simple ethers studied by vacuum ultraviolet absorption and near-threshold electron energy-loss spectroscopy". In: *J. Chem. Soc., Faraday Trans.* 87 (8 1991), pp. 1049–1055. DOI: 10.1039/FT9918701049. URL: http://dx.doi.org/10.1039/FT9918701049.

[69] Vladimir L. Orkin et al. "Atmospheric Lifetimes and Global Warming Potentials of Hydrofluoroethers: Reactivity toward OH, UV Spectra, and IR Absorption Cross Sections". In: *The Journal of Physical Chemistry A* 103.48 (1999), pp. 9770–9779. DOI: 10.1021/jp991741t. eprint:

https://doi.org/10.1021/jp991741t. URL: https://doi.org/10.1021/jp991741t.

[70] Renfei Feng, Glyn Cooper, and C.E Brion. "UV, VUV and soft X-ray photoabsorption of dimethyl ether by dipole (e,e) spectroscopies". In: *Chemical Physics* 260.3 (2000), pp. 391–400. ISSN: 0301-0104. DOI: https://doi.org/10.1016/S0301-0104(00)00248-2. URL: https://www.sciencedirect.com/science/article/pii/S0301010400002482.

[71] Hiroshi Tsubomura et al. "Vacuum Ultraviolet Absorption Spectra of Saturated Organic Compounds with Nonbonding Electrons". In: *Bulletin of the Chemical Society of Japan* 37.3 (1964), pp. 417–423. DOI: 10.1246/bcsj.37.417. eprint: https://doi.org/10.1246/bcsj.37.417. URL: https://doi.org/10.1246/bcsj.37.417.

[72] D.R. Salahub and C. Sandorfy. "The far-ultraviolet spectra of some simple alcohols and fluoroalcohols". In: *Chemical Physics Letters* 8.1 (1971), pp. 71–74. ISSN: 0009-2614. DOI: https://doi.org/10.1016/0009-2614(71)80578-X. URL: https://www.sciencedirect.com/science/article/pii/000926147180578X.

[73] J.C. Han, Masako Suto, and L.C. Lee. "Fluorescence from photoexcitation of C2H5OH by Vacuum ultraviolet radiation". In: *Journal of Quantitative Spectroscopy and Radiative Transfer* 42.6 (1989), pp. 557–562. ISSN: 0022-4073. DOI: https://doi.org/10.1016/0022-4073(89)90046-0. URL: https://www.sciencedirect.com/science/article/pii/0022407389900460.

[74] Renfei Feng and C.E Brion. "Absolute photoabsorption cross-sections (oscillator strengths) for ethanol (5–200 eV)". In: *Chemical Physics* 282.3 (1999), pp. 9770–9779. ISSN: 0301-0104. DOI: 10.1021/jp991741t. eprint: https://doi.org/10.1021/jp991741t. URL: https://doi.org/10.1021/jp991741t.

[75] Vladimir L. Orkin et al. "High-Accuracy Measurements of OH• Reaction Rate Constants and IR and UV Absorption Spectra: Ethanol and Partially Fluorinated Ethyl Alcohols". In: *The Journal of Physical Chemistry A*

115.31 (2011). PMID: 21710989, pp. 8656–8668. DOI: 10.1021/jp202099t. eprint: https://doi.org/10.1021/jp202099t. URL: https://doi.org/10.1021/jp202099t.

[76] A. Souza Barbosa et al. "Low-lying electronic states of ethanol investigated by theoretical and synchrotron radiation methods". In: *Journal of Quantitative Spectroscopy and Radiative Transfer* 285 (2022), p. 108170. ISSN: 0022-4073. DOI: https://doi.org/10.1016/j.jqsrt.2022.108170. URL: https://www.sciencedirect.com/science/article/pii/S0022407322001078.

[77] A. Bralick et al. In: *Journal of Physical Chemistry A* (2023).

[78] Mengjie Liu et al. "Reaction Mechanism Generator v3.0: Advances in Automatic Mechanism Generation". In: *Journal of Chemical Information and Modeling* 61.6 (2021). PMID: 34048230, pp. 2686–2696. DOI: 10.1021/acs.jcim.0c01480. eprint: https://doi.org/10.1021/acs.jcim.0c01480. URL: https://doi.org/10.1021/acs.jcim.0c01480.

[79] Matthew S. Johnson et al. "RMG Database for Chemical Property Prediction". In: *Journal of Chemical Information and Modeling* 62.20 (2022). PMID: 36222558, pp. 4906–4915. DOI: 10.1021/acs.jcim.2c00965. eprint: https://doi.org/10.1021/acs.jcim.2c00965. URL: https://doi.org/10.1021/acs.jcim.2c00965.